FACULTY OF HEALTH SCIENCES
UNIVERSITY OF COPENHAGEN

REGION Rigshospitalet

Image Analysis of FET PET scans performed during Chemo-Radiotherapy of Glioblastoma Multiforme.

Michael Lundemann Jensen

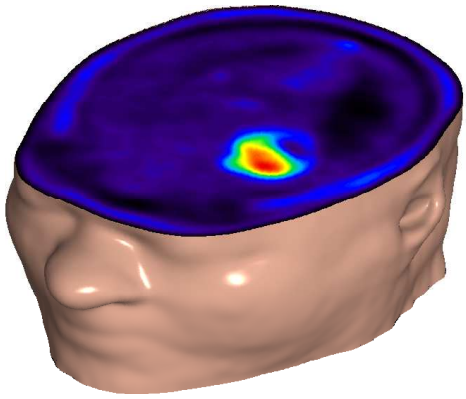

Copenhagen, 2012
IMM-Msc-2012-110

DTU Informatics
Department of Informatics and Mathematical Modelling

Department of Radiation Oncology
Rigshospitalet, University of Copenhagen
Blegdamsvej 9, DK-2100 Copenhagen, Denmark
Phone +45 35454215, Fax +45 35454015
rigshospitalet@rh.regionh.dk
www.rigshospitalet.dk

Technical University of Denmark
Informatics and Mathematical Modelling
Building 321, DK-2800 Kongens Lyngby, Denmark
Phone +45 45253351, Fax +45 45882673
reception@imm.dtu.dk
www.imm.dtu.dk

IMM-MSc-2012-110

Submitted in partial fullfillment of the
requirements for the degree of

Master of Science
in
Biomedical Imaging

at
Technical University of Denmark
and
University of Copenhagen

Supervisors
Marianne Aznar, Associate Professor, PhD
Per Munck af Rosenschöld, AD Medical Physics, PhD
Rasmus Larsen, Professor, PhD, DTU
Knut Conradsen, Professor, PhD, DTU
Censor
Jens Damgaard Andersen, Lektor Emeritus

Summary (English)

Clinical evaluation of response to chemoradiotherapy is an important discipline in cancer treatment. The prognosis for patient diagnosed with primary GBM is poor, with a median overall survival of 15 months from time of diagnosis.

This thesis characterize the response to chemoradiotherapy in 16 patients with GBM treated with a standard dose of 60 Gy in 2 Gy per fraction and concurrent TMZ. The patients underwent routine pre-treatment imaging that included several MRI modalities as well as a combined PET/CT using FET. FET has shown a high affinity for GBM while the sensitivity to inflammatory tissue is low, which give a tumor-to-background contrast that is superior to any other imaging modality. The patients underwent a second within-treatment FET-scan approximately after 40 Gy of radiotherapy, which formed the basis of response characterization.

Uncertainties associated with background and TBR_{95} were assessed and individual response criteria based on extreme value indices were established. The average required change in TBR_{95}, for the response to be considered statistically significant at a 95% level of confidence was found to be -24%.

Several intensity- and shape-related parameters, including TBR, tumor volume and solidity were calculated and compared to changes in TBR_{95}. However, clinical evaluation of the patients are needed in order to draw any conclusion about the predictive power of the parameters.

The spatial change in tumor uptake was quantified by an average distance, which was found to be 3.29 ± 2.22 mm. The tumor moved out of the 95% isodose in 5 out 16 patients at the time of the in-treatment scan.

12 out of 16 patients were characterized as non-responders and alternative treatment strategies were suggested based on the findings in this thesis.

Summary (Danish)

Klinisk evaluering af respons i forbindelse med combineret kemo- og stråleterapi er in vigtig disciplin i behandling af kræft. Prognosen for patienter diagnosticeret med primær GBM er ringe, med en samlet median overlevelse på 15 måneder fra tidspunktet hvor diagnosen stilles.

Denne afhandling karakteriserer responset til kombineret kemo- og stråleterapi i 16 patienter med GBM der er behandlet med standard dosis på 60 Gy i 2 Gy per fraktion og samtidig TMZ. Patienterne fik foretaget rutine skanninger før behandling, der inkluderede forskellige MRI modaliteter og en kombineret PET/CT med FET. FET har vist sig at have en høj affinitet for GBM og samtidigt et lavt optag i områder med betændelse, hvilket giver en tumor-til-baggrunds kontrast der er bedre end nogen anden billedmodalitet. Patienterne fik foretaget en anden FET-skanning efter cirka 40 Gy stråleterapi, hvilken dannede grundlag for respons karakteriseringen.

Usikkerheder i forbindelse med baggrund og TBR_{95} blev undersøgt og individuelle respons kriterier blev dannet på baggrund af ekstrem værdi indeks. Den gennemsnitlige ændring i TBR_{95}, der var krævet for at et respons var anset for at være statistisk signifikant ved et 95% konfidens niveau, var -24%.

Adskellige intensitets- og form-relaterede parametre, inklusiv TBR, tumor volume og soliditet blev beregnet of sammenlignet med ændringen i TBR_{95}. En klinisk evaluering af patienterne er dog nødvendig for at kunne drage konklusioner om den prædiktive effekt af de forskellige parametre.

Den spatielle ændring i tumor-optaget blev kvantificeret ved en gennemsnitlig afstand, som blev fundet til at være 3.29 ± 2.22 mm. Tumor havde flyttet sig uden for 95% isodosis i 5 ud af 16 patienter på tidspunktet for skanning nummer to.

12 ud 16 patienter blev karakteriseret som ikke-responderende og alternative behandlings strategier blev foreslået på background af resultaterne i denne afhandling.

Preface

This thesis was prepared at the department of Radiation Oncology, Copenhagen University Hospital, Rigshospitalet (RH), Copenhagen University (KU) and at the section for Image Analysis and Computer Graphics at the department of Informatics and Mathematical Modelling (IMM), Technical University of Denmark (DTU) in fulfilment of the requirements for acquiring an M.Sc. in Biomedical Engineering.

The work has been carried out from February to September 2012 and the assigned workload is 35 ECTS credits, corresponding to 980 hours of work.

The thesis deals with chemoradiotherapy response characterization of patients with glioblastoma multiforme.

Supervisors
Associate Professor, Medical Physicist, Marianne Aznar, KU and RH
Professor, PhD, Rasmus Larsen, DTU
Acting Director of Medical Physics Research, Per Munck af Rosenschöld, RH
Professor, PhD, Knut Conradsen, DTU
Censor
Lektor emeritus, Jens Damgaard Andersen

Copenhagen, 03-September-2012

Michael Lundemann Jensen

Acknowledgements

Unlike the production of photons in an X-ray tube, this thesis has not been created in vacuum and I am deeply indebted to the people around me, who have all been involved in this memorable journey. First of all I owe my greatest appreciation to my supervisors, associate professor Marianne Aznar from University of Copenhagen and Rigshospitalet, to Per Munck af Rosenschöld, acting director in medical physics research at the department of Radiation Oncology at Rigshospitalet, to Professor Rasmus Larsen and Professor Knut Conradsen, both from the section for Image Analysis and Computer Graphics at the department of Informatics and Mathematical Modelling at the Technical University of Denmark. I am much obliged for their level of dedication, their excellent guidance every time my mind reached an impasse and for always making me feel welcome. Thank you!

Also, a warm thanks to medical student Anne Sofie Bech Andersen, who patiently provided me with data and to MD, DMSc, PhD Ian Law for inspiring talks and feedback. Thanks to Mikael Olsen, B.Sc.Eng, whos office I have occupied for seven months. A special thanks to PhD student Christian Hollensen for invaluable consultations and technical inspiration.

At last, but definitely not least, a warm thanks to Andreas, Charlotte and Martin - fellow students that turned into elitist colleagues, acquaintances that turned into friends.

Nomenclatures

Abbreviations

AD	Average Distance
BTV	Biological Tumor Volume
CDF	Cumulative Distribution Function
CNS	Central Nervous System
CSF	Cerebrospinal Fluid
CT	Computed Tomography
CTV	Clinical Target Volume
DNA	Deoxyribonucleic Acid
DTI	Diffusion Tensor Imaging
DTU	Technical University of Denmark
DVH	Dose-Volume Histogram
EVI	Extreme Value Index
FDG	2-[^{18}F]fluoro-2-deoxy-D-glucose
FET	O-(2-^{18}F-fluoroethyl)-L-tyrosine
GBM	Glioblastoma Multiforme
GPD	Generalized Pareto Distribution

GTV	Gross Tumor Volume
ICRU	International Commission on Radiation Units and Measurements
IMM	Department of Informatics and Mathematical Modelling
IMRT	Intensity-Modulated Radiation Therapy
IMT	L-3-[^{123}]iodo-α-methyl tyrosine
IVH	Intensity-Volume Histogram
KU	University of Copenhagen
LOR	Line of Response
MD	Maximum Distance
MET	L-[methyl-^{1}1C]methionine
MLC	Multileaf Collimators
MRI	Magnetic Resonance Imaging
OS	Overall Survival
OSEM	Ordered Subset Expectation Maximization
PDF	Probability Density Function
PET	Positron Emission Tomography
PFS	Progression Free Survival
PTV	Planning Target Volume
RH	Rigshospitalet
SF	Survival Fraction
SUV	Standardized Uptake Value
TBR	Tumor-to-Brain Ratio
TE	Echo Time
TMZ	Temozolomide
TR	Repetition Time

Symbols

α	Linear parameter
$\bar{X}_i$	Observed mean of i^{th} variable
β	Quadratic parameter
β^+	Positron
κ	Probability of making type I error
λ	Poisson parameter
$\mathbf{R}$	Rotation matrix
$\mathbf{t}$	Translation vector
$\mathbf{w}$	Parameter vector for similarity transform
$\mathbf{x}$	Coordinate of reference scan
$\mathbf{y}$	Coordinate of template scan
$\bar{\mathcal{R}}$	Average image intensity in reference scan
$\bar{\mathcal{T}}$	Average image intensity in template scan
$\mathcal{D}$	Measure of dissimilarity
$\mathcal{R}$	Reference scan
$\mathcal{T}$	Template scan
ν	Neutrino
Ω	Region of overlap
θ_i	Rotation around the i^{th} coordinate axis
BW	Body weight
$C(t)$	Radioactivity concentration

D	Total dose
d	Dose per fraction
$D_{injected}$	Injected dose
f	Probability density function
$F^{-1}(p)$	p^{th} quantile
N	Number of fractions
n_i	Number of i^{th} observations
s	Isotropic scaling parameter
S_i^2	Observed variance of i^{th} variable
S_p^2	Pooled variance estimator
SF	Cell survival fraction
t	Student's t test statistic
T_1	Longitudinal relaxation time
T_2	Transverse relaxation time
t_i	Translation along the i^{th} coordinate axis
X	Random variable
$X_{([np])}$	$n \cdot p^{\text{th}}$ sample quantile
Z	Test statistic for large samples

Contents

Chapter 1

Introduction

Glioblastoma multiforme (GBM) is the most common and malignant brain tumor. At the same time one of the most aggressive tumors at all [1]. Approximately 5 out of 100,000 people are diagnosed every year and only 10% survive more than two years [2]. The poor prognosis has over the last couple of decades lead to intensive research in an attempt to prolong the overall survival. However, despite the numerous efforts, a revolutionary treatment has yet to be discovered. During the 1960's it was discovered that whole-brain radiation therapy doubled the survival rate and several alterations have since been attempted to improve the clinical outcome and reduce side-effects [3]. Surgery is today the primary curative attempt, but a complete resection of the tumor is often impossible due to an intricate localization in the brain and combined chemoradiotherapy is traditionally the secondary essay [3].

Surgical intervention and planning of radiation therapy necessitate precise definition of the extent of the tumor and this has traditionally been done based on anatomical information obtained by using *computed tomography* (CT) and *magnetic resonance imaging* (MRI). However, subclinical damages are often misinterpreted as they appear indistinguishable from tumor tissue, which may lead to incorrect surgical guidance and unnecessary large dose planning volumes. Functional imaging by *positron emission tomography* (PET), particularly using 2-[^{18}F]fluoro-2-deoxy-D-glucose (FDG), has over the recent decade moved from being a research topic to a standard clinical assessment in cancer diagnostics. Even though widely used in the case of brain tumors, the general high metabolic demand in brain tissue as well as diffuse uptake of FDG in inflammatory tissue lead to an image contrast that is inferior to that of other cancer types that are examined with FDG.

Recently, another PET tracer that is based on an amino acid has demonstrated a high affinity in brain tumors while not being sensitive to inflammation [4, 5]. The tracer is a fluorinated tyrosine analogue named O-(2-^{18}F-fluoroethyl)-L-tyrosine (FET) that has proved useful in both diagnosis and treatment evaluation of patient with GBM [6]. FET-PET is still a relatively new assessment, but is slowly gaining foothold as the superior assessment throughout treatment centres worldwide. The discrimination between tumor and healthy tissue has been addressed in a histology controlled study, which showed that a cut-off *tumor-to-background ratio* (TBR) of 1.6 is ideal for tumor delineation [7]. However, the definition of "background" is less clear, which is futher explained in section 3.2.1.1.

Forecasting the response to therapy based on a pre-treatment scan is a challenging task, but has been subject to much attention in studies of several cancer types, since response prediction is an important prerequisite for individualized antitumor therapy [8, 9]. Both the mean and maximum tumor-to-brain ratios have been shown to have a predictive power in patients with GBM, but this has not yet lead to more individualized treatments [10].

At Rigshospitalet, 16 patients with primary GBM were recruited to a clinical trial using FET-PET along with standard imaging modalities. The patients were scanned once prior to chemoradiotherapy and once after two-thirds of their planned treatment scheme. The idea with the second within-treatment scan was to get an idea of how the FET-uptake changed during radiotherapy and to have the possibility to alter the treatment in the remaining third part, in case the tumor did not respond to the general treatment.

1.1 Objectives

The aims of this project were to identify the patients that had responded to the chemoradiotherapy at the time of the second FET scan. In order to do this, it was necessary to establish response criteria that were useful for scans during radiotherapy. A previous study has shown that a decrease in the maximum tumor-to-background ratio of more than 10% from the pre-treatment scan to an evaluation scan obtained 7-10 weeks after chemoradiotherapy was associated with a longer overall survival [10]. However, there is no guarantee that this criterion is valid for scans obtained within treatment and since it is based on the value in the maximum voxel it might be sensitive to noise. The idea in this project was to evaluate the response based on a tumor-to-background ratio determined in the 95 percentile instead of the maximum voxel, as this is possibly a more robust measure. Furthermore, it was investigated whether it was possible

to establish an individualized response criterion, as this can possibly lead to a better treatment of the individual patient. In addition to the change in tumor-to-background ratio, the uncertainties associated with background definition was also addressed. Apart from this, a number of activity and shape related parameters were extracted from the pre-treatment scan, in order to evaluate their predictive possibilities.

The spatial change of the FET uptake during chemoradiatherapy was more pronounced than expected, hence another focus was to estimate the spreading of the tumor and quantify margin that would be required to control the tumor during the entire treatment period.

To sum up, this project aims to:

- explore the impact of differences in background definition,
- investigate the possibility of establishing an individual response criterion based on a percentile tumor-to-background ratio,
- identify patients that are responding to chemoradiotherapy,
- estimate the spatial change in tumor during chemoradiotherapy.

Chapter 2

Background

Objective This section provides a brief explanation of the theory necessary to understand the diagnosis, treatment and evaluation of patients with glioblastoma multiforme. The section is divided into four parts; the first one gives an overview of the human brain and characterization of GBM. The second and third parts deal with the important imaging modalities and therapy involved in the diagnosis and treatment of GBM, respectively, and the last part provides an overview of the statistical concepts necessary to understand the subsequent analysis.

2.1 The Human Brain

The human brain is the important part of the *central nervous system* (CNS) that resides in the cranial cavity. It is anatomically divided into several subparts as shown in figure 2.1a. In this project only the cerebrum is of interest. Cerebrum consists of the left and right hemispheres, where each is divided into four separate lobes as illustrated in figure 2.1b. The frontal lobe governs, among other things, motor function, motivation, aggression and mood, the parietal lobe is responsible for reception and evaluation of sensory motion, the temporal lobe plays an important role in memory and processing of auditory stimuli and visual stimuli are received and evaluated in the occipital lobe. The insular cortex, often denoted *insula*, which is folded deeply in between the temporal and frontal lobe, is often considered as the fifth lobe and plays a role in cognitive function. The insula is not visible in figure 2.1b, but shown in the coronal slice in figure 2.1c. Besides the signal transmitting neurons, the brain consist of a number of

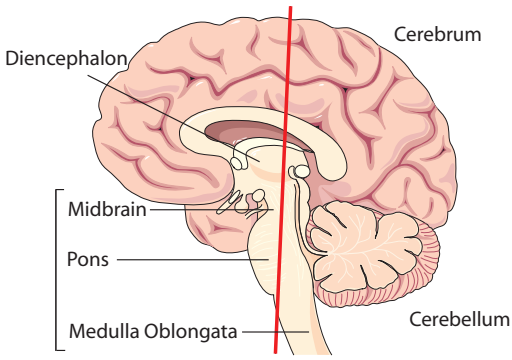

(a) Sagital slice through the brain, showing sub-division of brain parts. Only the cerebrum is of interest here. The red line illustrates the location of slice in figure c).

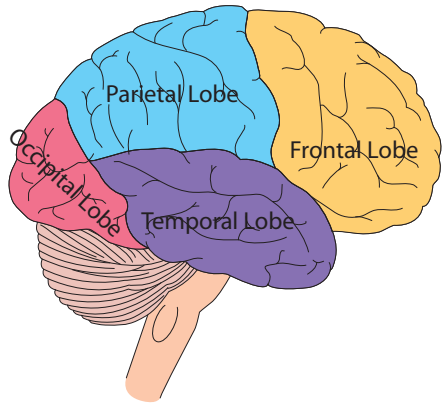

(b) Cerebrum is divided into 4 lobes. The frontal lobe (yellow), the parietal lobe (blue), the temporal lobe (purple) and the occipital lobe (magenta). See text for description of functions related to each lobe.

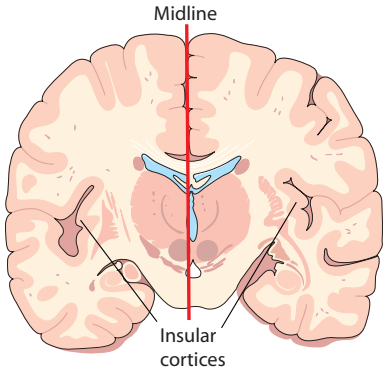

(c) Coronal slice through the brain. Location of the insular cortices are emphasized. The red line illustrates the midline, and devides the brain into two hemipheres.

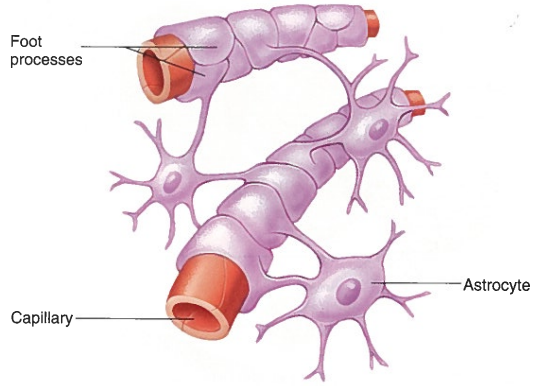

(d) Star-shaped astrocytes covering the neuronal blood vessels.

Figure 2.1: Overview of relevant brain anatomy of neuroglia. Modified from [11, 12].

supportive cells collectively known as neuroglia. The most abundant glial cell is the star-shaped astrocyte, whose cytoplasmic extension covers the surface of the blood vessels. They release substances that regulate the epithelial cells of the blood-brain barrier and play an important role in recycling of neuronal transmitting substances. Astrocytes are shown in figure 2.1d.

2.1.1 Glioblastoma multiforme

The most common and most aggressive, primary tumor in the CNS is GBM [1]. It is an astrocytic tumor, with a yearly incidence of 3-7 per 100,000 in Europe and Northern America, where less than 10% of the patients survive more than two years [2, 13, 14]. If left untreated, the average life expectancy from time of diagnosis is approximately 17 weeks [15]. Surgery and chemoradiotherapy prolong the median *progression free survival* (PFS) to 7 months and the *overall survival* (OS) to 15 months [13]. So far, no specific carcinogen related to the development of GBM has been identified, but exposure to ionizing radiation, e.g. from previous cancer treatment, has been shown as the only unequivocal predisposing factor [16, 17]. Symptoms of GBM are related to the location of the tumor, but often include headache and focal impairment, as well as simple or complex epileptic seizure [18].

Tissue growth and differentiation are normally controlled by various *protooncogenes*. Among other things, these genes code for proteins that either regulate mitosis through secretion or binding of different growth factors and hormones, or initiation of apoptosis in case of faulty repair of *deoxyribonucleic acid* (DNA). Alteration of the genetic sequence may result in defective protooncogenes, after which the normal function is impaired and can result in increased protein activity or loss of regulation. The mutation of a protooncogene into an *oncogene* is a process which in cancer terminology is known as *initiation*. Initiation of tissue might alter normal tissue growth and lead to rapid cellular proliferation, in which the formation of neoplastic tissue exceeds the rate at which old cells perish. The rapid division of cancer cells often result in irregular shaped tumor masses that invade normal tissue as illustrated in figure 2.2. In addition, as the tumor continues to expand, it might outgrow the vascularization which becomes inadequate. This results in hypoxic and subsequently anoxic areas that may be crucial for tumor control [19].

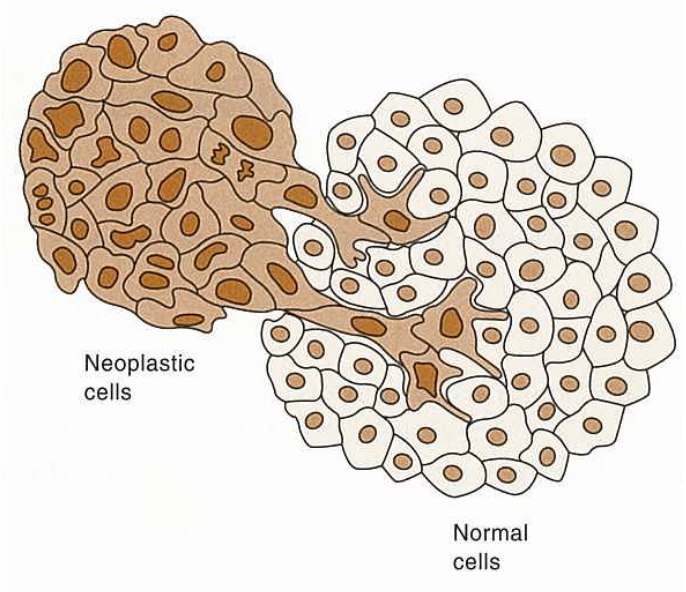

Figure 2.2: Illustration of the infiltrative behaviour that is pronounced in GBM. The rapid division of tumor cells often result in irregular masses that intrude normal tissue. From [19]

2.2 Imaging Diagnostic

Since the discovery of X-rays by Roentgen in 1895, the development and use of imaging as a diagnostic tool have increased rapidly. The following elaborates some of the techniques most used today, which are all relevant in the diagnosis and evaluation of several cancer types, including all brain tumors.

2.2.1 Positron emission tomography

Positron Emission Tomography is an imaging modality that use positron emitting radionuclides labelled to molecules that are introduced into the body, usually by injection or inhalation. The labelled compound is distributed within the body depending on its biological characteristics, from where the radioactive decay of the nuclei are spatially registered. One of the most commonly used radionuclides in PET imaging is fluorine-18, or ^{18}F, that has an excess of protons compared to the number of neutrons. Such nuclei with an imbalance in nucleons may decay to their stable isotope through a beta-plus decay; that is

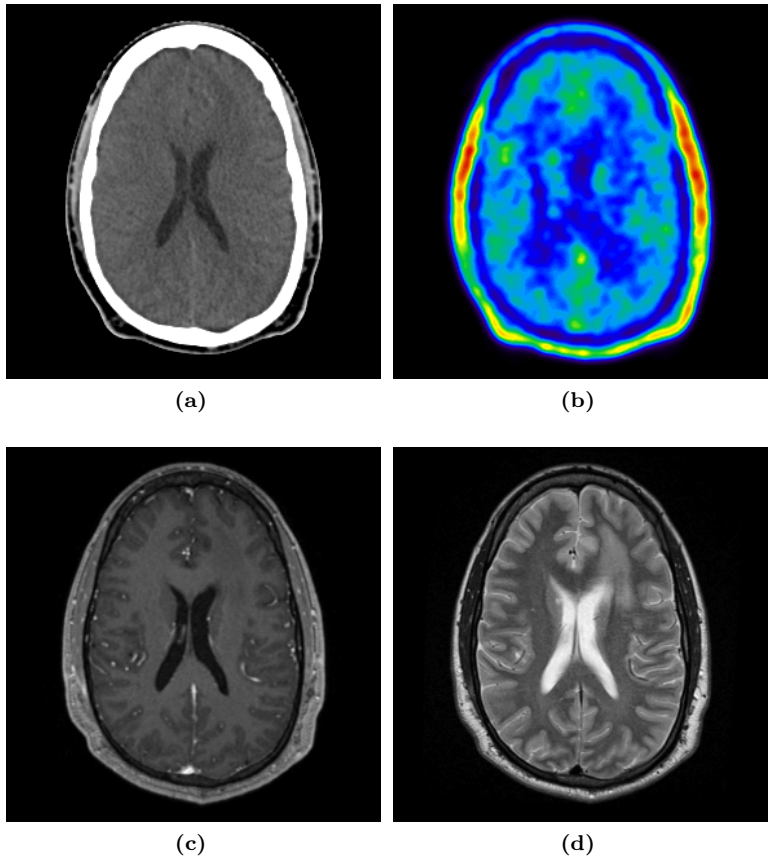

Figure 2.3: Figure showing the imaging modalities involved in diagnosis of GBM. (a) Computed tomography, (b) Positron emission tomography, (c) T1-weighted magnetic resonance imaging and (d) T2-weighted magnetic resonance imaging.

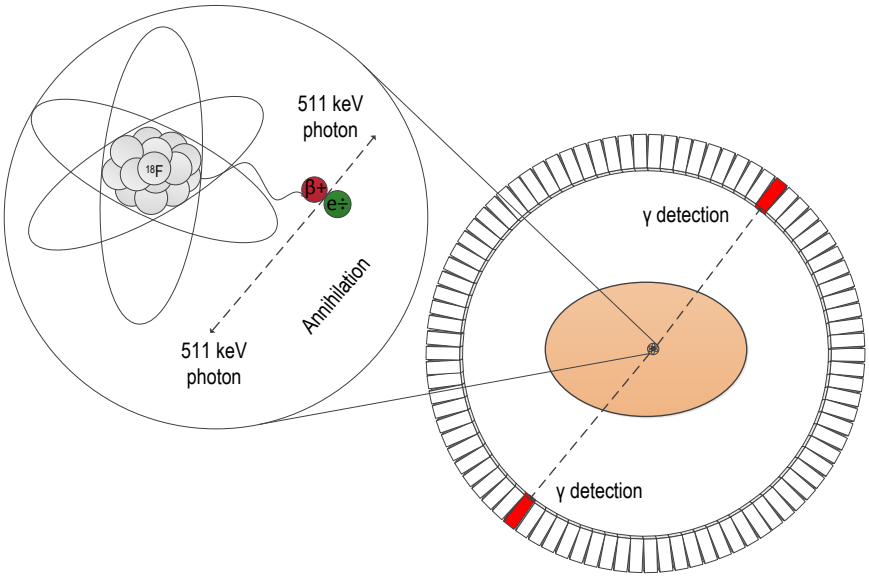

Figure 2.4: Registration of annihilation. The radioactive decay of ^{18}F results in emission of a positron that quickly annihilates with an electron. This results in the emission of two photons in opposite directions, which are registered in two opposing PET detectors.

the conversion of a proton to a neutron and a positron, as described by equation 2.1:

$$^{18}F \rightarrow ^{18}O + \beta^{+} + \nu \, . \tag{2.1}$$

The positron, which is sometimes referred to as a beta-plus particle, β^{+}, is the electron antiparticle with same mass but opposite charge. The energy released from the decay is transferred as kinetic energy to both the positron and a neutrino, ν, that is ejected from the nucleus along with the positron [20]. The emitted positron will travel some distance, while gradually loosing energy due to inelastic interactions, before it annihilates with an electron when most of its kinetic energy has been dissipated. Through conservation of mass and momentum, the annihilation results in the emission of two photons in opposite directions, each with an energy of 511 keV, as illustrated in the left part of figure 2.4. The physical characteristic of the two photons are exploited in the registration of events using a coincidence detection system. A decay is registered by two opposing detectors as shown in the right part of figure 2.4. The registration is only valid if two photons are registered within a limited time window. The line between two incident detectors is denoted the *line of response* (LOR) and the number of decays along each LOR is collected as a *sinogram*, which represents a

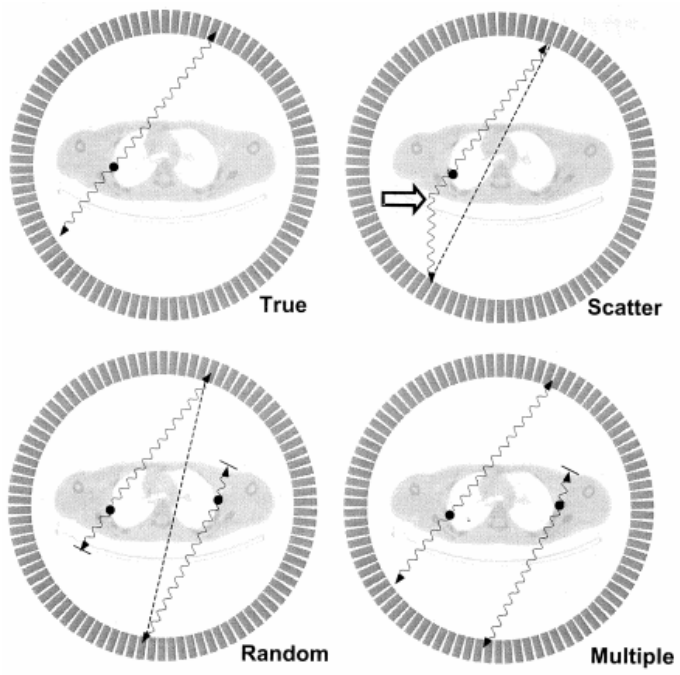

Figure 2.5: Several situations can result in the registration of photons along a misleading LOR. Photons might be deflected from their trajectory resulting in a scattered event (top right). Multiple decays may be registered in more than two detectors (bottom right) or the two random decays may be registered as one event (bottom left). From [21].

matrix of object projections. Several undesired coincidences may contribute to the acquired sinogram, as illustrated in figure 2.5. Scattered and random coincidences will result in false LOR's that do not contribute to the true information about the spatial distribution of the tracer, but which cannot be distinguished from true coincidences. Multiple coincidences, where more than two incident photons are registered within the time window, may result from examinations with high count-rates, but these are normally discarded since they lead to ambiguous LOR's. Correcting for these unwanted events can be cumbersome, but is important in order to improve the diagnostic quality of the images.

Traditionally, PET-images have been reconstructed from acquired sinograms using analytical methods, especially filtered backprojection, where images are constructed from simple line integrals. Recently, as the available computation power has increased, iterative reconstruction methods are more frequently being used. This reconstruction algorithm is based on expectation-maximization

algortithms that maximize the likelihood that a given model represents the projection data acquired. The number of computations for each iteration is proportional to the number of elements in the sinogram times the number of voxels in the image, which becomes extremely numerous for images with a high resolution. A way to speed up the reconstruction, is to only optimize an ordered subset of the projection angles, hence reducing the number of calculations in each iteration. This popular algorithm is called *ordered subset expectation maximization* (OSEM) [22, 23]. An example of a PET image is shown in figure 2.3b.

Standard uptake value

Tumor activity is often interpreted as proportional to the uptake of the radioactive tracer being used, hence regions in images with a high count rate is associated with a high tumor activity. The *standardized uptake value* (SUV) is often used as a quantitative measure of tumor uptake, where the tissue radioactivity concentration is normalized by the injected activity and body weight, as described in equation 2.2:

$$SUV = \frac{C_{PET}(t)}{D_{injected}/BW} \ , \tag{2.2}$$

where $C_{PET}(t)$ is the decay corrected radioactivity concentration at time t from injection, D is the injected dose and BW is body weight in kilogram [24].

Even though widely used, the correctness of SUV as a quantitative measure of malignancy in the form presented in equation 2.2 has been questioned over the years, since the sources of variability are numerous and often not taken into account [25, 26]. The factors influencing SUV may be divided into *biological* and *technological* and just to mention a few, the biologic factors include body weight estimates, postinjection uptake time and blood level of competing tracer analogous, whereas partial volume effects, difference in reconstruction parameters and inter-scanner variability account for the most important technological factors.

O-(2-^{18}F-fluoroethyl)-L-tyrosine

Delineation, differentiation and detection of recurrence have been shown to be more accurate when using L-[methyl-^{11}C]methionine (MET) compared to FDG and anatomical imaging [27, 28, 29, 30, 31], but due to the relative short half

life of ^{11}C (20.33 min) [32], the use has been restricted to a few sites equipped with a cyclotron.

The tyrosine-based tracer, O-(2-^{18}F-fluoroethyl)-L-tyrosine (FET), has been shown to have very similar uptake characteristics to that of MET and produce PET images with similar contrast and discriminative capabilities [27]. The 110-min half life of the ^{18}F isotope [32] does not restrict the use of FET to centres with an on-site cyclotron, but can be used by "satellite" PET centres similarly to FDG. FET is synthesized via a two-step process not explained here and the difference between FET and its natural isomer is shown in figure 2.6 [33, 34].

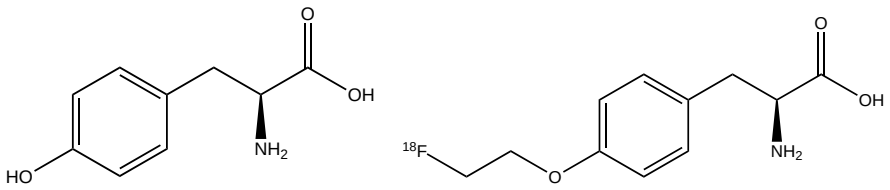

(a) L-tyrosine. **(b)** O-(2-^{18}F-fluoroethyl)-L-tyrosine.

Figure 2.6: Fluorination of L-tyrosine by the radioactive nuclei ^{18}F leads to FET.

FET is not incorporated into proteins and does not participate in any metabolic pathway [5], but is transported across the epithelium and epithelial blood barrier by a subtype of the L-transport system denoted LAT2 [35], hence the prefix L. LAT2 has not been identified in inflammatory cells, which preclude the uptake of FET in inflamed tissue and which potentially makes it even more tumor-specific than MET [36]. The uptake of FET in brain tumors reaches a plateau approximately 20 minutes post-injection as shown in figure 2.7. The uptake in grey and white matter continues to increase for a longer period, which will lead to lower *tumor-to-brain* ratios (TBR) from 20 to 60 minutes after injection. In a histology controlled study by Pauleit et al.[7], the use of FET-PET in addition to MRI has shown to significantly improve the discrimination between tumor and peritumoral tissue. A mean tumor-to-brain ratio (TBR) of FET uptake was found to be 2.9±0.9, while the ratio between areas with contrast enhancement in MRI but not in FET was found to be 1.1±0.4. Based on these findings, a cut-off TBR of 1.6 has subsequently been widely used to auto-contour tumoral tissue.

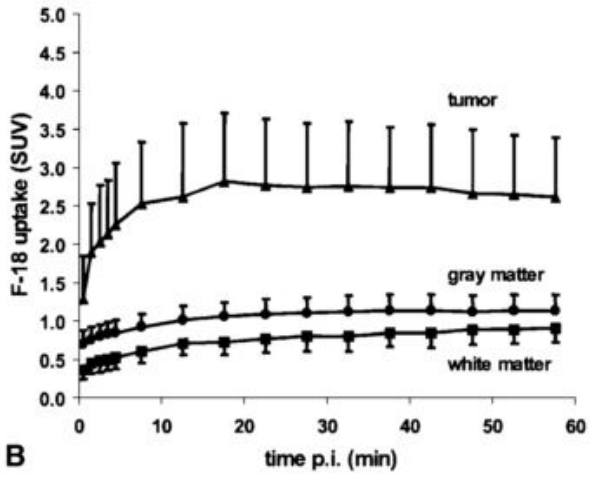

Figure 2.7: Uptake kinetics of FET in brain tumors, and grey and white matter, respectively. A plateau in brain tumors is reached approximately 20 minutes post-injection. From [27].

2.2.2 Computed tomography

Volumetric imaging became possible with the invention of computed tomography (CT). Tomographic images are acquired by rotating an X-ray source around an object of interest, hereby collecting tomographic projections of X-rays through the object from several directions. The electromagnetic radiation transmitted by the X-ray source, is attenuated it passes through the object [37]. The attenuated intensity is described by:

$$I(x) = I_0 e^{-\mu x};, \tag{2.3}$$

where I_0 is the transmitted intensity and x is the thickness of the object. The linear attenuation coefficient, μ, is a function of the energy of the transmitted X-rays photons, the density and the atomic number of the object. Reconstruction of the tomographic projections, similar to those described in section 2.2.1, provides a map of linear coefficients that is proportional to the density of the object. In addition to providing anatomical information, the CT image is often used to correct for attenuation in PET [38]. An example of a CT image is shown in figure 2.3a.

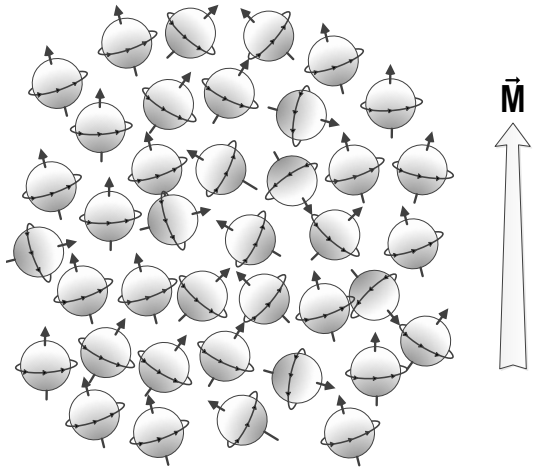

Figure 2.8: Illustration of an ensemble of nuclear spins in a magnetic field. The arrows represent the magnetic moments generated by the spin of each nuclei. Note the partial alignment of the nuclei that generate a net magnetic moment $\vec{\mathbf{M}}$.

2.2.3 Magnetic resonance imaging

In contrast to both PET and CT, magnetic resonance imaging does not expose patients to any ionizing radiation. Images are generated using RF waves and a strong magnetic field. The technique exploits the physical property called *spin*, possessed by some nuclei including hydrogen, which generates a nuclear magnetic moment along the spin axis as illustrated in figure 2.8. The human body is composed of more than seventy percent water and when placed within a strong magnetic field, here denoted $\vec{B}_0$, the abundantly present hydrogen nuclei tend to align with the direction of the magnetic field [12, 39]. The magnetic moment of a single nucleus is not measurable, but the alignment of several protons creates an ensemble of nuclei that generate a net magnetic moment, $\vec{\mathbf{M}}$, as illustrated in figure 2.8.

In equilibrium, when the net magnetic moment is parallel to $\vec{B}_0$, the body is irradiated with radio waves. This affect $\vec{\mathbf{M}}$ as an oscillating magnetic field perpendicular to $\vec{B}_0$ and $\vec{\mathbf{M}}$ is rotated away from the direction of the outer magnetic field. Once the transmitting radio waves are turned off, the net magnetic moment will return to equilibrium - a process called relaxation. The return to equilibrium creates an alternating magnetic field that generates an electric current when recorded with a receiver antenna coil. The relaxation back towards magnetic equilibrium occurs on two different time scales; one representing the

loss of transverse magnetization due to spin-spin interaction, characterized by the time constant T_2. The second is characterized by T_1, which represents the rebuilding of magnetization along the longitudinal axis parallel to $\vec{B}_0$. The two time constants are highly dependent on the tissue type and differences will be reflected in MR images [40].

The amplitude of the signal that is generated in the receiver coil, when the net magnetic moment returns to equilibrium is, among other things, a function of the tissue parameters, i.e. proton density (water content), T_1 and T_2.

Images are not acquired from a single excitation, but rather a series of excitations collectively called a *sequence*. Several different sequence parameters can be tweaked to enhance the difference in a specific tissue parameter, e.g. water content. An image where the contrast primarily derives from differences in T_1 is said to be T_1-weighted. Among the most important sequence parameters are the time between each excitation, denoted the *repetition time* (TR) and the time from excitation to signal readout, called the *echo time* (TE) [39, 40]. Examples of T1 and T2-weighted images are shown in figure 2.3c and 2.3d, respectively.

2.2.4 Image registration

Comparison of images acquired at different timepoints requires that the different scans are registered to a common space. A similarity transformation is often applied to compensate for different patient positioning at the two acquisitions and/or when the images are collected at two different scanners. The similarity transformation consist of translation, rotation and isotropic scaling and if $\mathbf{x}$ denote the coordinates of the reference scan, $\mathcal{R}$, and $\mathbf{y}$ the coordinate of the template scan, $\mathcal{T}$, which is to be transformed to the reference, the transformation can be described by equation 2.4:

$$\mathbf{y}(\mathbf{x}; \mathbf{w}) = s\mathbf{R}\mathbf{x} + \mathbf{t} \tag{2.4}$$

where $\mathbf{w} = (s, \theta_1, \theta_2, \theta_3, t_1, t_2, t_3)^T$ is a parameter vector representing the transformation. R is an orthogonal rotation matrix rotate $\mathcal{T}$ around the i^{th} coordinate axis with angles specified by θ_i. t_i denote translation along the i^{th} coordinate axis and s is the isotropic scaling factor. The objective of the image-transformation then becomes a matter of estimating the parameter $\mathbf{w}$ that maps the template image into the reference image. This can be done by iteratively updating the parameters that minimize the dissimilarity between the two images.

A common measure of dissimilarity in registration procedures is the sum of squared differences, however, this dissimilarity measure assumes that the voxel

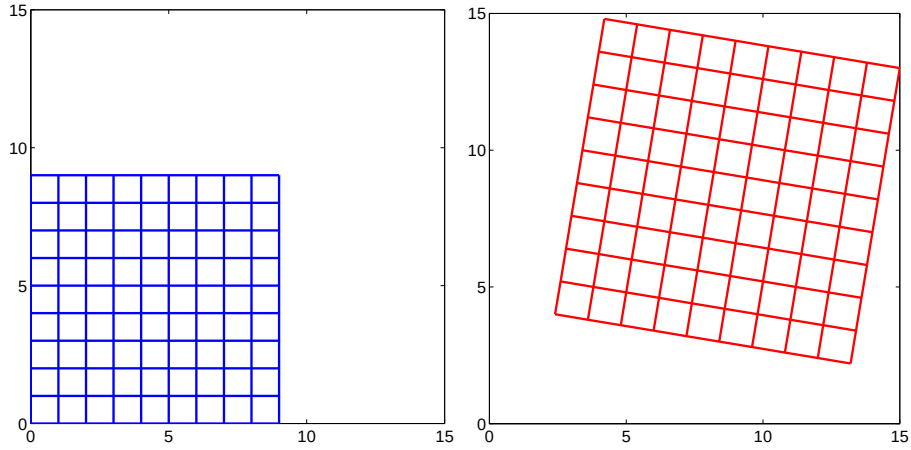

(a) Reference grid. **(b)** Transformed template grid.

Figure 2.9: Illustration of a 2D similarity transform. The red grid is a translated, rotated and isotropically scaled version of the blue grid. In image registration, the operation is the opposite way - the objective is to find the transformation that maps the red grid onto the blue grid.

intensities in the two scans are identical. This assumption may be violated when the images are acquired at two different scanners. In such situations a linear relationship exist between the voxel intensities in the reference and the template, hence a suitable dissimilarity measure is the normalized cross correlation [41]. The objective of the registration process is then to minimize:

$$\mathcal{D}_{CC}(\mathbf{w}) = \frac{\sum_{i\in\Omega}\left(\mathcal{T}\left(\mathbf{y}\left(\mathbf{x_i};\mathbf{w}\right)\right)-\bar{\mathcal{T}}\right)\left(\mathcal{R}\left(\mathbf{x_i}\right)-\bar{\mathcal{R}}\right)}{\sqrt{\sum_{i\in\Omega}\left(\mathcal{T}\left(\mathbf{y}\left(\mathbf{x_i};\mathbf{w}\right)\right)-\bar{\mathcal{T}}\right)^2\sum_{i\in\Omega}\left(\mathcal{R}\left(\mathbf{x_i}\right)-\bar{\mathcal{R}}\right)^2}}\,, \tag{2.5}$$

where Ω denote the region over which the dissimilarity is calculated, e.g. the entire overlap or a subset of both images. $\bar{\mathcal{T}}$ and $\bar{\mathcal{R}}$ are the average image intensity in Ω of the template and reference, respectively. An example of a coordinate grid that has been similarity transformed is shown in figure 2.9.

Once the transform has been determined, it will most often be necessary to interpolate the original image at the newly found grid points. The simplest form of interpolation is to assign the intensity value of the nearest integer neighbour or making a weighted sum of the nearest two, four or eight integer neighbours in 1, 2 and 3 dimensions, respectively. A more accurate, but yet more computationally demanding interpolation scheme is to use higher order polynomials. Especially third order, piecewise polynomials, known as cubic B-splines, have been widely used [42, 41].

2.3 Antitumor Therapy

Surgery is the primary curative or palliative attempt in nearly all cancer diseases [17]. Complete resection of brain tumors is often not possible, and patients undergo a subsequent period with combined chemo- and radiotheraphy, followed by adjuvant chemotherapy, as this has proved to be the best way to prolong patient survival [14, 43].

2.3.1 Surgery

Surgical removal of bulk tumoral tissue is the primary curative attempt in treating patients with glioblastoma multiforme [2],[13]. Intricate localization, including tumors located in the motor cortex in the frontal lobe, the corpus callosum or tumors that affect both hemispheres, often preclude total resection. The infiltrative growth of high grade gliomas, as illustrated in figure 2.2, is another factor that often hinder removal of all tumor cells. In situations where total resection is impossible, as much neoplastic tissue as possible is removed, since this is associated with a better prognosis [44]. In complicated cases, only a diagnostic biopsy is removed. The extracted specimen, being either the bulk tumor or the biopsy, is used to do a histological determination of the tissue of origin and degree of malignancy.

2.3.2 Radiotherapy

The purpose of radiotherapy is to deliver a lethal dose of ionizing radiation to neoplastic cells either *directly* or through *indirect* interactions, while preserving normal tissue. Dose is measured in units of Gy, which is defined as the number of joules absorbed by one kilogram of mass. Radiating tissue with charged particles, such as protons, electrons and alpha particles, will most probably have a direct crucial impact on different cell components, e.g. DNA. Indirect ionization is most likely to occur when the radiation is composed of photons, such as X-rays or gamma rays. Indirect effects facilitate the formation of *free radicals* through an intrinsic series of reactions that cause the splitting of water molecules. Free radicals are highly reactive ions that, if created, close to the cell nucleus, will cause damage to the chemical composition of DNA [17]. The cellular radiosensitivity depends on the phase of the cell cycle, the cell differentiation and mitotic future [17]. Undifferentiated, dividing cells with a long mitotic future are generally more sensitive to radiation than fully differentiated cells.

The cellular response to ionizing radiation is often described using the *linear quadratic model of cell survival* [45]. The model builds on the assumption that a cell is inactivated only if both strands of the double helix in the DNA-molecule are damaged. This might be an oversimplification, since the cellular response is influenced by several physical, chemical and biological factors, as explained later, but the model is widely accepted as the best way to characterize radiotherapy response [46]. Double strand breaks might be caused by two different events; 1) one ionizing particle hitting both helices or 2) two different particles breaking one strand each. Both of these events happen randomly and due to the low probability that a specific cell will be inactivated, the *survival fraction* (SF) of cells will be Poisson distributed. The Poisson distribution is given by:

$$f(k;\lambda) = \frac{\lambda^k e^{-\lambda}}{k!} \tag{2.6}$$

where k is the number of discrete events during a fixed time interval and λ is the average number of events in that period. The probability of no lethal events implies that $k = 0$, λ denotes the mean number of hits per cell and $f(0;\lambda) = SF$ which leads to equation 2.7:

$$SF = e^{-\lambda};. \tag{2.7}$$

For the single particle case, the expected number of hit cells is directly proportional to the ionizing dose, d, and following this $\lambda = \alpha d$, where α is a factor describing the mean probability that 1) will occur. In scenarios where the double helix are damaged by two separate particles, the expected number of inactivated cells equals $\lambda = \beta d^2$, where β is the mean probability of event 2) occurring. The overall probability of cell survival is then given by equation 2.8.

$$SF = e^{-\alpha d - \beta d^2}\ . \tag{2.8}$$

The parameters α and β vary with specific tissue types, and reflect the tissue response to therapy. Especially the ratio α/β is an important factor when modelling the response to therapy. The ratio represents the dose at which the logarithm of the linear contribution to tissue damage, equals the quadratic contribution, i.e. $\alpha d = \beta d^2$, and is an estimate of the curvature of the cell survival fraction curve as shown in figure 2.10a. α/β-ratios have been experimentally determined for various tissue types, where tumors most often have a high ratio and normal tissue a low ratio [46].

Fractionation As mentioned previously, the purpose of radiotherapy is to maximize the surviving fractions of normal tissue cells, while minimizing the number of surviving tumor cells. When inspecting figure 2.10a, this might seem like an impossible situation, as increasing the dose above 6 Gy causes the normal tissue cells to die at a faster rate than neoplastic cells. This is one of the

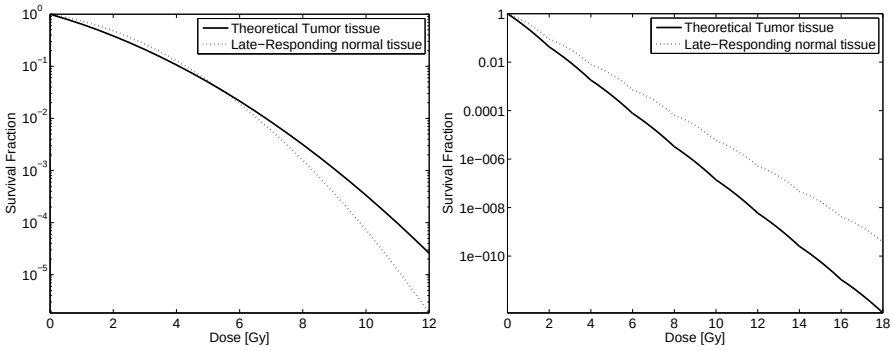

(a) Cell survival curve for tumor and late-responding normal tissue

(b) Effect of fractionation. With inspiration from [45].

Figure 2.10: Cell survival curve for tumor and late-responding normal tissue, using theoretical values for α/β. The ratio describes the shape of the curve where a low ratio gives a more bendy curve compared to a high ratio. Here $\alpha/\beta = 3$ and $\alpha/\beta = 10$ is used for late-responding normal tissue and tumor, respectively [46].

rationales behind delivering therapy in several smaller fractions, usually around 2 Gy in 30 fractions with 5 fractions a week [17, 45, 46]. Successive fractions have shown to be equally effective, if the time between them is sufficient to complete repair of sublethal damages and the effect of N fractions might be expressed as [17]:

$$SF^N = e^{N(-\alpha d - \beta d^2)} = e^{-\alpha D - \beta d D} \tag{2.9}$$

where $D = N \cdot d$ is the total dose. Graphically, this means that the shape of the cell survival curve will simply repeat for each fraction, as shown in figure 2.10b, hence resulting in a separation of the surviving fraction of tumor cells and healthy tissue, respectively.

The biologic response to therapy is governed by the four R's of radiotherapy; Repair, Reoxygenation, Redistribution and Repopulation. *Repair* of sublethal damage occurs within hours after radiation exposure. It is highly oxygen dependent, which favours normal tissue, since part of the tumor is often hypoxic. Hypoxic areas of the tumor might regain access to oxygen as surrounding cells are destroyed - a process known as *reoxygenation* - after which the formation of free radicals is more plausible. As mentioned previously, dividing cells are more sensitive than cells in resting state. Exposure to ionizing radiation will have greatest impact on cells in the mitotic phase, whereas cells surviving a single fraction of radiation therapy tend to *redistribute* into a later phase in the cell cycle, making them more vulnerable to a second fraction of radiation.

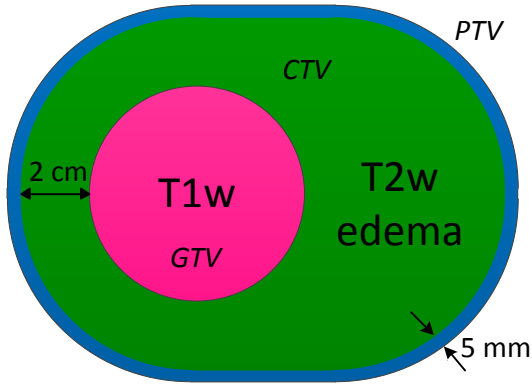

Figure 2.11: In patients with GBM, the GTV is defined by radiologists as the contrast enhanced area on T_1-weighted MRI. GTV is expanded by 2 cm to generate the CTV, which is extended even further if contrast enhancement on T_2-weighted MRI shows sign of edema. A dosimetric margin of 0.5 cm is added to the CTV to create the PTV.

Repopulation is the generation of new cells, as others are killed. Tumor cells often divide more rapidly than normal cell, hence repopulation of tumor cells often occur on a shorter time scale, which imply that fractionation should not be overly protracted.

2.3.2.1 Treatment planning and dose delivery

Treatment schemes are constructed based on the acquired planning images. The *International Commission on Radiation Units and Measurements* (ICRU) recommends the use of different planning volumes [47, 48]. The *gross tumor volume* (GTV) represents the proportion of the tumor that is palpable, visible or in any other way demonstrable. In patients with GBM, the GTV is traditionally delineated based on abnormalities in T_1-weighted MRI. Extending the contour of GTV, usually by a 2 cm margin, is the *clinical target volume* (CTV) that serves to include all subclinical, microscopic extensions that may not be visible in diagnostic images. Peritumoral edema visible on T_2-weighted MRI is usually included in CTV. The *planning target volume* (PTV) contains the CTV, plus an additional dosimetric margin, usually of 0.5 cm. The extra margin is added to compensate all geometric uncertainties, such as anatomical displacement of the tumor and more importantly to comply with different patient positioning. Figure 2.11 shows an illustration of the different tumor volumes as suggested by ICRU. Treatment schemes for brain tumors are usually inversely planned, meaning that a dosimetrist applies the dose to the tumor volume as prescribed by

the physician. Furthermore, the dosimetrist has to ensure that dose constraints to organs at risk, as also prescribed by the physician, are not exceeded. Based on these specifications, beam geometry, beam intensity, gantry angle and other parameters are optimized by computer simulation, until a satisfying dose distribution is obtained. The treatment should be planned such that PTV receives at least 95% and no more than 110% of the prescribed dose [45]. An example of a dose plan is showed in figure 2.12a. An important tool when evaluating the estimated dose distribution is the so-called *dose-volume histogram* (DVH), which is a plot showing the minimum dose absorbed within a certain volume of a given structure. Figure 2.12b shows the DVH related to the dose distribution in figure 2.12a. When evaluating a DVH, it is desired that the curves representing organs at risk decrease as quickly as possible, i.e. are located in the leftmost part of the diagram, while curves representing tumor volumes should cover a high percentage volume at the prescribed dose and then decrease rapidly to ensure a high dose uniformity [17, 45].

A novel way to deliver the prescribed dose to the tumor, while sparing organs at risk, is by using *intensity-modulated radiation therapy* (IMRT). The radiation beam is formed by *multi-leaf collimators* (MLC), which are small shielding blocks of heavy material capable of obstructing the photon flux. Figure 2.13 shows one beam configuration, targeting the tumor volume. The MLC-configuration is represented by the blue bars, and modulates the beam dynamically as the radiation gantry is rotated around the head along the red horizontal curve. The result is a beam optimized to deliver dose primarily to the tumor, while sparing surrounding tissue [17, 45].

2.3.3 Chemotherapy

In addition to surgery and radiation therapy, chemotherapy is an additional treatment modality offered to patients with brain tumors. Chemotherapeutic agents are cell toxic substances, classified either by their source or by the action carried out on the cell [17]. *Temozolomide* (TMZ) delivered both during and after radiation therapy has shown to prolong both progression free survival and overall survival of patients with GBM [14, 43, 49]. The antitumor effect of TMZ is thought to be caused by methylation of DNA, i.e alteration of the biochemical composition of DNA by addition of a methyl group, which among other things inhibit normal DNA repair. The major drawback of chemotherapy in general is the considerable degree to which normal tissue is affected as well, but administration of TMZ has proved not to significantly affect patients quality of life [2].

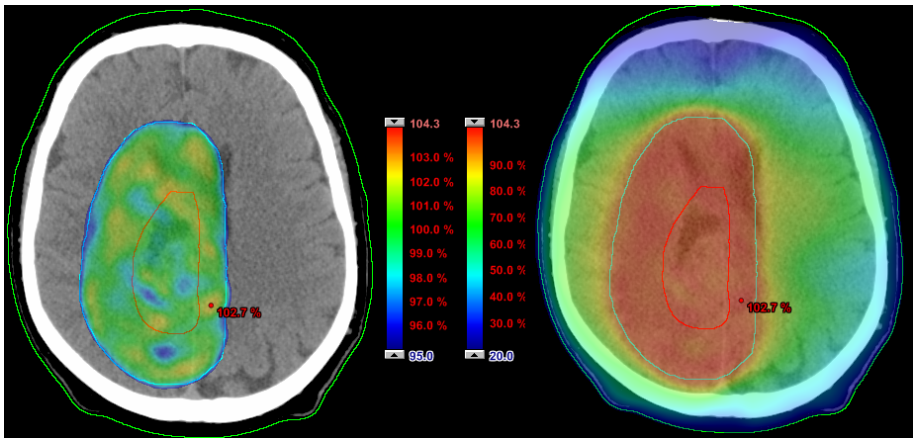

(a) Left side shows everything above 95% of the prescribed dose and it is noticed that the volume within PTV (blue contour) is covered by the required dose. GTV is delineated by the red contour. Right part of the figure shows that the whole brain receives a considerable amount of radiation.

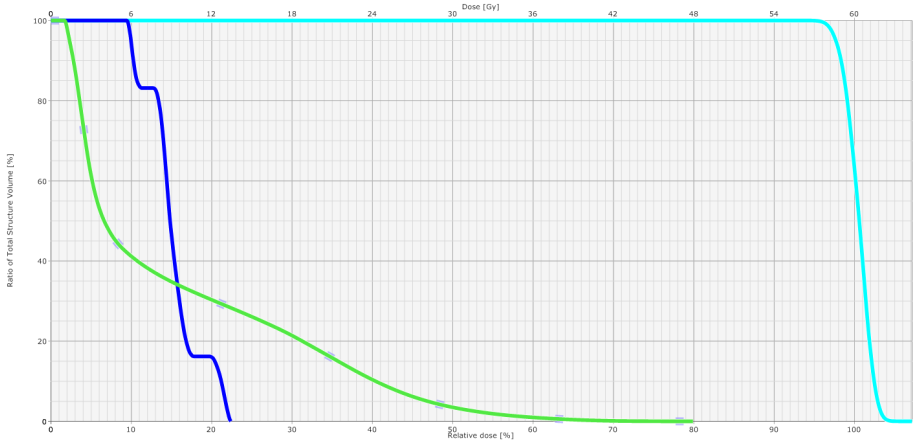

(b) Dose-volume histogram. The cyan, green and blue curves show the relative dose delivered to the PTV, brainstem and optic nerve, respectively.

Figure 2.12: a) An example of a dose plan, showing that the entire brain receives a considerable amount of dose and that PTV receives 95% of the prescribed dose. b) Dose-volume histogram showing the dose delivered to important volumes.

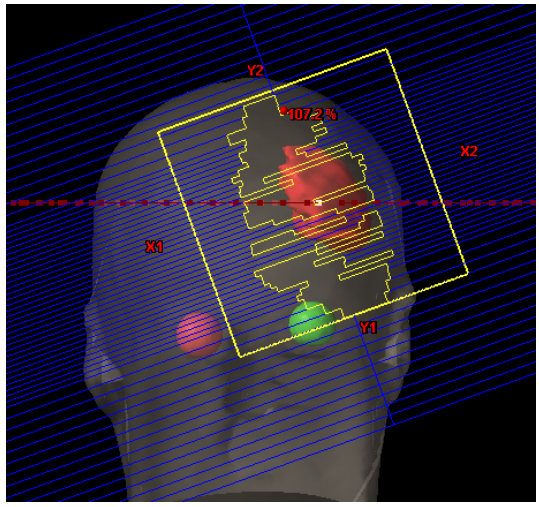

Figure 2.13: Figure showing how the intensity-modulated radiation therapy is delivered to the tumor (red mass). The yellow square represents the beam gantry and the MLC that modulates the radiation beam is shown as the blue bars. The gantry is rotated around the patient while the MLC regulate the flux of photons.

2.4 Statistics

This section provides a definition of the statistical concepts used throughout this thesis. The first part explains how it is decided whether a difference between two measures is significant, while the last part presents a method to quantify uncertainties of extreme values in a distribution.

2.4.1 Inference about means

Testing whether the difference between the means of two independent variables is significant or not, is usually formulated as *test of hypothesis*. The assertion which it is desired to reject is denoted the null hypothesis, H_0, and the alternative hypothesis which is then accepted is denoted H_1. If μ_X and μ_Y are the means of two independent random variables, both drawn from a normal population, the alternative hypotheses to the test that $\mu_X = \mu_Y$ are summarized in table 2.1. κ is the probability of making a type I error, i.e. rejecting H_0 when it is true and z_κ is the critical value. For large sample sizes Z is given by equation

$\mathbf{H_1}$	**Reject $\mathbf{H_0}$ if**
$\mu_X - \mu_Y < 0$	$Z < -z_\kappa$
$\mu_X - \mu_Y > 0$	$Z > z_\kappa$
$\mu_X - \mu_Y \neq 0$	$Z < -z_{\kappa/2}$ or $Z > z_{\kappa/2}$

Table 2.1: Rejection criterias for mean hypothesis.

2.10:

$$Z = \frac{\bar{X} - \bar{Y}}{\sqrt{\frac{S_X^2}{n_X} + \frac{S_Y^2}{n_Y}}} , \tag{2.10}$$

where the bar notation represents the estimated mean of each variables, s_i^2 their sample variance and n_i the number of samples [50].

For small sample sizes the test statistic is given by equation 2.11.

$$t = \frac{\bar{X} - \bar{Y}}{S_p\sqrt{\frac{1}{n_X} + \frac{1}{n_Y}}} , \tag{2.11}$$

where S_p^2 is the pooled estimator of variance in both samples and is given by equation 2.12:

$$S_p^2 = \frac{(n_X - 1)s_X^2 + (n_Y - 1)s_Y^2}{n_X + n_Y - 2} . \tag{2.12}$$

A confidence interval concerning hypotheses about one mean can be formulated as

$$\bar{X} - t_{\kappa/2}\frac{s}{\sqrt{n}} < \mu < \bar{X} + t_{\kappa/2}\frac{s}{\sqrt{n}} , \tag{2.13}$$

where $\bar{X}$ is the sample mean, s the standard error of the sample, n the number of samples and $t_{\kappa/2}$ the test-statistic at a $(1-\kappa)100\%$ level of confidence [50].

2.4.2 Order statistics

When evaluating observations in an experiment, it is often desired to estimate the expected value and its associated variance. This is straightforward if data is drawn from well defined distributions, like the normal distribution, but it becomes more complicated if the underlying distribution is unknown [51]. One approach is to use order statistics.

A set of independent and identically distributed observations $X_1, X_2, \cdots X_n$ are ordered in ascending order $X_{(1)}, X_{(2)}, \cdots, X_{(n)}$, where $X_{(1)}$ is the smallest and $X_{(n)}$ the largest observation, respectively. For $n \to \infty$, and if $X_{(n)}$ converge to a non-single value, the p^{th} sample quantile will be asymptotically normal distributed and the mean, $\hat{x}_p$, and variance, $\hat{\sigma}_p^2$, are approximated by:

$$X_{([np])} \sim AN\left(F^{-1}(p), \frac{p(1-p)}{n\left(f\left(F^{-1}(p)\right)\right)^2}\right) = \left(\hat{x}_p, \hat{\sigma}_p^2\right) \ , \tag{2.14}$$

where $X_{([np])}$ is the sample quantile, f is the density function and F^{-1} is the quantile function [51]. Determination of the two parameters are illustrated in figure 2.14. For a theoretical distribution, the expected quantile can be estimated from the *cumulative distribution function* (CDF), as illustrated in figure 2.14a. If the desired quantile is determined as the empirical quantile (here $F^{-1}(0.995) = \hat{x}_{0.995}$) for $p = 0.995$, the density at that point $f(\hat{x}_{0.995})$ can be estimated from the *probability density function* (PDF) as illustrated in figure 2.14b.

2.4.2.1 Extreme value index

The *extrema value index* (EVI) is a measure that characterize the heaviness of the tail in a distribution [52]. One way of estimating EVI based on the order statistic mentioned above is the *moment estimator* described in equation 2.15:

$$\hat{\gamma}_{k+1} = M_{k+1}^{(1)} + 1 - \frac{1}{2}\left(1 - \frac{\left(M_{k+1}^{(1)}\right)^2}{M_{k+1}^{(2)}}\right)^{-1} \ , \tag{2.15}$$

with

$$M_{k+1}^{(l)} = \frac{1}{k}\sum_{i=1}^{k}\left(\log X_{(n-i+1)} - \log X_{(n-k)}\right)^l \ , l = 1, 2 \ , \tag{2.16}$$

where $X_{(n-k)}$ denote the $(k+1)^{\text{th}}$ largest observation.

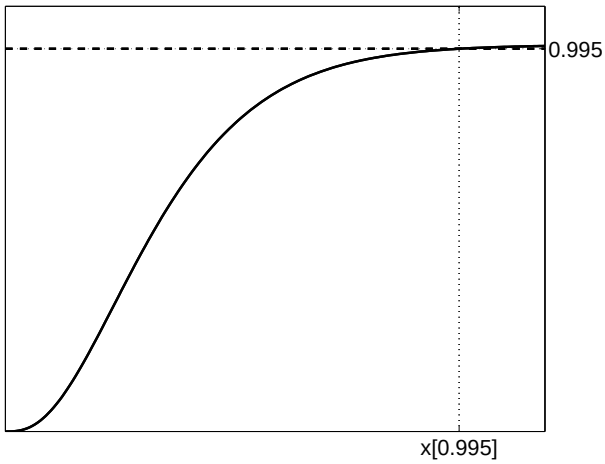

(a) CDF for a theoretical gamma distribution. $x_{0.995\%}$ denote the 99.5 percentile of the distribution.

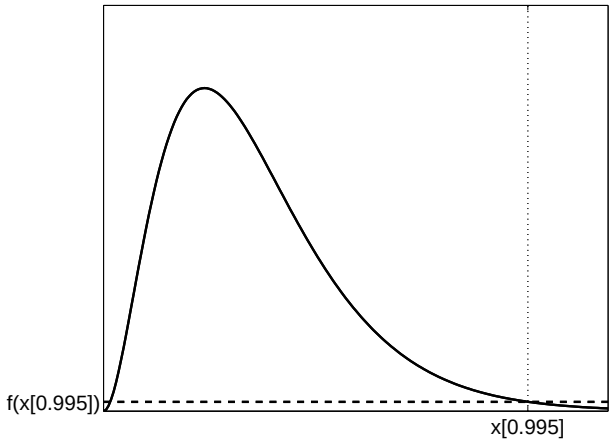

(b) PDF for a theoretical gamma distribution. The density in the point of the quantile is estimated from $f(x_{0.995})$.

Figure 2.14: Illustration of PDF (left) and CDF (right) for a theoretical gamma distribution. Parameters needed in equation 2.14 are emphasized.

Chapter 3

Patients and Methodology

Objective The previous two chapters provided an overview of the biological and technological aspects of treating patients with GBM. This chapter covers the patients as well as the specific methods used through this thesis. First, an overview of the selected patients as well as a description of their course of treatment is given. The second part explains the methods used to evaluate the uncertainties associated with two of the most important image-derived parameters and the third part demonstrate the methods used to characterize a group of patients with GBM as well as their response to therapy. The last part presents two ways to quantify the spatial change in FET uptake during chemoradiotherapy.

3.1 Patients

Two groups of patients contribute to the data that are used in this thesis. The first group is presented in table 3.1 and consists of 20 patients with a suspected cerebral neoplasm that underwent a combined PET/CT scan using a Siemens Biograph64. The patients were part of a larger investigation that seeks to explore the impact of using different reconstruction algorithms and reducing scan time. Approximately 200 MBq of FET was intravenously injected circa 20 minutes prior to the scan. The scans used here were acquired over a 20 minutes period, were reconstructed using 3D OSEM with 4 iterations and 12 subsets and subsequently filtered with a 5mm Gaussian kernel. Images were corrected for radioactive decay, scanner dead time, attenuation, scatter and random events.

		n	%
Gender	Male	15	75
	Female	5	25
Age (median,range)		51.5	24 - 80
Injection to scan time (min) (median,range)		22	17 - 37

Table 3.1: Summary of the 20 patients with a suspected brain tumor that is used in investigation of uncertainties associated with background estimation.

16 patients diagnosed with primary glioblastoma multiforme WHO grade IV constitute the second group that are summarized in table 3.2. All patients were routinely examined with several MRI modalities using a 3.0-T MR scanner, as well as a combined PET/CT using FET. PET images are acquired in the same way as described for the 20 patients in the first group. If possible, patients had tumor reductive surgery. According to neurosurgical reports 4, 12 and 0 interventions were rated as biopsy, partial and gross resection, respectively. All patients were assigned to radiotherapy with concurrent TMZ. GTV was delineated by experienced radiologists from contrast enhancement in the T_1-weighted MR image. *Biological tumor volume* (BTV) was delineated from the FET scan by auto-contouring using a cut-off TBR of 1.6, i.e. uptake that exceeds 1.6 times the background is included. At Rigshospitalet, the background uptake, B, is routinely determined by delineating a large region of healthy tissue above the insular cortex, contralateral to the tumor and averaging the uptake value in a 70% sub-mask within this region, as illustrated in figure 3.1a. BTV was subsequently edited by a physician with expertise in nuclear medicine to exclude non-neoplastic regions with high uptake, such as skin and blood vessels. Edematous areas visible in T_2-weighted MRI were not included in the CTV in contrast to the guidelines provided by ICRU, but a margin of 2 cm was added by the oncologist to the union of GTV and BTV to generate the CTV. An additional margin of 0.5 cm was added by a dosimetrist to define the PTV. A schematic of a planned volume is shown in figure 3.1b. Radiotherapy was planned so that PTV received a total of 60 Gy in 30 fractions, with 5 fractions per week, while sparing critical organs such as the brain stem and optic nerves. An example of a FET-scan fused onto a planning MRI is shown in figure 3.2 together with the corresponding dose plan.

After approximately 20 fractions (median: 19, range: 13-23) of radiotherapy the patient underwent a second PET/CT, using the same parameters as described above. The scans were done on the same scanner model, but not necessarily the exact same scanner. This second, in-treatment scan is co-registered to the pre-treatment scan, using a registration framework in MATLAB developed at the Technical University of Denmark [42]. The registration is performed

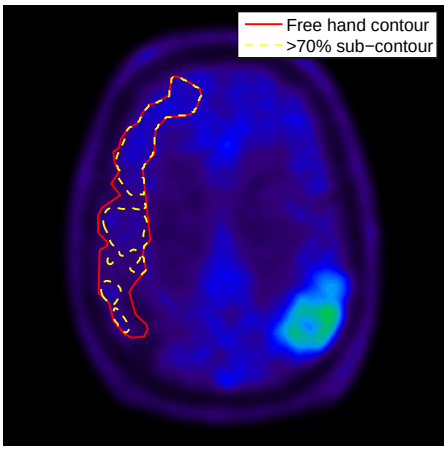

(a) FET scan used to determine background uptake. The conspicuous green mass in the lower right part is a suspected tumor. The outer contour (red) is the contralateral region delineated by an experienced physician. The dashed yellow contour is a sub-mask, including everything above 70% of the maximum. All voxels within the yellow contour are averaged to determine B.

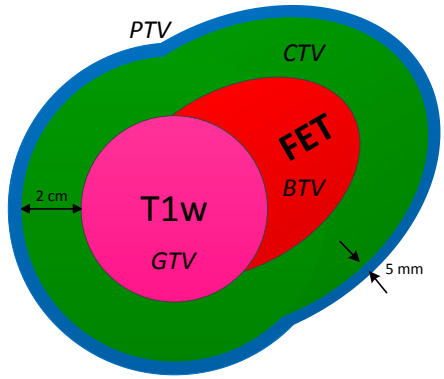

(b) Tumor volume definitions, including the FET positive area, used when planning radiotherapy of patients with GBM at RH. Comparison with figure 2.11, shows that the planning differs from the procedures described by ICRU.

Figure 3.1: a) FET-PET scan showing one slice used for background estimation. Healthy tissue is delineated contralaterally to the tumor. The uptake within a sub-mask of 70% is averaged to determine B. b) Overview of tumor volume definitions used in radiotherapy planning at RH.

using a similarity transform, a normalized cross-correlation as similarity measure and spline interpolation. The registered images are used for evaluation of intermediate tumor response to therapy.

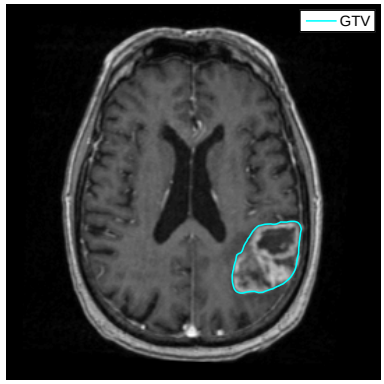

(a) T1-weighted MRI.

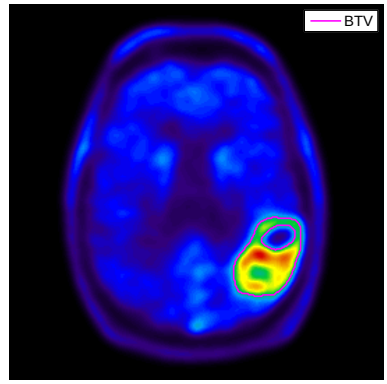

(b) FET image.

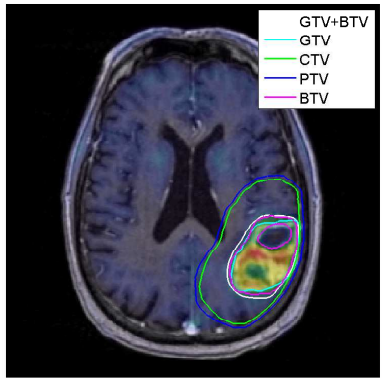

(c) FET image fused onto MRI.

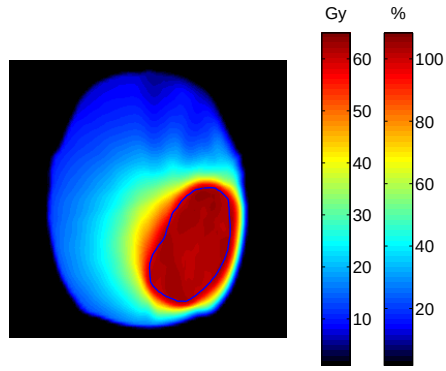

(d) Calculated dose plan based on contours delineated in MRI and PET images. Blue contour shows PTV, which should receive at least 95% of the prescribed dose, as explained in section 2.3.2.1.

Figure 3.2: Planning images acquired prior to radiotherapy. Important tumor volumes are delineated. Note the difference between GTV in (a) and BTV in (b). The two is combined in (c) (white contour), from which CTV and PTV are estimated.

		n	%
Gender	Male	15	93.8
	Female	1	6.2
Extent of resection	Partial	12	75
	Biopsy	4	25
Injection to scan time (min)	Pre-treatment (median,range)	21.1	17.4-24.3
	In-treatment (median,range)	20.6	17.8-32.9
Age (median,range)		57	26-81
Number of fractions (median,range)		19	13-23

Table 3.2: Summary of 16 patients with confirmed GBM.

3.2 Methodology

The methods used to analyze data are divided into three sections. The first section seeks to explore the uncertainties associated with two of the most used parameters, i.e. the background uptake, B, and the TBR. The second part is a characterization of the course and response of the 16 patients diagnosed with GBM, based on parameters extracted from the PET-scans acquired before radiotherapy and during radiotherapy. In section three, the spatial change of the uptake between pre-treatment and in-treatment scans is determined, as an attempt to estimate a margin necessary to include the FET-positive volume during the entire treatment period.

3.2.1 Parameter uncertainties

3.2.1.1 Background

A number of different factors influence the uptake of FET in healthy tissue, which has an impact on the acquired PET images. Table 3.3 lists some of the most predominant factors. The biologic and technologic factors are to some extent controlled by design, e.g. scan duration is kept constant, images are reconstructed using the same parameters, patients are asked to meet fasting, and any uncertainties associated with these are assumed negligible. This section estimates the uncertainties with the two factors that are controlled by the physician, i.e. the use of sub-mask and sensitivity of region contouring. The size of the delineated region is not considered.

Biologic	Injected activity
	Scan duration
	Time from injection to scan
	Patient weight
	Concentration of amino acids
Technologic	Reconstruction
	Partial volume effects
	Inter-scanner variability
Physician	Location of delineation
	Sub-mask
	Size of delineated area

Table 3.3: List of factors that influence the definition of background uptake.

Different sub-masks The cohort of 20 the patients with a suspected brain tumor is used to investigate the uncertainties associated with the definition of uptake of FET in healthy tissue. One hypothesis is that tissue in the insular cortex (II) have a higher background uptake than tissue above insula (AI) due to a higher degree of vascularization. It is investigated whether there is a significant difference in the estimate of B, when delineating healthy tissue II and AI. For this, two lateral regions of healthy tissue, one AI and one in II, have been delineated in the hemisphere opposite of the possible tumor by a trained medical student. The two regions each covered a large part of both grey and white matter in five adjacent slices. The test of significance is performed using one-sided, paired t-tests with a null hypothesis that $\mu_{AI} = \mu_{II}$ against the alternative that $\mu_{AI} < \mu_{II}$. A significance level of 0.05 is used.

Furthermore, the impact of using different sub-masks are investigated. Sub-masks including at least 60%, 70%, 80%, 90% of the maximum value within the hand-delineated volume are used as shown in figure 3.3. The background uptake value, B, is calculated as the average uptake within a given sub-mask. The change in average background value relative to a sub-mask of 70% is calculated across all 20 patients and both locations. The relative change in B was used to estimate the impact on tumor volume, using both rounds of scans from the 16 patients with GBM.

Robustness The background is based on a hand drawn contralateral region, and this might lead to both inter- and intra-observer variability. Due to limited resources, it was not possible to do either a repeated contouring by the same person or delineation of the same region by several persons. Instead, the robustness was investigated by moving the initial contour 4 pixels (3.26 mm) left/right and up/down as a way to simulate worst-case delineation. One of

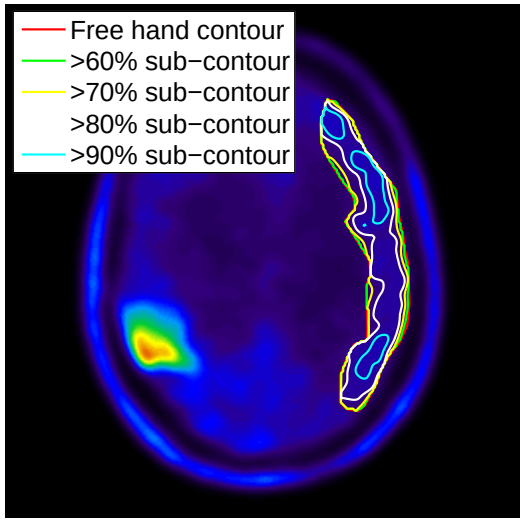

Figure 3.3: FET-PET scan showing one slice used for background estimation. Healthy tissue is delineated contra-laterally to the tumor. The outer contour (red) is the region delineated by a trained medical student. The remaining regions are sub-masks based on this initial contour.

the four locations is illustrated in figure 3.4. For each location the background uptake value was calculated using a 70% sub-mask. The difference between the average of the 4 extreme contours and the reported background was tested using two-tailed, paired t-tests with a significance level of 0.05, again for regions both above insula and in insula.

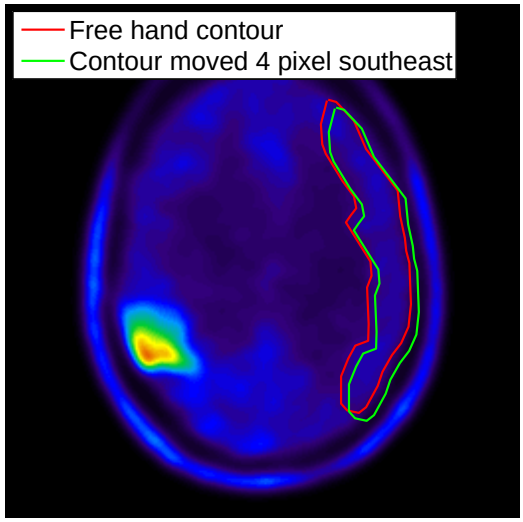

Figure 3.4: Hand-delineated contour shown in red. The green contour is the result of moving the red contour four pixels (3.26 mm) down-right to one of four extreme positions.

3.2.1.2 Tumor-to-brain ratio

As previously mentioned, the TBRs, and especially TBR_{max}, have been subject of much attention in prediction and evaluation of treatment response. Changes in TBR_{max} has proved to be superior to changes in tumor volume determined by MRI, as an indicator of a positive clinical response to therapy [6]. Low pre-treatment TBR_{max} has furthermore been associated with longer PFS [53]. However, the uncertainties with TBR have not been statistically addressed and a change in TBR_{max} of more than 10% has empirically been associated with a positive response. The 10% criterion is established based on the reproducibility of tracer-uptake of another L-tyrosine analogue L-3-[^{123}]iodo-α-methyl tyrosine (IMT). Reproducibility of IMT has been shown to be in the order of 5% [54], hence a change in TBR_{max} of 10% in FET is traditionally considered significant.

This section explores the uncertainties associated with TBR. The maximum uptake value, and hence TBR_{max}, is suspected to be prone to noise and other imaging artifacts, as it is based solely on the value in one maximum voxel . A comparable and potentially more robust measure is the 0.95 fractile, denoted $\text{TBR}_{0.95}$, which is the ratio of B and the voxel that have the 5% highest uptake of FET. Using the concepts of order statistics explained in section 2.4.2, the uncertainties associated with $\text{TBR}_{0.95}$ are estimated. The distribution of TBR was modelled as a gamma distribution, as an attempt to estimate the theoretical 0.95 fractile of TBR, using the methods illustrated in figure 2.14. Another approach based on EVI was also attempted. It has been shown that the distribution above a certain fractile can be approximated by a Generalized Pareto Distribution GPD [55]:

$$g(\hat{x}_{1-p}) \simeq \frac{1}{\hat{\sigma}} p^{1+\hat{\gamma}} \,, \tag{3.1}$$

where $\hat{x}_{1-p}$ is $(1-p)^{\text{th}}$ sample quantile, $\hat{\gamma}$ a moment estimate of the EVI and $\hat{\sigma}$ an estimated scale parameter. See appendix A.1.2 for details and references.

The estimate of the density function obtained in equation 3.1 is inserted into equation 2.14, to get an estimate of the variance, $\hat{\sigma}_{0.95}$ of the 95^{th} percentile. However, the estimate of the variance assumes that observations are identical and independetly distributed, which the voxels in a PET image are not. This was corrected for in two ways: One, by doing a random sub-sampling of voxels in the tumor and secondly by a rough estimate of the true number of uncorrelated voxels in a PET-image, as illustrated in appendix A.1.3.

Based on the two PET scans acquired for each patient, it is individually assessed whether or not the change in $\text{TBR}_{0.95}$ is significant. A significant change in $\text{TBR}_{0.95}$, implies rejection of the null hypothesis that $\hat{x}_{0.95} \leq \hat{y}_{0.95}$. According

to table 2.1 and equation 2.10 the alternative hypothesis is accepted if

$$\frac{(\hat{x}_{0.95} - \hat{y}_{0.95})}{\sqrt{\hat{\sigma}^2_{x_{0.95}} + \hat{\sigma}^2_{y_{0.95}}}} > z_\kappa \ . \tag{3.2}$$

At a 5% level of significance $z_\kappa = 1.645$ and the response to therapy is positive if

$$\hat{y}_{0.95} < \hat{x}_{0.95} - 1.645\sqrt{\hat{\sigma}^2_{x_{0.95}} + \hat{\sigma}^2_{y_{0.95}}} \ . \tag{3.3}$$

Traditionally, changes in TBR are reported in percent relative the pre-treatment observation. Using equation 3.3, the required change in percent for the response to be significant, is given by

$$\Delta_\% \leq \left(\frac{\left(\hat{x}_{0.95} - 1.645\sqrt{\hat{\sigma}^2_{x_{0.95}} + \hat{\sigma}^2_{y_{0.95}}}\right) - \hat{x}_{0.95}}{\hat{x}_{0.95}} \right) \cdot 100\% \ . \tag{3.4}$$

3.2.2 Response characterization

Image-derived parameters have been widely used as a tool when characterizing and predicting response to radiotherapy [6, 8]. Table 3.4 provides an overview of the parameters extracted or estimated from the pre- and in-treatment FET scans. They are divided in two categories: One describing the activity of the tumor and one related to the shape.

Activity		**Shape**
SUV	TBR	
B	$\mathrm{T}_{max}/\mathrm{B}$	FET volume
SUV_{max}	$\mathrm{T}_{mean}/\mathrm{B}$	Convex Hull volume
SUV_{mean}	$\mathrm{T}_{peak_{99.5}}/\mathrm{B}$	Solidity
$\mathrm{SUV}_{peak_{99.5}}$	$\mathrm{T}_{99.5}/\mathrm{B}$	Number of foci
$\mathrm{SUV}_{99.5}$		AUC-IVH

Table 3.4: Overview of extracted and estimated parameters. The two left columns contains activity-related parameters and the right column parameters related to tumor shape.

3.2.2.1 Activity

Tumor activity is characterized by a number of uptake-related parameters. Voxel intensities in the PET images represent the standardized uptake value of the FET-tracer as given by equation 2.2. Estimation of the background, B, is explained in section 3.1 and SUV_{max} is the value of the one voxel within the tumor with highest intensity. $\text{SUV}_{peak_{99.5}}$ is calculated as the average of the 0.5% voxels with the highest uptake. $\text{SUV}_{99.5}$ denote the 99.5 percentile of the uptake distribution, i.e. if the tumor consist of 1000 voxels, $\text{SUV}_{99.5}$ will be equal to the 995^{th} voxel if all voxels were ordered in ascending order. All four SUV-estimates are normalized by B to create the corresponding tumor-to-background ratios (TBR).

3.2.2.2 Shape

Parameters related to the shape of the tumor are presented in the right column of table 3.4. *FET volume* is defined as the volume of the tumor that is FET positive, i.e. the volume included in the BTV as explained in section 3.1. The *Convex Hull* is defined as the smallest, arbitrary polygon that covers all of the FET positive areas. Both the FET positive volumes (FET1 and FET2) and the convex hulls (Ch1 and CH2) are illustrated in figure 3.6a and 3.6b. The *Solidity* represents the ratio of the FET positive volume and the convex hull, as shown in equation 3.5 and is a measure of how dispersed the tumor is.

$$\text{Solidity} = \frac{\text{FET volume}}{\text{Convex hull volume}} \,. \tag{3.5}$$

The *number of foci* is defined as the number of separate FET positive regions using a 26 voxel neighbourhood, meaning that all voxels that touch either at a face, edge or a corner are considered to be connected. The area under the *intensity-volume histogram* (IVH) is proposed as a way to quantify the heterogeneity of the tumor uptake [9, 56]. The area under the curve of the IVH is abbreviated *AUC-IVH*. The concept is adapted from the DVH and the IVH illustrates the volume fraction of the tumor with an SUV higher than a certain value. A simulation of theoretical tumor distributions is shown in figure 3.5a as well as the resulting IVH's. A homogeneous tumor, as shown in the upper left part of figure 3.5a, results in an AUC-IVH of 100, since the area below the blue curve in 3.5b is equal to 100.

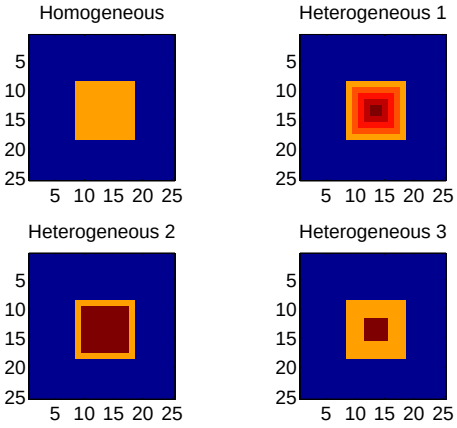

(a) Four theoretical tumor distributions.

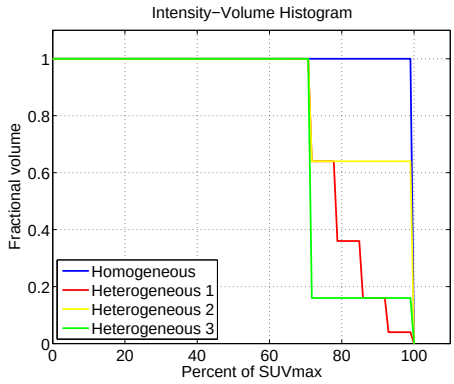

(b) Intensity-volume histogram of theoretical tumor distribution. The yellow, red and green curve represent decreasing AUC-IVH, which by comparison to their corresponding distributions is a result of increased heterogeneity.

Figure 3.5: Simulation of different tumor distributions and their corresponding intensity-volume histograms. AUC-IVH decreases as tumor heterogeneity increases.

3.2.2.3 Parameter correlation

The correlation between a number of the extracted parameters was calculated. Especially, the correlation between ΔTBR_{max} and $\Delta\text{TBR}_{0.95}$ is of interest, since it is argued that the latter is an equally powerful, yet more robust indicator of tumor response to therapy. Four parameters, $\text{TBR}_{0.95}$, TBR_{mean}, Solidity and AUC-IVH estimated from the pre-treatment scan were correlated with $\Delta\text{TBR}_{0.95}$ as an attempt to identify features that potentially can predict treatment response. $\text{TBR}_{0.95}$ and TBR_{mean} were selected since TBR_{max} and TBR_{mean} earlier has been associated with good clinical outcome [6, 53]. The correlation between $\Delta\text{TBR}_{0.95}$ and solidity and AUC-IVH, respectively, is interesting since these parameters characterize the spatial uptake distribution.

3.2.3 Spatial change

This section presents the method used to quantify the spatial change in FET-uptake. Since tumors on some occasions are widely dispersed, the margin estimate is based on the difference between the volume of the pre-treatment convex hull and the in-treatment FET positive volume, as illustrated by the white contour in figure 3.6a and the red contour in figure 3.6b. Illustration of the margin estimate is presented in figure 3.6c. Both an *average distance* (AD) as well as the *maximum distance* (MD) are calculated for both approaches, as given by equation 3.6 and 3.7, respectively.

$$AD = \frac{1}{N}\sum_{j=1}^{N} \eta \cdot d\left(B_P, B_{I_j}\right) \tag{3.6}$$

$$MD = \max_{j}\left(\eta \cdot d\left(B_P, B_{I_j}\right)\right) \tag{3.7}$$

with

$$\eta = \begin{cases} 1 & \text{for} \quad B_{I_j} \in B_P^c \cap B_I, \\ 0 & \text{else} \end{cases} \tag{3.8}$$

where B_P are the border voxels for the pre-treatment convex hull and B_I the border voxels for the in-treatment FET volume. N denote the number of in-treatment boundary voxels and $d(\cdot,\cdot)$ returns the minimum Euclidean distance between two sets of voxels. $B_P^c \cap B_I$ is the relative complement of B_P in B_I, hence the quantity η ensures that distances are only included in case the tumor has expanded from pre-treatment to in-treatment scan, as is illustrated in figure 3.6c. The correlation between AD and the number of fractions before FET2 was investigated.

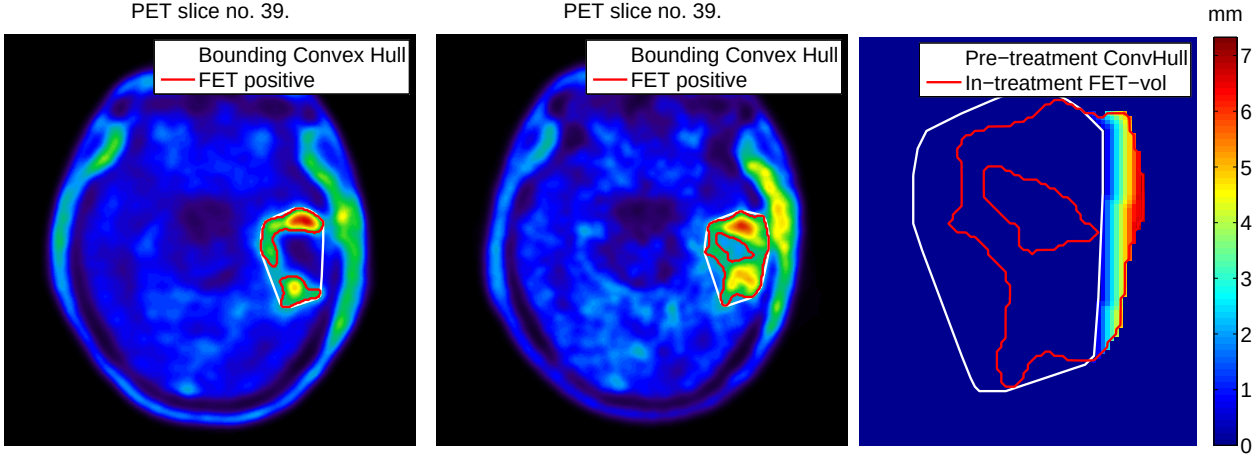

(a) Pre-treatment FET scan. The red contour delineates the FET positive volume and the white contour is the convex hull.

(b) In-treatment FET. The red contour delineates the FET positive volume and the white contour is the convex hull.

(c) Colormap shows the spatial displacement in millimetres from pre-treatment convex hull to in-treatment FET volume. The white contour is the convex hull from (a) and the red contour is the FET positive volume from (b).

Figure 3.6: Estimates of spatial change. The difference between the convex hull of the pre-treatment FET scan and the FET positive volume of the in-treatment scan er investigated. Top row shows the same slice of the pre-treatment and in-treatment scan, respectivel. Bottom figure shows the estimated spatial change in milimeters. Note, only the border voxels of the red contour are included in estimation of AD and MD.

It was furthermore visually investigated whether or not the FET positive area remained within the 95% isodose at the time of the in-treatment scan.

Based on the margin estimates, the probability of including the FET positive volume at the time of the in-treatment scan, is empirically determined as a function of millimeter margin as described by equation 3.9.

$$P(mm) = \frac{F_I}{CH_P(mm)} \,, \tag{3.9}$$

where F_I is the FET positive volume of the in-treatment scan and $CH_P(mm)$ is the convex hull of the pre-treatment scan, expanded by mm millimeters. A 95% confidence interval about the estimated mean fraction is calculated using equation 2.13.

Chapter 4

Results

Objective This chapter presents the results obtained in three different sections. The first sections presents estimates of the uncertainties associated with evaluation of FET scans, the second section deals with the parameters extracted from the two sets of scans of 16 GBM patients and the last section treats the spatial change in FET uptake over a period of approximately four weeks of chemoradiotherapy.

4.1 Parameter uncertainties

As described in section 3.2.1, one goal of this project was to investigate the uncertainties associated with two central parameters in treatment and evaluation of patients with GBM, namely uptake in healthy tissue and the ratio between the tumor and background.

4.1.1 Background

Only factors that are controllable by the physician when estimating the uptake in healthy tissue are evaluated here. A discussion of all the parameters influencing B, is provided in section 5.2.1.

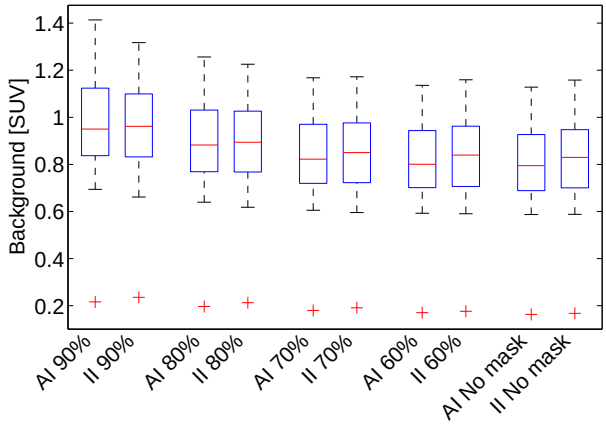

Figure 4.1: Result of using different sub-masks when estimating background uptake value. The subscripts AI and II denote the region above insula and in insula, respectively.

Different sub-masks

The result of using sub-masks of 90%, 80%, 70% and 60% when estimating background uptake is shown in table A.1 in appendix and summarized in figure 4.1. Worth noticing is that the background estimate decreases as sub-mask percentage decreases. Testing the differences between B when determined above insula and in insula, revealed that the difference is significant for sub-masks of 70% and below at a 0.05 level of significance. p-values and the relative difference are presented in table 4.1. The relative change between estimates AI and II is noted to be around 2%.

The overall effect of using different sub-masks were quantified by averaging over all patients and both regions. The result is shown in table 4.1 relative to using a 70% sub-mask. It is noticed that increasing the sub-mask level increases the estimated background value and reduces the estimated tumor volume.

Robustness

The estimate of the sensitivity of the hand-delineated contour is shown in table A.2 in appendix. Figure 4.2 shows a Bland-Altman plot of the reported background and the average of the four extreme positions. It is noted that the difference means were close to zero and hypothesis tests revealed that the difference is insignificant both AI and II ($p = 0.92$ and $p = 0.32$, respectively).

sub-mask	Change B [%]	Change volume [%]	p-value $\mu_{\mathbf{AI}} < \mu_{\mathbf{II}}$	$\frac{\mathbf{II}-\mathbf{AI}}{\mathbf{AI}} \cdot 100\%$
90%	14.0	-40.4	0.45	0.78
80%	5.31	-17.7	0.17	1.1
70%	0	0	0.01	1.5
60%	-2.27	8.44	0.001	1.9
No mask	-3.46	13.0	>0.001	2.6

Table 4.1: Table showing the average change in background, B, across all patients and regions as well as the resulting average tumor volume. The changes are shown relative to using a sub-mask of 70%. The fourth column shows the p-value for testing the hypothesis that $\mu_{AI} < \mu_{II}$ and the rightmost column shows the average difference between B_{AI} and B_{II}.

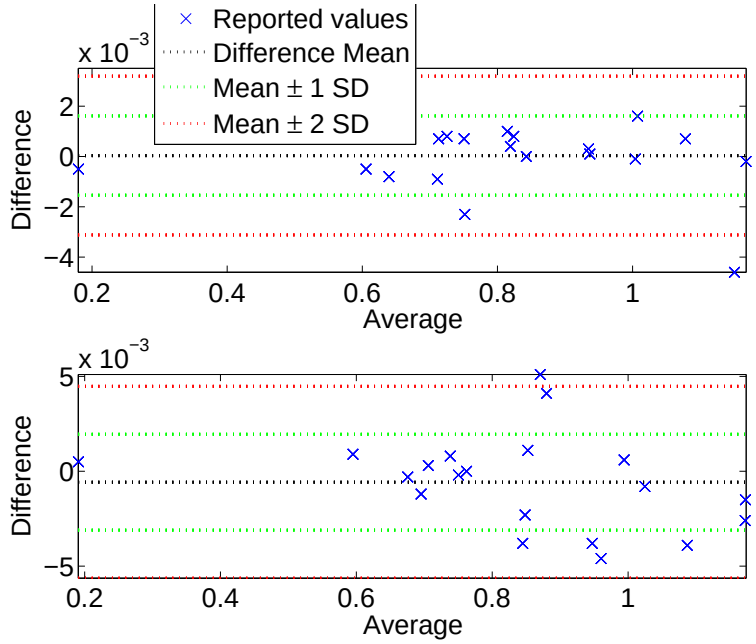

Figure 4.2: Bland-Altmann plot for reported background value versus estimated background in four extreme positions. Both tumors above insula (top) and in insula (bottom) are tested. A two-sided paired t-test are used to revealed that the difference is not significantly different from zero, neither AI nor II.

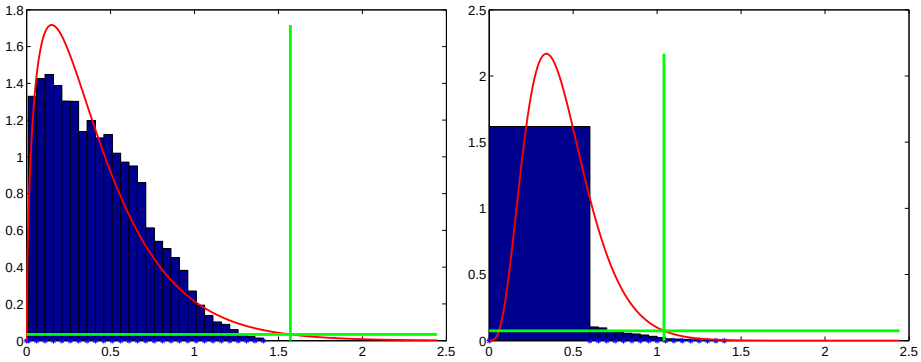

(a) Gamma fit of tumor distribution. The distribution is shifted to zero before the fitting.

(b) Gamma fit of tumor distribution with modified bins.

Figure 4.3: Gamma fit of tumor uptake distribution. Blue bars show the frequency of observed TBR's within a given bin and red curves show the corresponding gamma fit. The vertical green and horizontal green line mark the sample quantile ($x_{0.995}$) and density (f($x_{0.995}$)).

4.1.2 Tumor

To investigate uncertainties associated with the TBR_{95}, histograms showing the distribution of TBR's were created. The initial idea was to fit a gamma distribution to the data using maximum likelihood estimates and exploit the concepts explained in section 2.4.2. The result of such a fit is shown in figure 4.3a. The red curve shows the best fit of the data using maximum likelihood estimates. The vertical green line, illustrates the TBR_{95} determined from the red curve and the intersecting green line shows the estimate of the density. It is noted that the distribution of TBR obviously does not follow a gamma distribution. Another thing to notice is that the histogram of TBR is not very smooth, but has several shoulders indicating a heterogeneous distribution. Equation 2.14 requires only that the density function is known in the given sample quantile, hence it was investigated if modifying the bin size of the histogram would improve the fit around the sample quantile, but as is apparent in figure 4.3b, this was not the case. Alternatively, the variance of TBR_{95} was calculated by the moment estimator as explained in section 3.2.1.2. The distribution of TBR and the empirical TBR_{95} for the pre-treatment and in-treatment scan is shown for one patient in blue and red, respectively, in figure 4.4.

To evaluate whether the treatment had worked so far, it was tested whether the change in TBR_{95} was significant at a 0.05 level of significance, using equation 3.3.

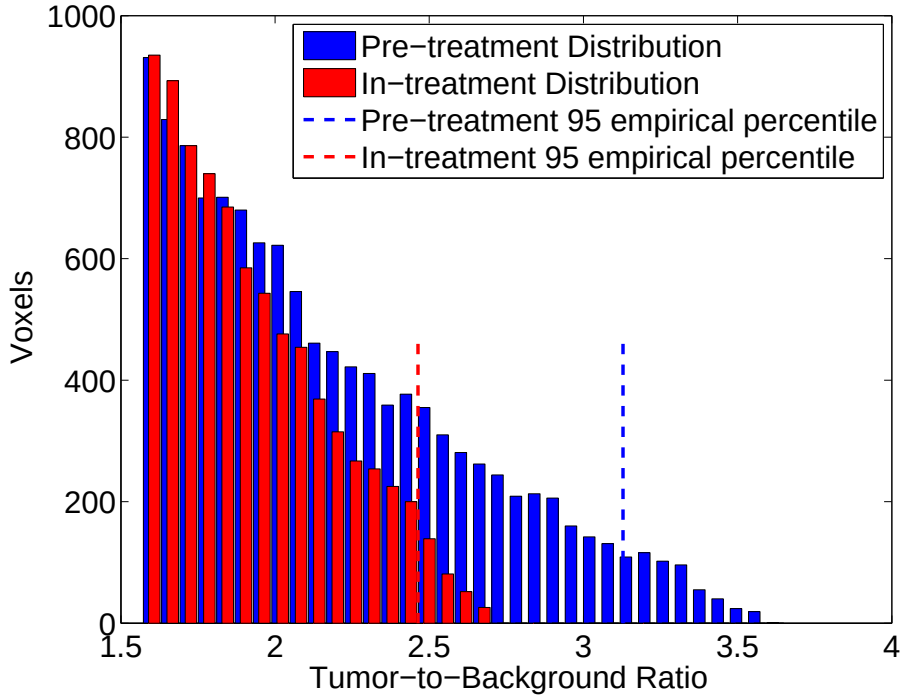

Figure 4.4: Histograms of tumor distributions. Blue bars show pre-treatment and red bars in-treatment. The dashed line marks TBR_{95}.

Graphically this means testing whether or not the red dashed line in figure 4.4 was significantly further to the left than the blue dashed line. The estimated TBR_{95}, the associated variance, the number of voxels in the tumor and the required as well as the actual percentage change are shown in table 4.2. The estimate of the variance in equation 2.14 assumes that voxels are uncorrelated. Compensation for this was attempted by doing a randomly sub-sample 1000 voxels in the tumor, but this lead to erroneous estimates of the EVI. Instead, a rough estimate of ratio between the total number of voxels and the effective number of uncorrelated voxels, was according to section A.1.3 in appendix found be 600:1. This is used correct the listed variance.

The required change, for the response to be considered significant, was calculated as the percentage in change TBR_{95} as shown in equation 3.4. The tumor for patient number 12 consisted only of 132 voxels at the time of the in-treatment scan and was excluded in the average estimates. The estimated standard deviation of TBR_{95} is 0.248 for the pre-treatment scans and 0.131 for the in-treatment scans. The analysis showed a significant reduction in TBR_{95}

in 4 of 16 patients and the average required change was -24.13%.

Patient	$\mathbf{TBR_{95_X}}$	$\hat{\sigma}_{\mathbf{x0.95}}$	$\mathbf{n_X}$	$\mathbf{TBR_{95_Y}}$	$\hat{\sigma}_{\mathbf{y_{0.95}}}$	$\mathbf{n_Y}$	Required Change [%]	Actual Change [%]	Response
1	2.442	0.174	13378	2.533	0.109	22282	-13.84	3.75	N
2	2.601	0.319	17992	2.788	0.256	16776	-25.87	7.17	N
3	2.724	0.288	10779	3.241	0.277	24421	-24.17	18.98	N
4	2.227	0.182	18078	2.397	0.357	8717	-29.61	7.67	N
5	2.781	0.162	28395	2.334	0.278	23910	-19.02	-16.07	N
6	2.678	0.095	33118	2.195	0.072	17669	-7.32	-18.03	P
7	3.627	0.213	27155	3.067	0.104	27276	-10.75	-15.44	P
8	2.080	0.135	8341	2.319	0.109	20813	-13.67	11.44	N
9	2.840	0.698	3774	2.953	0.795	3661	-61.30	3.98	N
10	3.128	0.257	11973	2.464	0.136	8025	-15.29	-21.25	P
11	2.280	0.106	24480	2.356	0.133	26024	-12.26	3.33	N
12	1.963	0.342	1797	1.918	0.942	132	-83.98	-2.30	N
13	3.535	0.391	14691	2.947	0.241	16466	-21.39	-16.64	N
14	3.099	0.261	17069	2.368	0.113	16826	-15.09	-23.59	P
15	2.453	0.197	18984	2.751	0.228	25432	-20.21	12.16	N
16	2.549	0.140	15482	2.689	0.131	20160	-12.37	5.50	N
Average	**2.688**	**0.248**		**2.583**	**0.268**		**−24.13**	**−2.46**	

Table 4.2: Table showing the result of statistical analysis of a sub-maximal TBR. X denote the pre-treatment and Y the in-treatment. TBR_{95_X} and TBR_{95_Y} are the percentile estimates, and $\hat{\sigma}_{x0.95}$ and $\hat{\sigma}_{y0.95}$ the corresponding standard deviations. Required change is defined as the change TBR_{95} in percent, necessary to produce a significant difference at a 5% level of significance. Response (N=negative, P=positive) is the result of evaluating the actual change against the required change. Patient number 12 is not included in the average estimations for reasons discussed in section 5.

4.2 Response characterization

As mentioned in chapter 3, each patient diagnosed with GBM received PET/CT scans using FET once before treatment and once during treatment. Both activity related parameters as well as tumor shape parameters are extracted for each patient from both rounds of scans.

4.2.1 Image derived parameters

This section presents the image derive parameters described in section 3.2.2.1 and 3.2.2.2. A summary of the population average is listed in table 4.3. The first eight rows show the raw SUV measures extracted from the images. The following eight rows the corresponding TBR. The last part of the table lists the shape-related parameters. Parameters for each patient is provided in section A.2 in appendix.

4.2.2 Response evaluation

This section characterize the intermediate response after two-thirds of planned chemoradiotherapy. Visualization of the response for each patient is provided in section A.3 in appendix. Figure 4.4 showed an example of the entire change in TBR distribution. Another illustration of response is provided in figure 4.5 for the patient shown in figure 3.6. Figure 4.5a shows a response map with areas that have responded as well as areas where the tumor has progressed. Figure 4.5b shows an IVH of the two scans, illustrating that the tumor has become more homogeneous, since the area under the red curve is larger than the area under the blue curve.

The percentage change in SUV for each patient as well as the overall change in the population is shown in figure 4.6. Similarly, figure 4.7 shows the change in TBR and figure 4.8 the change in shape parameters. The boxplots show the median (central red mark), the 25^{th} and 75^{th} percentiles (lower and upper edge, respectively) and the whiskers extend to the most extreme datapoints not considered outliers. One thing to notice is that on average, all SUV parameters have increased from first to second scan, including the background (figure 4.6b), while change in TBR's are more evenly distributed around zero (figure 4.7b). Another thing to notice is the length of the boxes in figure 4.7b, indicating that there is a large spreading in TBR's. The change overall change in each parameter is listed in table 4.4.

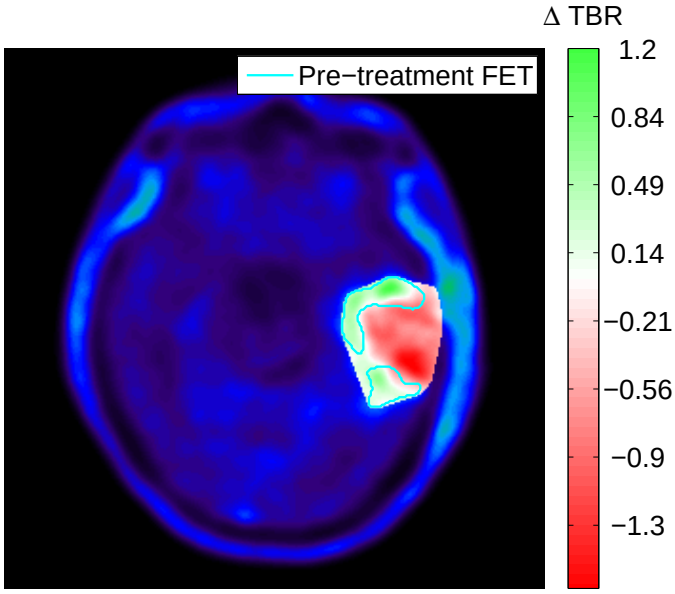

(a) Map showing the response in one slice. Green areas are those where the response is positive, and red the areas where the tumor has progressed.

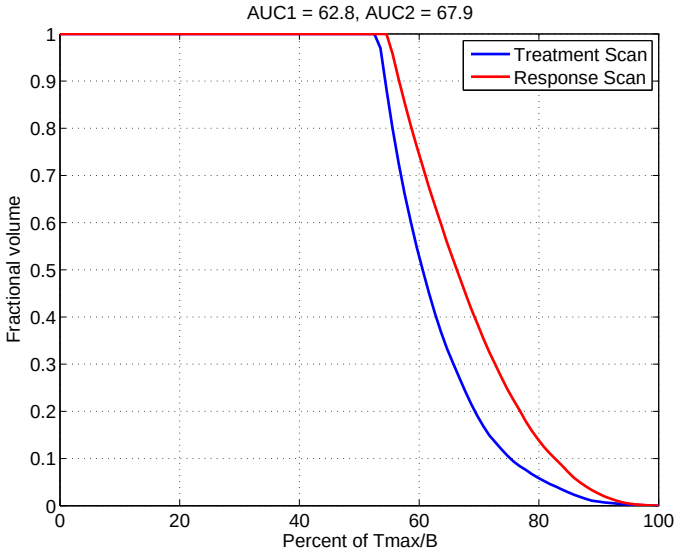

(b) Intensity-volume histogram of the tumor in the pre-treatment scan (blue) and in-treatment scan (red). The IVH is moved towards the upper right corner, indicating that tumor has become more homogeneous.

Figure 4.5: Illustration of response to therapy based on the pre-treatment and in-treatment scan shown in figure 3.6

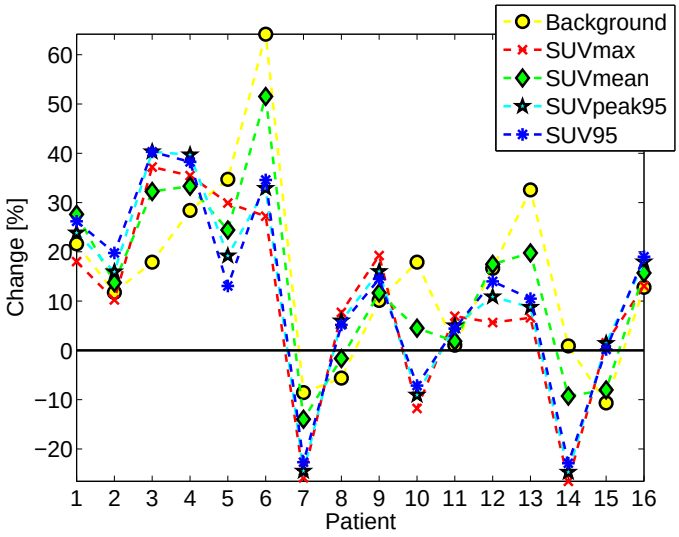

(a) Response plot.

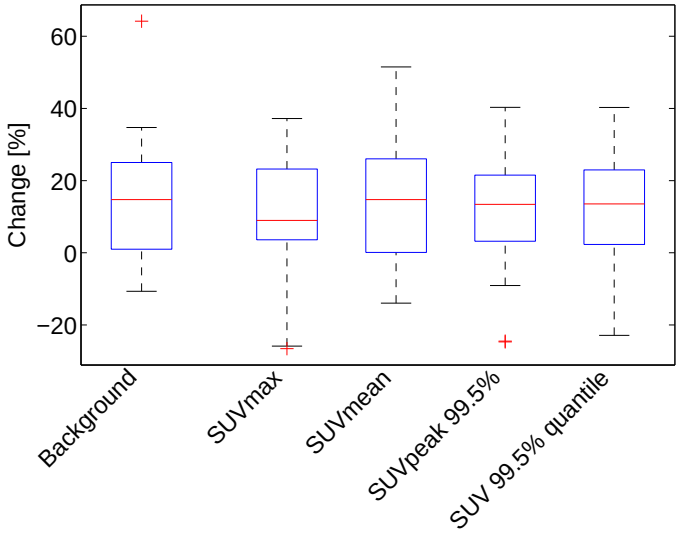

(b) Boxplot of response in population.

Figure 4.6: Change in raw SUV relative to pre-treatment scan. a) Change in SUV for each patient. b) Percentage change in population.

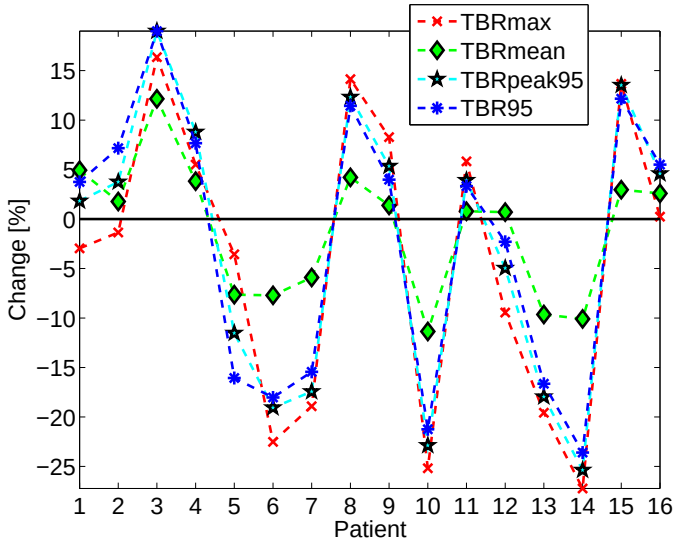

(a) Response plot.

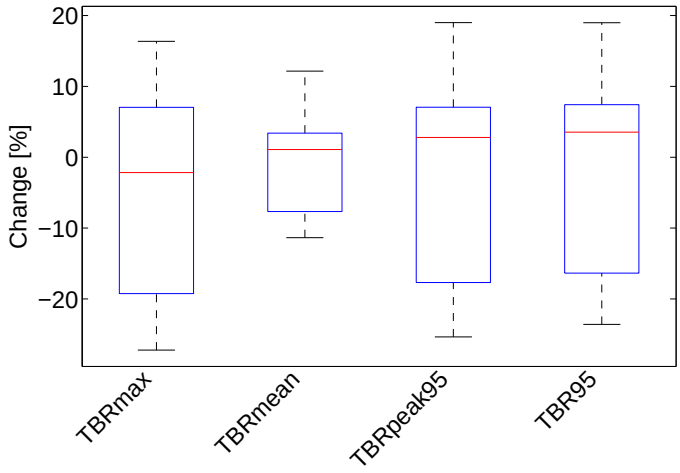

(b) Boxplot of response in population.

Figure 4.7: Change in TBR relative to pre-treatment scan. a) Change in TBR for each patient. b) Percentage change in population.

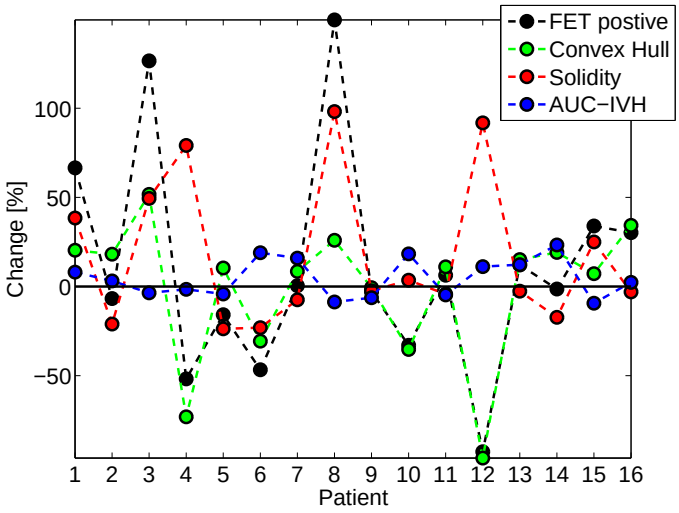

(a) Response plot of shape parameters.

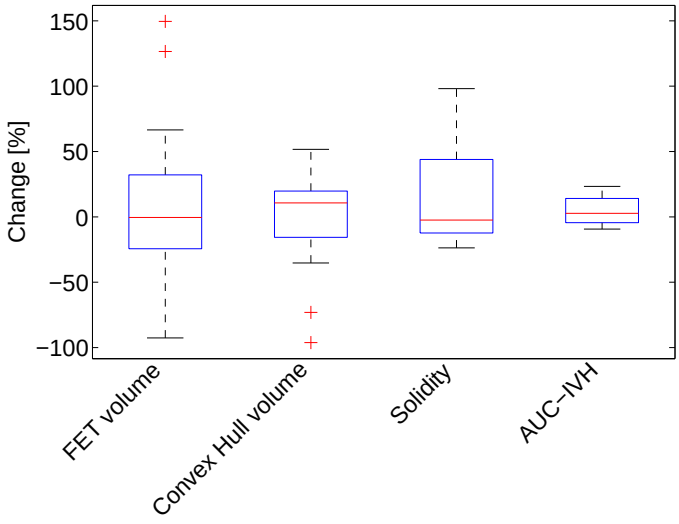

(b) Boxplot of response in population.

Figure 4.8: Overview of change in shape parameters from pre-treatment and in-treatment scans. a) Percentage change for each patient. b) Average change in population.

			Median	Range
SUV	**Pre-treatment**	SUV_{max}	2.5	1.70 - 4.09
		SUV_{mean}	1.56	1.26 - 2.37
		$SUV_{peak_{95}}$	2.17	1.54 - 3.67
		SUV_{95}	2.05	1.48 - 3.44
	In-treatment	SUV_{max}	2.84	1.83 - 4.12
		SUV_{mean}	1.81	1.24 - 2.44
		$SUV_{peak_{95}}$	2.51	1.63 - 3.60
		SUV_{95}	2.35	1.55 - 3.36
TBR	**Pre-treatment**	TBR_{max}	3.24	2.17 - 4.50
		TBR_{mean}	1.98	1.73 - 2.38
		$TBR_{peak_{95}}$	2.86	2.05 - 3.87
		TBR_{95}	2.64	1.96 - 3.63
	In-treatment	TBR_{max}	3.00	1.97 - 4.06
		TBR_{mean}	1.96	1.74 - 2.24
		$TBR_{peak_{95}}$	2.63	1.95 - 3.51
		TBR_{95}	2.50	1.92 - 3.24
Shape	**Pre-treatment**	FET positive [cm^3]	32.4	3.58 - 65.9
		Convex Hull [cm^3]	47.6	7.02 - 128
		No. of Foci	1	1 - 7
		Solidity	0.60	0.31 - 0.93
		AUC IVH	61.0	52.7 - 79.4
	In-treatment	FET positive [cm^3]	37.7	0.26 - 54.3
		Convex Hull [cm^3]	53.9	0.27 - 127
		No. of Foci	1	1 - 4
		Solidity	0.74	0.37 - 0.98
		AUC IVH	64.0	52.0 - 88.2

Table 4.3: Uptake summary based upon 16 patients with glioblastoma multiforme.

4.2.3 Parameter correlation

Traditionally, TBR_{max} has been used as the parameter to predict and evaluate response to therapy. It was previously argued that TBR_{95} shared the same properties, but with a lower variance. The relationship between ΔTBR_{max} and ΔTBR_{95} is visualized in figure 4.9 and shows a strong correlation ($r = 0.987$). The correlations between a number of selected pre-treatment parameters and ΔTBR_{95} have been analyzed as an attempt to identify any prognostic factors that potentially would predict the response to therapy. The parameters with the strongest correlation to ΔTBR_{95} were pre-treatment TBR_{95}, TBR_{mean}, solidity and AUC-IVH, which have been plotted against ΔTBR_{95} in figure 4.10. The

			Median	Range
Change [%]	**Raw SUV**	ΔSUV_{max}	8.98	−27 - 37
		ΔSUV_{mean}	15	−14 - 52
		$\Delta SUV_{peak_{95}}$	13.4	−25 - 40
		ΔSUV_{95}	14	−23 - 40
	TBR	ΔTBR_{max}	−2.16	−27 - 16
		ΔTBR_{mean}	−1.1	−11 - 12
		$\Delta TBR_{peak_{95}}$	2.8	−25 - 19
		ΔTBR_{95}	3.5	−24 - 19
	Shape	FET positive	−0.49	−92.7 - 150
		Convex Hull	10.7	−96.2 - 51.2
		No. of Foci $[n]$	0	−6 - 3
		Solidity	−2.50	−23.7 - 98.1
		AUC IVH	2.73	−9.34 - 23.3

Table 4.4: Overall change in image derived parameters.

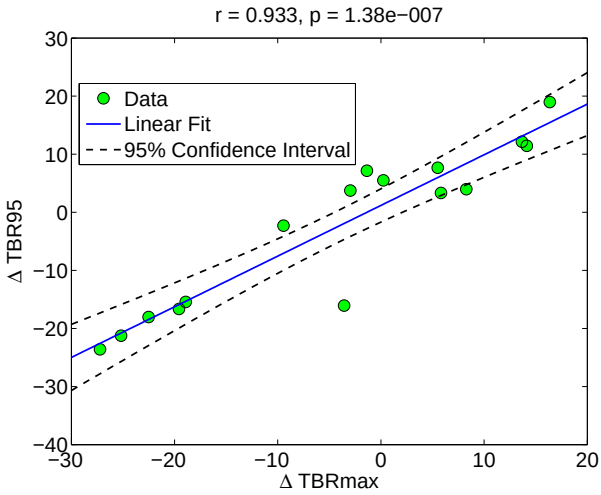

Figure 4.9: Relationship between ΔTBR_{max} and ΔTBR_{95}. A correlation of $r = 0.987$ is noted.

strongest correlation is seen for TBR_{mean}, as a high ratio is correlated with a large decrease in TBR_{95}. Even though less pronounced, negative correlations are noted for solidity and TBR_{95} as well, while AUC-IVHs show a small positive, but insignificant, correlation with ΔTBR_{95}.

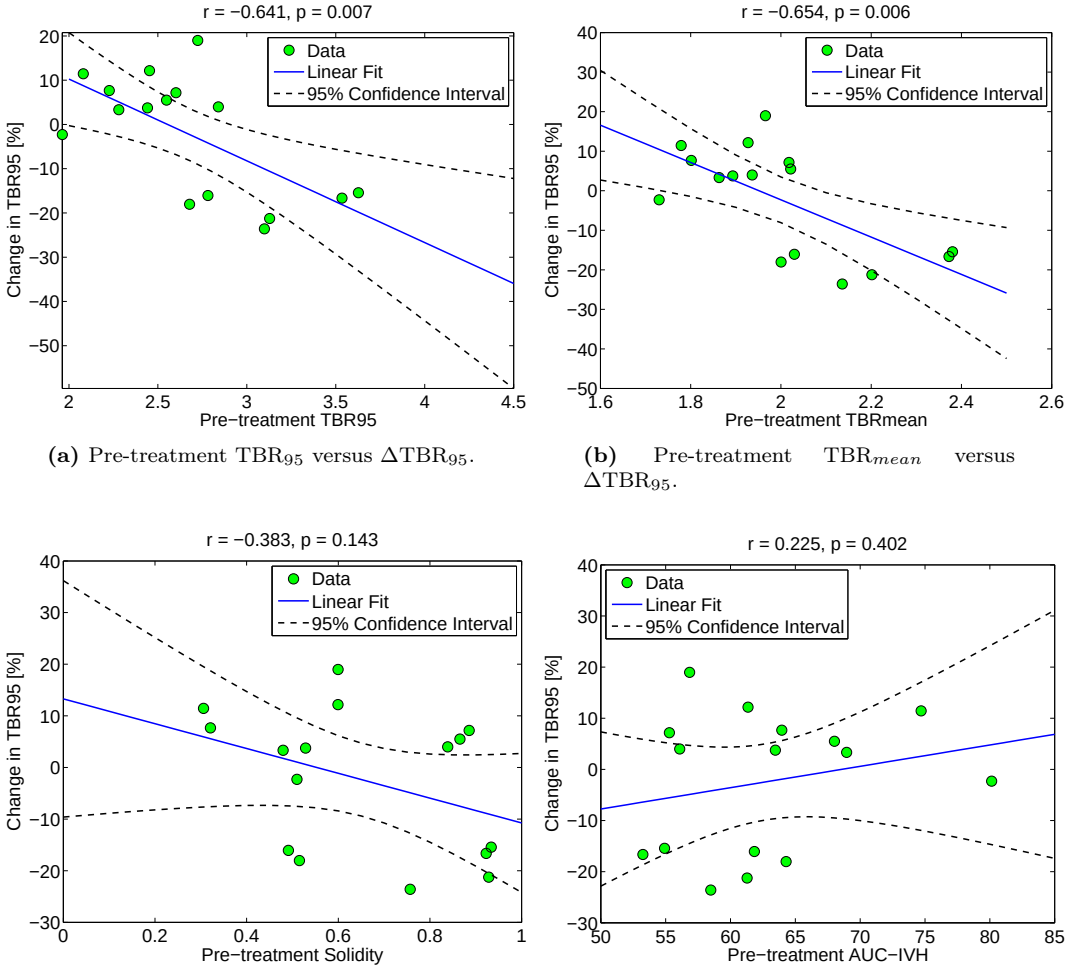

(a) Pre-treatment TBR_{95} versus ΔTBR_{95}.

(b) Pre-treatment TBR_{mean} versus ΔTBR_{95}.

(c) Pre-treatment Solidity versus ΔTBR_{95}.

(d) Pre-treatment AUC-IVH versus ΔTBR_{95}.

Figure 4.10: Correlation between ΔTBR_{95} and four image-derived parameters from pre-treatment FET scans.

4.3 Spatial change

The average distance and maximum distance between the pre-treatment convex hull and the in-treatment FET positive volume are shown in the second and fourth column of table 4.5. It is noted, that the AD across all patients is 3.29 mm with a standard deviation of 2.22. A 95% confidence interval on the AD was found to be 2.11-4.47 mm. No significant correlation between AD and the number of fractions was found, neither between AD and the days between scans.

Large maximum distances are required in some patients, especially patient 1, 2 and 8. A visual analysis revealed that the tumor had outgrown the 95% isodose in 5 of 16 patients. Figure 4.11 shows a cumulative graph of the margin necessary to fully include a given number of tumors. The average fraction of FET2 that is included in CH1 is determined as described by equation 4.12 and visualized in figure 4.12. The figure shows that, on average, a 5 mm margin is required to include 95% of FET2 at the time of the second scan.

Patient	**External Margin [mm]**			**FET2 within 95% isodose**
	AD	SD from AD	MD	
1	5.11	3.61	20.48	Y
2	7.34	10.11	37.45	N
3	3.92	1.86	9.61	Y
4	2.49	1.38	6.43	Y
5	2.74	1.88	10.12	Y
6	1.39	0.84	3.51	Y
7	1.72	0.91	4.39	N
8	5.92	3.58	18.47	Y
9	4.04	1.94	9.07	Y
10	1.68	0.81	4.89	Y
11	2.03	1.31	9.48	N
12	2.71	1.22	4.50	Y
13	2.96	1.26	6.89	N
14	3.49	2.07	10.01	Y
15	2.64	1.42	7.36	N
16	2.43	1.27	6.00	Y
Average	3.29	2.22		N: 5, Y: 11

Table 4.5: Margin estimates calculated as differences between convex hull of pre-treatment scan and FET positive volume of in-treatment scan. AD denote the average distance and MD the maximum distance. SD is the standard deviation of the AD. The rightmost column list the tumors that remain within the 95% isodose at the time of the in-treatment scan (Y: yes, N: no).

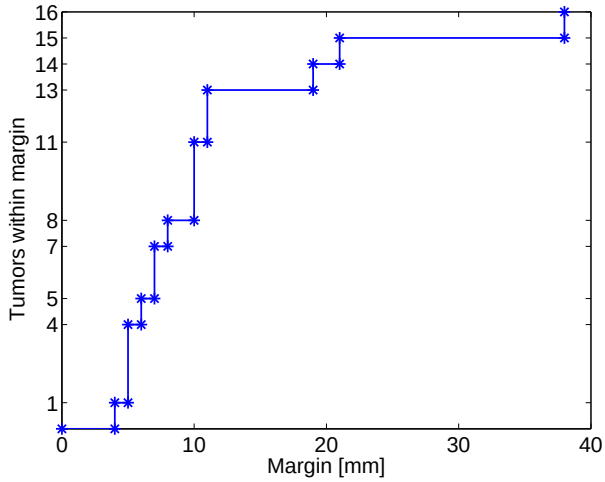

Figure 4.11: Cumulated curve, showing the required margin added to the pre-treatment convex hull in order to include the in-treatment FET positive volume.

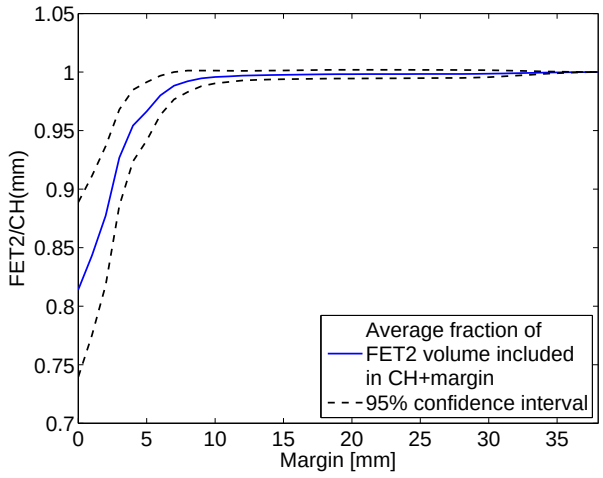

Figure 4.12: Average fraction of FET2-volume within convex hull volume of FET1 as a function of milimeter margin. The dashed lines show the estimated 95% confidence interval.

Chapter 5

Discussion

5.1 Patients

Two groups, with a total of 32 patients, contributed to the data analyzed in the foregoing. The hand-delineated regions are not routinely exported, which was the reason why the 16 patients with GBM were not included in the background estimation. The 20 patients that did contribute to the background estimates were scanned using the same parameters as the patients with GBM, hence the obtained results were directly applicable. Only one female was included in the cohort of patients with GBM, which is unexpected since the average male-female ratio is 3:1 [3]. There is no obvious explanation to this. The neurosurgical reports revealed that four patients had a biopsy and 12 had partial tumor resection, whereas none was rated as a gross total resection. The definition of *extend of resection* varies across different hospitals which complicates comparison of neurosurgical findings. At RH a brain tumor resection is rated as "gross total" if there is no contrast enhancement in the subsequent PET scan, which apparently was not the case in any of these 16 patients.

5.2 Parameter uncertainties

As explained in section 3.2.1 the uncertainties associated with B and TBR_{95} were investigated. The results were presented in section 4.1.1 and 4.1.2 and is discussed in the following.

5.2.1 Background

Determination of uptake in healthy tissue is important, since tumor delineation, dose planning and subsequent evaluation are based on this parameter. The factors that influence the uptake were listed in table 3.3 and only two factors related the physician were investigated. Biological and technological factors were assumed to be negligible. The injected activity and the scan duration is kept of the same level for every patient in both pre-treatment and in-treatment scan. It was shown in figure 2.7, that the uptake of FET in brain tumors reaches a plateau after approximately 20 minutes, hence it was striven to keep the time from injection to the beginning of each scan around 20 minutes. This was more or less accomplished as seen in table 3.2. This might seem like a parameter that is easy to control, but it is often complicated by the general work-flow in the clinic.

Patient related parameters, such as the body weight and blood concentration of amino acids might be the parameters that are most difficult to control. Many patients do not know their exact weight and they are not routinely weighed by clinical personnel. Patients are required to arrive fasting, but this is sometimes a problem for patients in general, and since large brain tumors sometimes impair cognition, the compliance might be further degraded. Background definition is based on a large delineated region, which reduce the effect of partial volume. The impact of varying the size of the delineated area was not investigated, but it is expected that delineating a large region in five adjacent slices is a rather robust method, since a large number of voxels is included.

The effect of varying the level of the sub-mask is illustrated in figure 4.1. The reason for using a sub-mask, is that the delineated region will contain both brain tissue and the *cerebrospinal fluid* (CSF) that surrounds the brain tissue in which there is no FET uptake. Averaging a region based on a sub-mask ensures that B is a more precise measure of the uptake in the tissue only. It was noticed that the background estimate decreased as the sub-mask level decreased. The reason for this, is that the sub-mask is based on the one voxel with highest value within the hand-delineated region. Increasing the level of the sub-mask implies that the size of the sub-mask is reduced, which was seen in figure 3.3, and fewer voxels, but with higher intensity, is included in the estimation. The relative effect to using a 70% sub-mask was listed in table 4.1 and was quite pronounced, especially when using a 90% sub-mask. These differences demonstrate that the size of the sub-mask is pivotal in determination of B, and that it is a subtle balance between excluding regions with CSF, while not favoring high uptake regions.

The sensitivity of B was addressed by moving the initial contour to four extreme positions and comparing the average in these four regions to the reported

B. No significant difference was found, indicating that the method of determining B within a 70% sub-mask is rather robust. This seems reasonable, since the sub-mask probably is not that sensitive to displacement of the hand-delineation. Moving the initial contour to four extreme positions might not be comprehensive enough to say something definitive about the robustness, since averaging differences in the four positions in theory could diminish the true difference.

It was furthermore investigated whether there was a difference when determining B in a region above insula and a region in the insular cortex. Testing revealed a significant difference when using a sub-mask of 70% or below. However, the difference was found to be less than two percent, which will probably not have a large clinical impact, since PET examinations in general are associated with larger uncertainties.

In summary, the estimation of B using a 70% sub-mask seems to be plausible and fairly robust. However, some attention is required if the tumor resides in the insular cortex as this seem to have a general higher level of FET uptake.

5.2.2 Tumor

The variance associated with TBR_{95} was assessed in two ways. The radioactive decay is Poisson distributed and the tumor is consequently a mixture of different Poisson distributions [20]. The gamma distribution is closely related to the Poisson distribution, hence modelling TBR as gamma distributed was plausible in theory, but turned out to be infeasible in practice. The reason is most likely due to the many shoulders on the histogram, as was noticed in figure 4.3. The tumors might have several separate foci, or different hot spots with a high uptake within the same focus, as was seen in both the pre-treatment and in-treatment scan in figure 3.6. This indicate that the tumor is a mixture of many different distributions.

Another approach to investigate the variance was based on the extreme value index and the results were presented in table 4.2. The estimated variance and the empirical TBR_{95} was used to establish a response criterion for each patient. The variance estimate is based on the assumption that the samples are independently distributed, but the voxels in a PET image will to some degree be correlated. The attempt to correct for this using 1000 randomly sub-sampled voxels was not successful. The EVI moment estimator requires a large number of observations, as explained in section 2.4.2.1. EVI is estimated from the observations above TBR_{95} as shown in equation 2.15, which implies that only 5% of the total number of voxels are included. So when 1000 voxels were sub-sampled, only 50 voxels were included in the estimation of EVI, which turned out to be

insufficient.

The degree of correlation between pixels in a PET image was addressed by investigating a sub-region within the brain as illustrated in appendix A.1.3. The effective number of pixels in that region was found to be approximately $N_{eff}/N = 1/600$. This indicates a strong correlation between the pixels that has to be accounted for when estimating the variance. In this thesis is was assumed that the horizontal correlation between pixels in the brain is representative for the overall correlation between voxels in a tumor. This might be a rough approximation, but it serves the purpose to give an indication of the level of correlation. A more accurate estimate would only include a sub-region within the tumor and consider the correlation between slices as well. The tumor is suspected to be more heterogeneous than the healthy tissue, which will probably lead to less correlated pixels and in consequence a lower $N_{eff}/N = 1/600$.

Under the assumption that $N_{eff}/N = 1/600$, the estimated standard deviation on the TBR_{95} was found to be in the order of 0.25. This lead to an average required change of -24.13%, which is somewhat higher than what Piroth et al. have previously shown for TBR_{max}. They have empirically shown that a change in TBR_{max} of -10% was associated with a positive clinical response. 4 out of 16 patients was shown to have a significant reduction in TBR_{95}, however, there is no guarantee that TBR_{95} is related to the actual clinical response and this has to be verified, in order to manifest its clinical potential. Most of these patients were diagnosed during January and February 2012 and no data on survival or progression were available at the deadline of this thesis, hence the decisive conclusion is yet to be made.

Patient number 12 was excluded from the average estimation, since the in-treatment tumor only consisted of 132 voxels as was shown in table 4.2. This is far to few observations for the moment estimator to produce a meaningful EVI.

In summary, the TBR variance is possible to estimate using EVI and moment estimation, which can lead to individual response criteria. The fact that the distribution of TBR might be a mixture of several distributions, could have an impact on the estimation of the extreme value index, and subsequently the TBR variance. However, the method implemented here seems to be a reasonable first order approximation.

5.3 Response characterization

Extraction of image derived parameters was explained section 3.2.2. The following section discuss the response characterization that was presented in section 4.2.

Figure 4.6 showed the change in raw SUV and a distinct elevation from pre-treatment to in-treatment was noticed. Higher SUV values in the tumor could indicate an increase in tumor aggressiveness, but since the background showed an equal elevation, the higher SUV are rather a result of a general increase in FET-uptake. The higher level could be explained by a longer time from injection of FET to the beginning of scan, but actually the opposite was the case as seen in table 3.2, where median waiting time went from 21.1 minutes to 20.6 minutes. The higher uptake might also be a result of radiation. Brandsma et. al mentioned both vasodilation and disruption of the blood-brain-barrier as two common acute side-effects of radiotherapy. Both events lead to an increased intracranial blood volume and potentially higher SUV values [57]. The elevated level of SUV presented here justifies the use of TBR as the primary choice of clinical parameter.

The change in TBR was more evenly distributed around zero percent, when compared to raw SUV measurements, as shown in figure 4.7a. The change in TBR has proved to reflect the response to therapy [6, 53] and the distribution of TBR around zero indicate that some patients are responding and some are not. The spreading on ΔTBR_{mean} is lower compared to the maximum and sub-maximal ratios. This indicate that radiotherapy has the greatest impact on the most active areas of the tumor. A reduction in ΔTBR_{mean} is either due to a lower overall level of TBR or a decrease in the most active areas. The latter will result in a more homogeneous tumor and even though modest, a slightly higher AUC-IVH was noticed in the in-treatment scan (median: 2.73%, range: -9.34% - 23.3%).

Traditionally, TBR_{max} has been used as the best indicator of response to therapy. It was argued that TBR_{95} has an equal potential and a lower variance. The exact difference in variance has not been investigated, though, since the uncertainty with the most extreme value is rather difficult to quantify. The correlation between the two parameters was indisputable as shown in figure 4.9.

The correlation between ΔTBR_{95} and four important parameters was investigated, as an attempt to identify predictive parameters. High pre-treatment TBR_{95} and TBR_{mean} were significantly correlated with large change in TBR_{95}. This could again indicate that the most active areas are those that are most sensitive to chemoradiotherapy. No significant correlation was found for AUC-

IVH or solidity. However, there was a tendency for tumors with high solidity to experience a larger change in TBR_{95}. The correlations are based on the result from 16 patients, and will require a larger cohort of patients in order to draw any general conclusion.

One of the major goals with this thesis was to illustrate the individual response to therapy. Traditionally this is done by measures that are easy to extract, i.e. volume and TBR_{max} or by visual inspection of the follow up MRI and/or FET scan. However, this demands quite a few resources, and will be prone to both inter- and intra-observer variability. The IVH and the estimate of solidity are two suggestions on how to reduce the complex information in a 3D image, to measures that are easy to interpret. The parameters have earlier proved applicable in other cancer-types, such as head-and-neck, cervix and non-small cell lung cancer, but need to be clinical verified in the case of brain tumors [8, 9].

As the response maps showed in figure 4.5a and in section A.3 there are often distinct areas of the tumor that respond and others that do not. It would be desirable to predict the regions that do not respond, so that treatment alternatives can be considered before treatment. As mentioned in section 2.3.2, regions that are hypoxic are generally more resistant to radiotherapy, hence examinations of these areas might be important. This can be done either by MR perfusion imaging, which does not increase the workload particularly, since anatomical MRI are already routinely performed. Another approach would be to use a PET tracer that is sensitive to oxygen deprived regions, such as fluorine-18-fluoromisonidazol (FMISO) [58]. Another interesting issue is the repopulation of cells during and after radiotherapy. The poor prognosis for patient with GBM, might indicate that the fractionated radiotherapy is not the optimal strategy for these patients. The standard 2 Gy fractionated treatment might not be sufficient, if the surving fraction of cells is different from what was explained in section 2.3.2 or if the repopulation of tumor cells are more pronounced than normal tissue cells.

5.4 Spatial changes

The average distance from the border voxels of the FET2 volume to the borders of CH1 was found to be 3.29 mm (CI95%: 2.11-4.47mm). This as a modest change, which corresponds to 4-5 voxels, however, large displacements of up to 3.5 cm was noticed as well. This is an indication, that some tumors might spread widely and some remain stable. This was also apparent from the cumulated curve in figure 4.11, which showed that 13 of the tumors would be fully covered by a margin around 1 cm. Figure 4.12 showed that a margin of approximately 5

mm added to the pre-treatment convex hull on average would cover 95% of the FET positive volume at the time of the second scan. These findings may give an indication of the spatial change in FET-uptake during treatment. One has to bear in mind, that these scans are performed after approximately 20 fractions and the AD after all 30 fractions might be even larger.

In a study by Piroth et al., it was investigated if increasing the dose to the BTV to 72 Gy would improve the overall survival. However, they discovered that the sub-volume boosting did not lead to any survival benefit. The spatial change quantified in this thesis, might explain why they did not succeed. If the FET positive volume are changing radically during treatment, the effect of sub-volume boosting to BTV determined at the pre-treatment scan might not be fully exploited, since the tumor "escapes" the boosted area. Sub-volume boosting based on the pre-treatment BTV alone is thus not a treatment strategy to follow. An alternative strategy is to predict the patterns in which the tumor grow and increase the dose in these areas as well. Krishnan et. al found that the tracts of water diffusion were correlated with the location of tumor progression, which indicate that diffusion tensor imaging (DTI) can be used to predict the escape routes of brain tumors [59]. Boosting the dose to the most active areas as shown in the FET-PET images as well as along the most pronounced diffusion tracts might then lead to a better local tumor control.

Furthermore, table 4.5 showed that the tumor in 5 out 16 patients outgrew the 95% isodose, which indicate that the standard treatment protocol with 2 Gy in 30 fractions is not ideal for controlling the tumor. If the 2 Gy fractionation is to be used, it would be advisable the adapt the dose-plan during the treatment, even though this would require additional scans to be performed. In every PET/CT examination, a considerable amount of dose is deposited in the patient and this sets an upper limit for the number of possible examinations. Performing the additional examinations using a combined PET/MR scanner would be highly beneficial, since this eliminates the dose delivered from the CT scan, while at the same time providing a higher level of anatomical details and the possibility to perform more advanced examinations, such as perfusion MRI.

The correlations between AD and the number of fractions, as well as the number of days, before FET2 were investigated. No significant correlations were found, which again indicate that the response is very patient specific and thus require individual assessment.

The accuracy of the registration of the images was not estimated, which is of course necessary to fully interpret the margin estimates. This could be done by measuring the Euclidean distance between some anatomically defined landmarks.

5.5 Perspectives

Several treatment strategies have been investigated in order to prolong survival of patients with GBM as was reviewed by [3]. The data presented in section 4.3 might be an explanation to the limited success in some of the approaches. The 60 Gy with 2 Gy per fraction in combination with TMZ, is the standard treatment protocol offered to patients with GBM, but the median OS of 15 months suggest that alternatives should be explored. Sub-volume boosting to the pre-treatment BTV does not seem to be approach to follow, since a pronounced spatial change is observed during the treatment. Some hypo-fractionated trials, i.e. treatment with a higher dose delivered in fewer fractions, have shown significant improvement in both PFS and OS. Baumert et. al showed an increase in OS to 20 months using a stereotactic boost, i.e. a high fraction usually 10-15 Gy given in a single fraction, after conventional therapy [60].

If it turns out that there is a correlation between the response after 40 Gy and the overall survival, the intermediate FET scan performed in this thesis could be used to identify patients that do not respond to the conventional radiotherapy and thus could have a potential benefit of an altered treatment. In case ΔTBR_{95} shows a correlation with clinical outcome, the methods used here could be used to identify those patients that have no benefit of the standard treatment, but who could potentially merit from a stereotactive boost.

Chang et. al has shown that there is no significant correlation between MRI-defined CTV and tumor progression [61], while Lee et. al, on the contrary, showed a tendency for recurrence in areas that were positive on MET-PET scans [62]. These findings suggest that it might be possible to define the CTV from the FET positive area, instead of using the traditional 2 cm margin to the GTV. Combined with the results presented here, a 5 mm margin added to the convex hull of the pre-treatment FET scan could be a suggestion to an alternative CTV. Reducing the margins will reduce the irradiated volume in the brain and will potentially reduce side-effects. However, the reduction of margin should not compromise the overall tumor control.

The estimation of B, using a 70% sub-mask in the contralateral hemisphere proved to be pretty robust. However, method of background estimation differs between treatment centres [7, 53, 63] and if results are to be compared across centres, this suggest that a standard method is established.

5.6 Future work

The result presented in this thesis are by no means exhaustive, but rather scratch the tip of an iceberg. The results need to be verified against clinical outcome, which can be done as the patients progress. The establishment of individual response criteria is promising, but it will most likely require that the correlation between voxels in a tumor, is quantified more precisely. Estimation of the EVI can be further refined as well. Beirlant et. al suggest the use exponential regression models as a more accurate measure of the EVI [64].

The correlation between ΔTBR_{95} and the level of oxygen, as well as the correlation of DTI and spatial tumor progression, are two investigations that would be extremely interesting to do. If both radio-resistance and local tumor escape routes can be predicted from pre-treatment examinations, the definition of a more sophisticated dose plan would be possible. This could possibly lead to better tumor control and longer overall survival.

The correlation of ΔTBR_{95} with various image-derived parameters proved to be significant. Eikenberry et. al presented a mathematical model growth, migration and treatment used for simulation tumor progression and treatment [65]. The development of a similar response model, that incorporates various significant response parameters, would be a valuable tool for physicians. Identification of response predicting parameters, and the correlation between different parameter, could possibly be used to establish such a model that would aid in dealing with patient prognosis.

Chapter 6

Conclusion

16 patients were diagnosed with primary glioblastoma multiforme during the first half of 2012. They received a standard therapy with surgical tumor reduction, fractionated radiation therapy as well as concurrent and subsequent chemotherapy. The patients were scanned with FET-PET both prior to, and during their treatment. The aim of this project was to visualize and quantify the intermediate response to therapy based on image-derived parameters from these two FET scans.

The definition of background uptake was shown not to be sensitive to the contour delineated by the physician. Determination of B using sub-mask of 70% or below was shown to produce a significant difference between areas above the insular cortex and within the insular cotex ($p<0.01$). Changes in tumor volume as a result of using different sub-masks was shown to shown to be most pronounced when increasing the level, i.e. for sub-masks of 80% and 90%. The 70% sub-masks seems like a feasible compromise between excluding CSF and favoring high-uptake regions.

An individual response criterion, based on TBR_{95} and moment estimation of the extreme value index, was establish under the assumption that the ratio of effective uncorrelated voxels and total number of voxels $N_{eff}/N = 1/600$. The method indicated that 4 out of 16 patients had a significant reduction in TBR_{95} at a 5% level of significance. The average required change in TBR_{95} was found to be -24% which is higher than the required, and clinically confirmed, change in TBR_{max}. The difference can both be due to an erroneous estimate of $N_{eff}/N0$ as well as a result of comparing two different parameters. This have to be investigated further.

Several image-derived parameters were extracted and compared to the percentage change in TBR_{95}. The strongest correlations was seen for pre-treatment TBR_{95} and TBR_{mean}, respectively. However, clinical response assessment is required in order to determine if TBR_{95} can be used as a clinical parameter and no decisive conclusion can be made about the predictive power of the various image-derived parameters.

The spatial change of the tumor during chemoradiotherapy, was quantified by an average distance from the convex hull of the pre-treatment scan to boundary of the FET positive volume in the in-treatment scan. An AD of 3.29 mm and a 95% confidence interval of 2.11-4.47 mm were noticed. A 5 mm margin added to the pre-treatment convex hull was found to include on average 95% of the FET positive volume of the in-treatment scan. These findings might explain way several trials, that boost the dose based on FET-derived BTV, have not succeeded in increasing overall survival.

Based on the analysis used in this thesis, 12 patients that were identified as non-responding to the standard chemoradiotherapy and who would potentially benefit from an alteration in the remaining third of the treatment.

Appendix A

Appendix

A.1 Parameter uncertainties

A.1.1 Background

Patient	AI	II	AI60	II60	AI70	II70	AI80	II80	AI90	II90
a	1.1281	1.1582	1.1357	1.1594	1.1485	1.172	1.1941	1.2119	1.2899	1.2935
b	0.677	0.6731	0.6959	0.6852	0.7108	0.7061	0.7441	0.7525	0.8086	0.8179
c	0.7005	0.7521	0.7069	0.7535	0.7258	0.7623	0.7687	0.8006	0.8336	0.8766
d	0.6735	0.6749	0.6884	0.6806	0.7135	0.6947	0.769	0.7354	0.8409	0.798
e	0.7853	0.8202	0.7955	0.837	0.8247	0.8734	0.8884	0.9411	0.9772	1.0353
f	0.6253	0.6628	0.6292	0.6648	0.6391	0.6755	0.6636	0.7215	0.7083	0.8043
g	0.8046	0.8464	0.8055	0.8464	0.8152	0.853	0.8545	0.8709	0.9189	0.9223
h	0.7358	0.7258	0.7378	0.7274	0.751	0.7387	0.7831	0.7873	0.8472	0.8461
i	0.5872	0.5877	0.5924	0.5903	0.6053	0.5954	0.6394	0.6178	0.6939	0.6615
j	0.8982	0.9447	0.9146	0.9457	0.935	0.9579	0.9827	1.0083	1.0589	1.069
k	0.7257	0.7374	0.7354	0.7388	0.7506	0.7502	0.7888	0.7826	0.8567	0.8468
l	0.9675	0.9504	0.9785	0.9793	1.0082	1.0245	1.0724	1.0795	1.1704	1.1602
m	0.8708	0.9374	0.9085	0.938	0.9369	0.9454	0.9893	0.9701	1.0805	1.0401
n	1.0551	1.0624	1.0651	1.0664	1.0785	1.0852	1.1045	1.126	1.1672	1.2139
o	1.1177	1.1362	1.1305	1.147	1.1679	1.1712	1.2565	1.2255	1.4136	1.3173
p	0.9555	0.9804	0.9731	0.9844	1.0041	0.9945	1.0739	1.0442	1.1681	1.1296
q	0.8233	0.8411	0.8287	0.8419	0.8429	0.8473	0.8891	0.866	0.967	0.9193
r	0.1628	0.1672	0.1703	0.1764	0.1797	0.1911	0.1965	0.2125	0.2158	0.2354
s	0.7386	0.7815	0.7769	0.802	0.8195	0.8431	0.8765	0.9174	0.9327	1.0012
t	0.8503	0.8396	0.8666	0.8585	0.8927	0.882	0.945	0.9298	1.0255	1.0117

Table A.1: Background measurements above insula (AI) and in insula (II) as reported by a physician, using submasks of 60%, 70%, 78% and 90%, respectively.

	Above Insula		In Insula	
Patient	Reported	Average	Reported	Average
a	1.1485	1.1562	1.172	1.1741
b	0.7108	0.7126	0.7061	0.7049
c	0.7258	0.7266	0.7623	0.7643
d	0.7135	0.7122	0.6947	0.697
e	0.8247	0.8222	0.8734	0.8675
f	0.6391	0.6406	0.6755	0.6765
g	0.8152	0.8123	0.853	0.8501
h	0.751	0.7489	0.7387	0.7375
i	0.6053	0.6073	0.5954	0.5939
j	0.935	0.9342	0.9579	0.9696
k	0.7506	0.7529	0.7502	0.7503
l	1.0082	1.0037	1.0245	1.0251
m	0.9369	0.9364	0.9454	0.9506
n	1.0785	1.0771	1.0852	1.0934
o	1.1679	1.1682	1.1712	1.1765
p	1.0041	1.0033	0.9945	0.9935
q	0.8429	0.8425	0.8473	0.8504
r	0.1797	0.1814	0.1911	0.1887
s	0.8195	0.8185	0.8431	0.8526
t	0.8927	0.9013	0.882	0.8896

Table A.2: Estimate of the sensitivity, both above insula (AI) and in insula (II). Average is estimated by moving hand-delineated submask 4 pixels (3.3mm) up/down and left/right. Reported activity is determined using a 70% submask, as this is done routinely in the clinic.

A.1.2 Probability density of extreme observations

The Generalized Pareto Distribution (GPD) is given by:

$$G_{\xi,\upsilon,\varepsilon}(x) = \begin{cases} 1 - \left(1 + \xi \frac{x-\upsilon}{\varepsilon}\right)^{-1/\xi} & \text{for} \quad \xi \neq 0, \\ 1 - e^{-\frac{x-\upsilon}{\varepsilon}} & \text{for} \quad \xi < 0 \end{cases} , \tag{A.1}$$

where ξ is a shape parameter, υ is location parameter and ε is a scale parameter. The GPD for rare observations may be written as $G(x_{1-p}) = 1-p$, where p is the exceedance probability (close to zero). If the shape of the tail is characterized by the EVI, the GPD may be written as

$$G(x_{1-p}) = 1 - \left(1 + \hat{\gamma}\frac{x-\upsilon}{\varepsilon}\right)^{-1/\hat{\gamma}} , \tag{A.2}$$

where $\hat{\gamma} \neq 0$ is the estimate of EVI. The x_{1-p} fractile is then given by

$$1 - p = 1 - \left(1 + \hat{\gamma}\frac{x-\upsilon}{\varepsilon}\right)^{-1/\hat{\gamma}} \tag{A.3}$$

$$p = \left(1 + \hat{\gamma}\frac{x-\upsilon}{\varepsilon}\right)^{-1/\hat{\gamma}} \tag{A.4}$$

$$p^{-\hat{\gamma}} = \left(1 + \hat{\gamma}\frac{x-\upsilon}{\varepsilon}\right) \tag{A.5}$$

$$p^{-\hat{\gamma}} - 1 = \hat{\gamma}\frac{x-\upsilon}{\varepsilon} \tag{A.6}$$

$$x_{1-p} = \upsilon + \frac{\varepsilon}{\hat{\gamma}}\left(p^{-\hat{\gamma}-1}\right) . \tag{A.7}$$

If $p = 0.05$ and $p = 0.01$ the fractiles are given by

$$x_{0.95} = \upsilon + \frac{\varepsilon}{\hat{\gamma}}\left(0.05^{-\hat{\gamma}-1}\right) \tag{A.8}$$

$$x_{0.99} = \upsilon + \frac{\varepsilon}{\hat{\gamma}}\left(0.01^{-\hat{\gamma}-1}\right) , \tag{A.9}$$

respectively. Subtracting A.8 from A.9 yields:

$$\hat{\varepsilon} = \hat{\gamma}\left(\frac{x_{0.99} - x_{0.95}}{0.01^{-\hat{\gamma}} - 0.05^{-\hat{\gamma}}}\right) , \tag{A.10}$$

as an estimate of the scale in tail of the distribution. Rearranging A.7 gives an estimate of the location:

$$\hat{\upsilon} = x_{1-p} - \frac{\varepsilon}{\hat{\gamma}}\left(p^{-\hat{\gamma}-1}\right) . \tag{A.11}$$

The probability density function is given by:

$$g(x) = \frac{1}{\varepsilon}\left(1 + \gamma\frac{x-\upsilon}{\varepsilon}\right)^{-\frac{1+\gamma}{\gamma}} . \tag{A.12}$$

By rearranging and inserting the approximated parameters, the density around x_{1-p} may then be written as

$$g(x_{1-p}) \simeq \frac{1}{\hat{\varepsilon}}p^{1+\hat{\gamma}} \tag{A.13}$$

A.1.3 Correcting for correlated pixels

A sub-region within the brain was used to determine the correlation between pixels in a PET image. The region contained mostly healthy tissue, but a small amount of tumor was included as well. See figure A.1a. The sum of squared differences (SSD) for a shifted version of the region was determined and plotted against the lag as shown in figure A.1b. The brain is considered more or less isotropic, hence only a horizontally shift was used. The correlation as a function of lag was calculated as $1 - \frac{SSD}{\hat{\sigma}}$, where σ is the variance in the region, as shown in figure A.1c. An exponential decrease in correlation was noted, and the corresponding correlation function was fitted by a Gaussian function using the statistical software SPSS. The estimated function was $\rho(i,j) = e^{-0.00437\cdot\sqrt{i^2+j^2}^2}$ and is visualized in figure A.1d. By using the estimated correlation function, the correlation between all pixels in the image were estimated. The sum of the correlation between pixels can in a compact notation be written as

$$\sum \rho(i,j) = \begin{pmatrix} \sum_0 & \sum_1 & \cdots & \sum_{m-1} \\ \sum_1 & \sum_0 & \cdots & \sum_{m-2} \\ \vdots & \vdots & \ddots & \vdots \\ \sum_{m-1} & \sum_{m-2} & \cdots & \sum_0 \end{pmatrix} , \tag{A.14}$$

where m denotes the number pixels in the second dimension of the region. The element sum, S_μ, of matrix $\sum_\mu$ is given by:

$$S_\mu = n\rho(0,\mu) + 2\sum_{\nu=1}^{n-1}(n-\nu)\rho(\nu,\mu) , \tag{A.15}$$

where n denotes the number of pixels in the first dimension of the region. The element sum $\sum \rho(i,j)$ is subsequently calculated as

$$S = \sum \rho(i,j) = mS_0 + 2\sum_{\mu=1}^{m-1}(m-\mu)S_\mu . \tag{A.16}$$

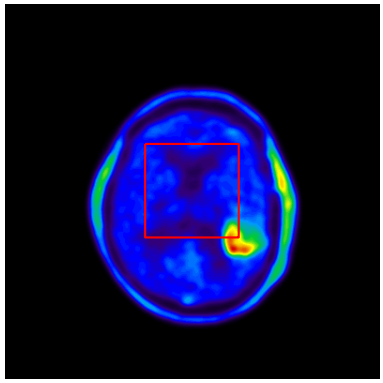

(a) Brain showin region where correlation is estimated. The region contains mostly healthy tissu, but a small part of the tumor is included as well.

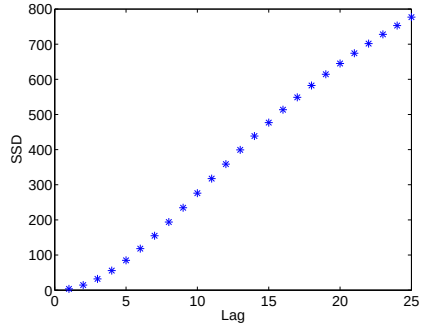

(b) Sum of squared difference as a function of lag.

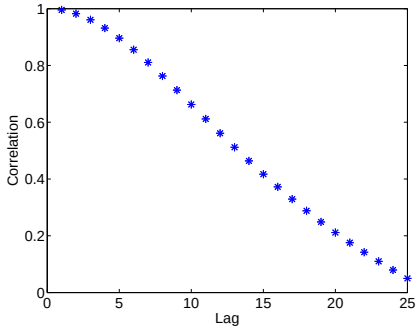

(c) Correlation as a function of lag.

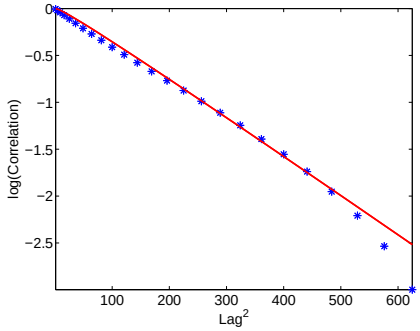

(d) Estimated correlation function.

Figure A.1

The extracted region was 101×101 pixels, giving a total number of $N = 10201$ pixels. The estimated element sum of the correlation was $6.2113 \cdot 10^6$, and the effective number of pixels in the image was calculated as $N_{eff} = N^2/S$.

$$N_{eff} = \frac{10201^2}{6.2113} = 16.75 \tag{A.17}$$

This gives a ratio of pixels to effective pixels of 10201/16.75 or approximately 600:1.

A.2 Scan parameters

A.2.1 Uptake

Patient	$\mathbf{SUV}_{max}$	$\mathbf{SUV}_{mean}$	$\mathbf{SUV}_{peak_{99}}$	$\mathbf{SUV}_{99.5}$
1	2.225	1.401	1.9226	1.8069
2	2.5044	1.3722	1.9836	1.7689
3	2.3371	1.3169	1.9748	1.8251
4	2.4977	1.5851	2.1142	1.9594
5	2.3821	1.4614	2.1298	2.0025
6	2.1012	1.3402	1.8743	1.7944
7	3.0617	1.6662	2.7096	2.5391
8	1.7021	1.263	1.5406	1.4772
9	2.7521	1.5297	2.4396	2.2435
10	2.4268	1.4751	2.2127	2.096
11	2.5853	1.7699	2.2913	2.1663
12	2.0856	1.6609	1.9662	1.8845
13	3.8677	2.0402	3.3074	3.0401
14	4.0887	2.3709	3.6696	3.4395
15	3.2619	1.985	2.7284	2.5264
16	2.5748	1.7386	2.3007	2.1918

Table A.3: Patient data extracted from pre-treatment images.

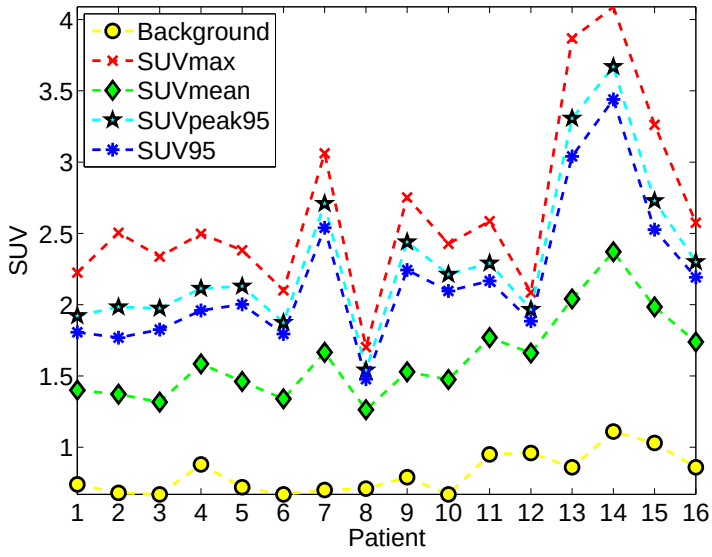

Figure A.2: SUV pre-treatment.

Patient	$\mathbf{SUV}_{max}$	$\mathbf{SUV}_{mean}$	$\mathbf{SUV}_{peak_{99}}$	$\mathbf{SUV}_{99.5}$
1	2.6258	1.7879	2.3811	2.28
2	2.7611	1.5608	2.3001	2.1186
3	3.2066	1.7415	2.7709	2.5605
4	3.3838	2.1134	2.9534	2.709
5	3.0947	1.8184	2.5387	2.2644
6	2.673	2.0307	2.4908	2.4148
7	2.2697	1.4335	2.0457	1.963
8	1.8333	1.2421	1.633	1.5535
9	3.2815	1.7079	2.8303	2.5691
10	2.1409	1.5416	2.012	1.9463
11	2.7646	1.8026	2.406	2.262
12	2.2033	1.9513	2.18	2.1482
13	4.1235	2.4437	3.5972	3.3591
14	3.0025	2.1509	2.7632	2.6517
15	3.3116	1.8255	2.7667	2.531
16	2.9111	2.0118	2.7143	2.6082

Table A.4: Patient data extracted from in-treatment images.

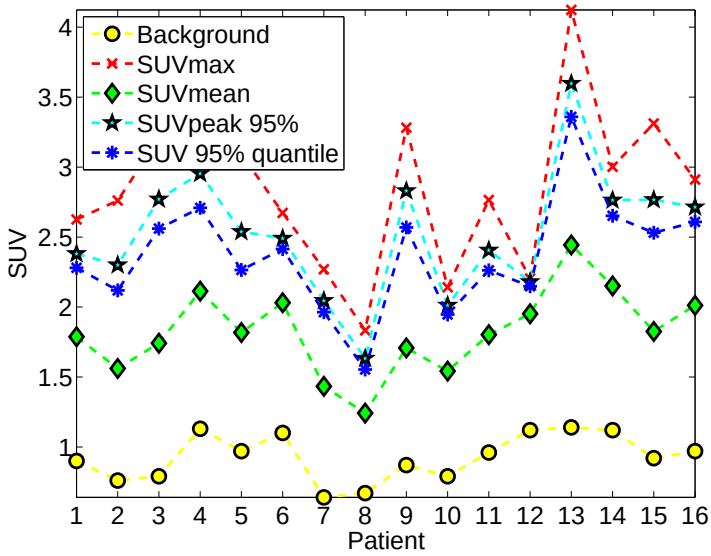

Figure A.3: SUV in-treatment.

Patient	$\mathbf{SUV}_{max}$	$\mathbf{SUV}_{mean}$	$\mathbf{SUV}_{peak_{99}}$	$\mathbf{SUV}_{99.5}$
1	18.014	27.613	23.844	26.183
2	10.25	13.745	15.953	19.771
3	37.205	32.242	40.313	40.291
4	35.473	33.328	39.695	38.254
5	29.914	24.426	19.2	13.075
6	27.214	51.522	32.893	34.576
7	-25.869	-13.965	-24.503	-22.688
8	7.7054	-1.6589	5.9974	5.1647
9	19.237	11.648	16.012	14.513
10	-11.781	4.5098	-9.0681	-7.1433
11	6.9377	1.8457	5.0058	4.4166
12	5.6479	17.485	10.875	13.989
13	6.6143	19.776	8.7624	10.495
14	-26.566	-9.2794	-24.7	-22.904
15	1.5239	-8.0311	1.4068	0.18429
16	13.058	15.714	17.976	18.995

Table A.5: Change in patient data in percent. Changes are with respect to pre-treatment scan, i.e. negative values indicate a reduction from first to second scan.

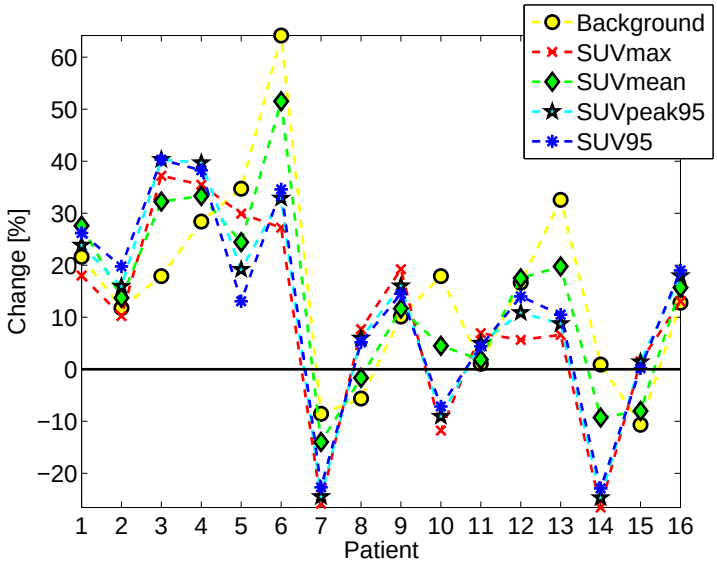

Figure A.4: Response plot.

Patient	$\mathbf{T}_{max}/\mathbf{B}$	$\mathbf{T}_{mean}/\mathbf{B}$	$\mathbf{T}_{peak_{99}}/\mathbf{B}$	$\mathbf{T}_{99.5}/\mathbf{B}$
1	3.0067	1.8933	2.5982	2.4418
2	3.6829	2.0179	2.9171	2.6013
3	3.4882	1.9656	2.9474	2.7241
4	2.8384	1.8013	2.4025	2.2266
5	3.3085	2.0297	2.958	2.7813
6	3.1361	2.0003	2.7975	2.6782
7	4.3739	2.3803	3.8708	3.6273
8	2.3974	1.7789	2.1699	2.0805
9	3.4837	1.9364	3.0882	2.8399
10	3.6221	2.2016	3.3025	3.1283
11	2.7213	1.863	2.4119	2.2804
12	2.1725	1.7301	2.0481	1.9631
13	4.4973	2.3723	3.8458	3.535
14	3.6835	2.1359	3.3059	3.0987
15	3.1669	1.9271	2.6489	2.4528
16	2.994	2.0216	2.6752	2.5486

Table A.6: Patient data extracted from pre-treatment images.

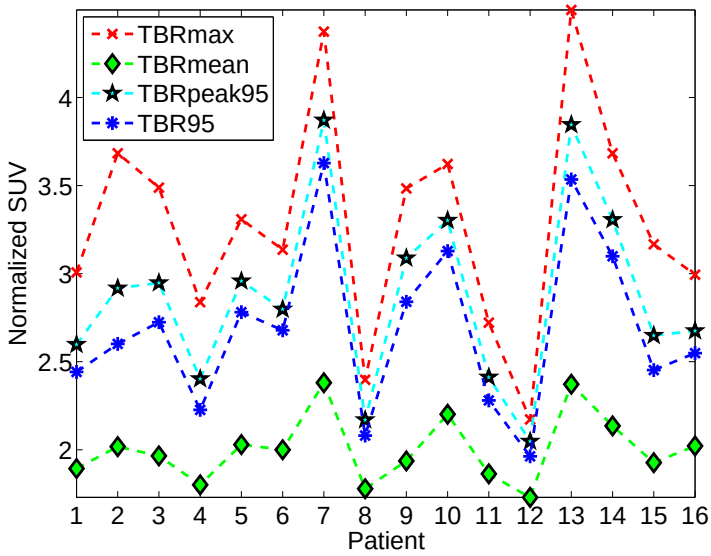

Figure A.5: TBR pre-treatment.

Patient	$\mathbf{T}_{max}/\mathbf{B}$	$\mathbf{T}_{mean}/\mathbf{B}$	$\mathbf{T}_{peak_{99}}/\mathbf{B}$	$\mathbf{T}_{99.5}/\mathbf{B}$
1	2.9175	1.9865	2.6456	2.5334
2	3.633	2.0537	3.0264	2.7877
3	4.059	2.2045	3.5074	3.2411
4	2.9945	1.8703	2.6137	2.3974
5	3.1904	1.8746	2.6172	2.3344
6	2.43	1.8461	2.2644	2.1953
7	3.5464	2.2398	3.1964	3.0672
8	2.7363	1.8539	2.4374	2.3186
9	3.7719	1.9631	3.2532	2.953
10	2.71	1.9514	2.5469	2.4636
11	2.8798	1.8777	2.5062	2.3563
12	1.9673	1.7423	1.9464	1.918
13	3.6171	2.1436	3.1554	2.9466
14	2.6808	1.9204	2.4672	2.3676
15	3.5995	1.9843	3.0073	2.7511
16	3.0011	2.074	2.7982	2.6888

Table A.7: Patient data extracted from in-treatment images.

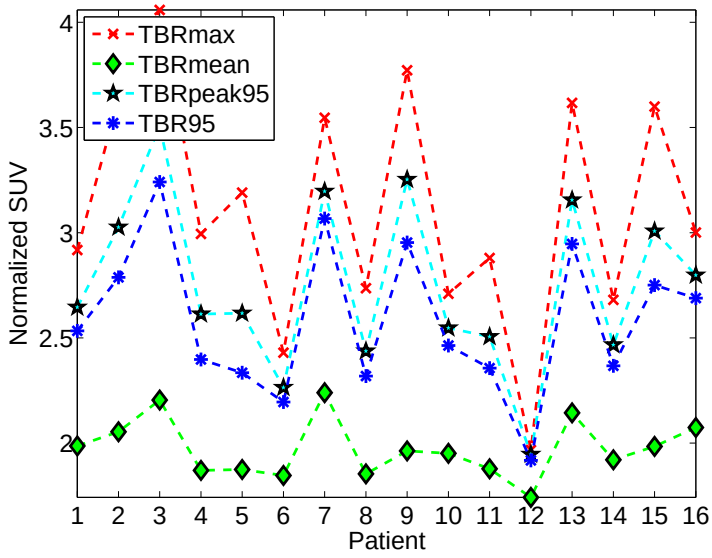

Figure A.6: TBR in-treatment.

Patient	$\mathbf{T}_{max}/\mathbf{B}$	$\mathbf{T}_{mean}/\mathbf{B}$	$\mathbf{T}_{peak_{99}}/\mathbf{B}$	$\mathbf{T}_{99.5}/\mathbf{B}$
1	-2.9659	4.9265	1.8271	3.7508
2	-1.3549	1.7722	3.7475	7.1634
3	16.364	12.154	18.999	18.981
4	5.5014	3.8309	8.7893	7.667
5	-3.5692	-7.6423	-11.522	-16.068
6	-22.515	-7.7095	-19.056	-18.031
7	-18.92	-5.8992	-17.425	-15.44
8	14.136	4.2122	12.326	11.443
9	8.2726	1.3819	5.344	3.9829
10	-25.181	-11.365	-22.881	-21.248
11	5.8237	0.78479	3.912	3.3289
12	-9.4447	0.70113	-4.964	-2.2952
13	-19.572	-9.6424	-17.951	-16.644
14	-27.222	-10.089	-25.372	-23.593
15	13.663	2.9651	13.532	12.163
16	0.23699	2.5918	4.5976	5.501

Table A.8: Change in patient data in percent. Changes are with respect to pre-treatment scan, i.e. negative values indicate a reduction from first to second scan.

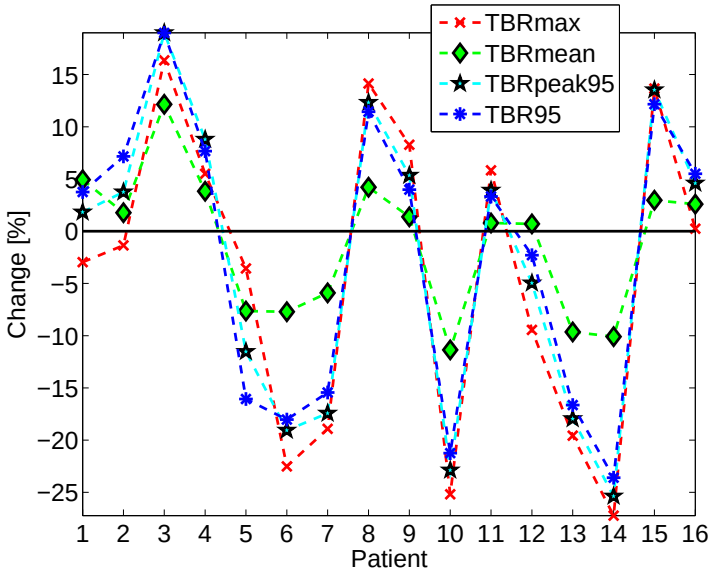

Figure A.7: Response plot of TBR in percent.

A.2.2 Shape

Patient	FET vol [cm^3]	ConvHull vol [cm^3]	Foci	Solidity	AUC IVH
1	26.63	50.377	1	0.52861	62.84
2	35.814	40.444	1	0.88552	54.747
3	21.456	35.792	3	0.59947	56.283
4	35.985	112.08	4	0.32107	63.326
5	56.522	115.08	1	0.49117	61.237
6	65.923	127.93	2	0.51529	63.645
7	54.053	57.891	1	0.93371	54.378
8	16.603	54.262	7	0.30598	73.97
9	7.5123	8.9555	3	0.83885	55.527
10	23.833	25.674	1	0.92828	60.673
11	48.729	101.62	1	0.47954	68.274
12	3.577	7.0167	1	0.50979	79.352
13	29.243	31.694	1	0.92269	52.724
14	33.977	44.889	1	0.75691	57.912
15	37.789	63.063	1	0.59922	60.752
16	30.818	35.611	1	0.8654	67.348

Table A.9: Patient data extracted from pre-treatment images.

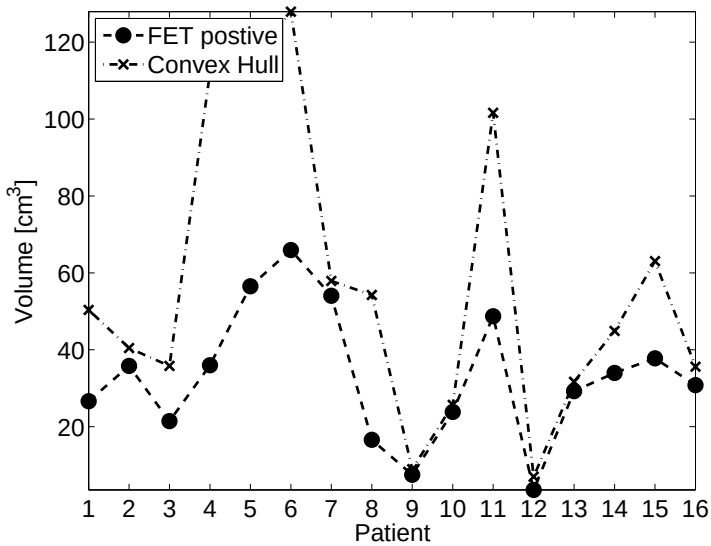

Figure A.8: Volume estimates from pre-treatment scans.

Patient	FET vol [cm^3]	ConvHull vol [cm^3]	Foci	Solidity	AUC IVH
1	44.354	60.628	1	0.73156	67.907
2	33.394	47.769	4	0.69906	56.46
3	48.611	54.276	1	0.89562	54.272
4	17.352	30.171	1	0.57511	62.332
5	47.594	127.03	2	0.37467	58.666
6	35.171	88.725	1	0.39641	75.715
7	54.294	62.81	1	0.86442	63.028
8	41.429	68.342	1	0.60621	67.578
9	7.2874	8.8978	1	0.81902	52.04
10	15.974	16.615	1	0.96142	71.785
11	51.802	112.84	1	0.45907	65.062
12	0.26275	0.26872	1	0.97778	88.189
13	32.776	36.477	1	0.89855	59.174
14	33.493	53.474	1	0.62634	71.422
15	50.624	67.605	1	0.74881	55.079
16	40.13	47.819	1	0.8392	68.915

Table A.10: Patient data extracted from in-treatment images.

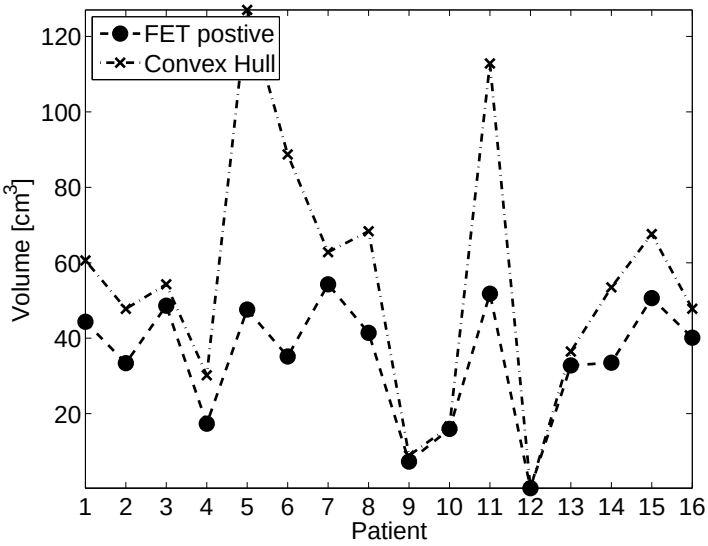

Figure A.9: Volume estimates from in-treatment scans.

Patient	FET vol [cm^3]	ConvHull vol [cm^3]	Foci	Solidity [%]	AUC IVH [%]
1	66.557	20.349	0	38.395	8.0625
2	-6.7586	18.112	3	-21.057	3.128
3	126.56	51.643	-2	49.404	-3.5725
4	-51.781	-73.081	-3	79.126	-1.5699
5	-15.795	10.389	1	-23.72	-4.1995
6	-46.648	-30.648	-1	-23.071	18.964
7	0.44559	8.4964	0	-7.4203	15.907
8	149.53	25.946	-6	98.121	-8.6409
9	-2.9942	-0.64459	-2	-2.3648	-6.2791
10	-32.974	-35.285	0	3.57	18.315
11	6.3072	11.048	0	-4.2693	-4.7043
12	-92.654	-96.17	0	91.801	11.137
13	12.082	15.092	0	-2.6154	12.235
14	-1.4236	19.126	0	-17.25	23.329
15	33.965	7.2031	0	24.964	-9.3371
16	30.216	34.282	0	-3.028	2.3265

Table A.11: Patient data extracted from in-treatment images.

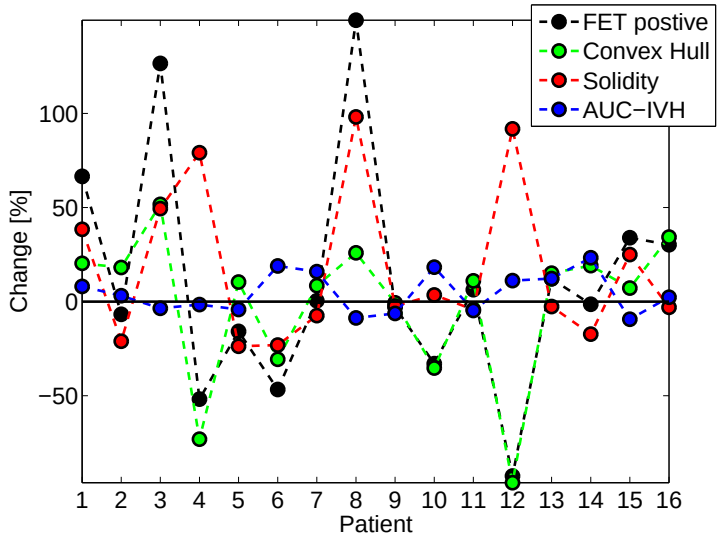

Figure A.10: Change in volume estimates, relative to the pre-treatment scan.

A.3 Patient visualization

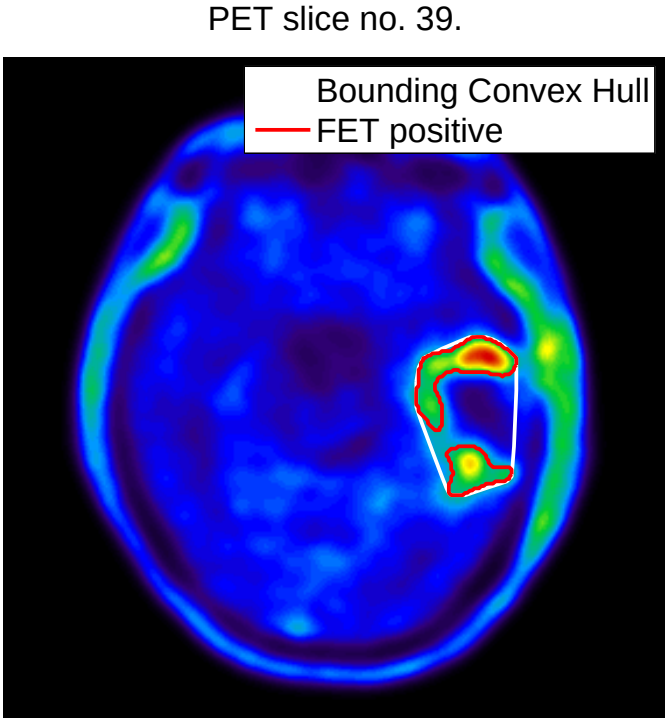

(a) Pre-treatment FET

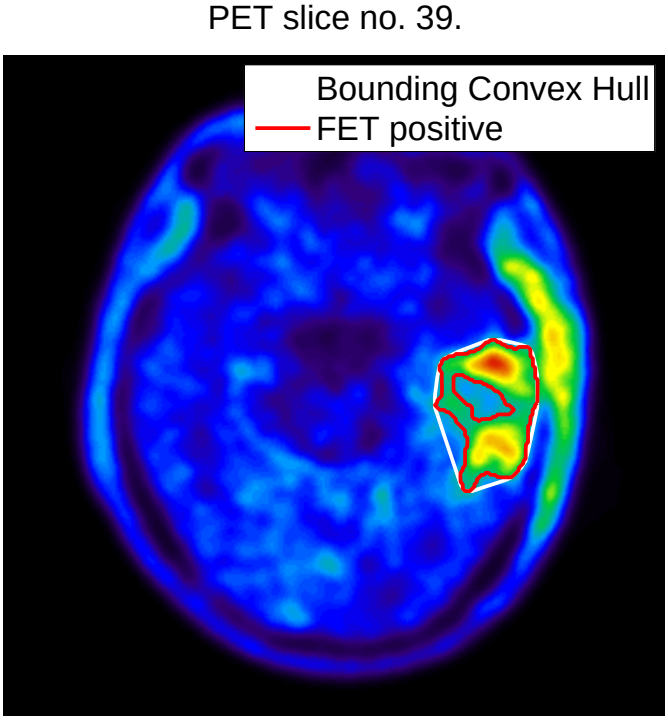

(b) Pre-treatment T1

Figure A.11: FET Scans patient 1.

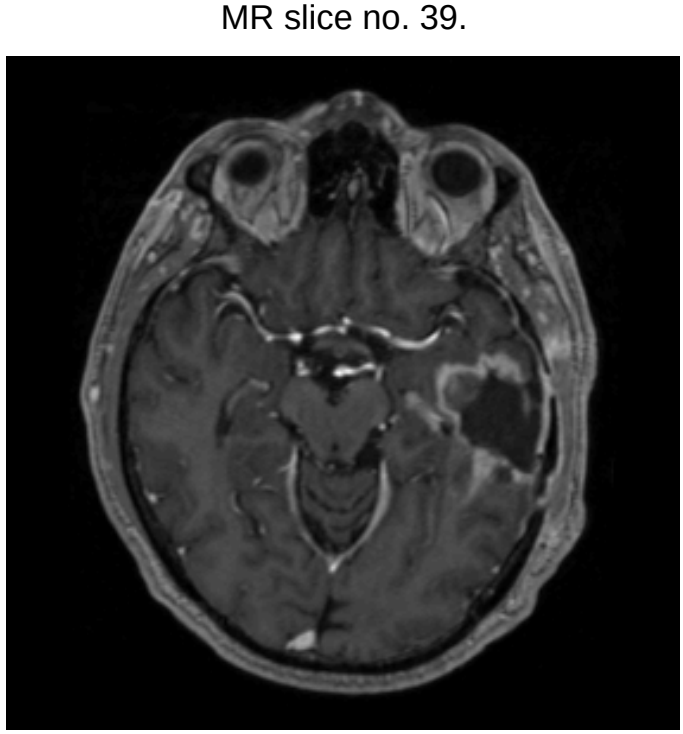

(a) Pre-treatment T1

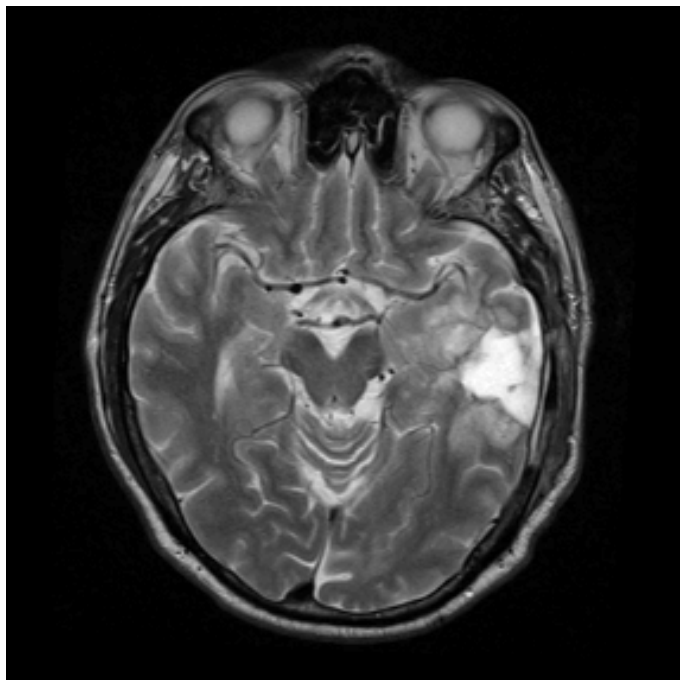

(b) Pre-treatment T2

Figure A.12: MRI patient 1.

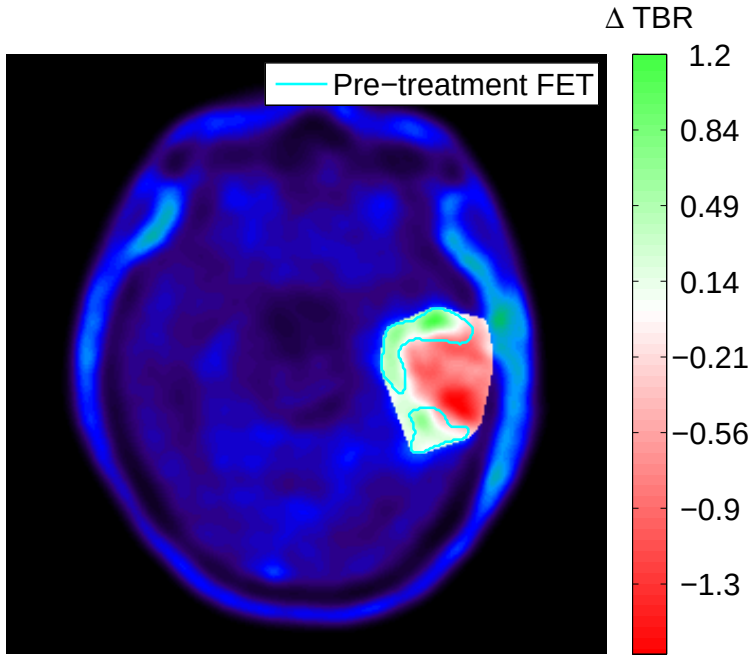

(a) Margin Map from FET volumes

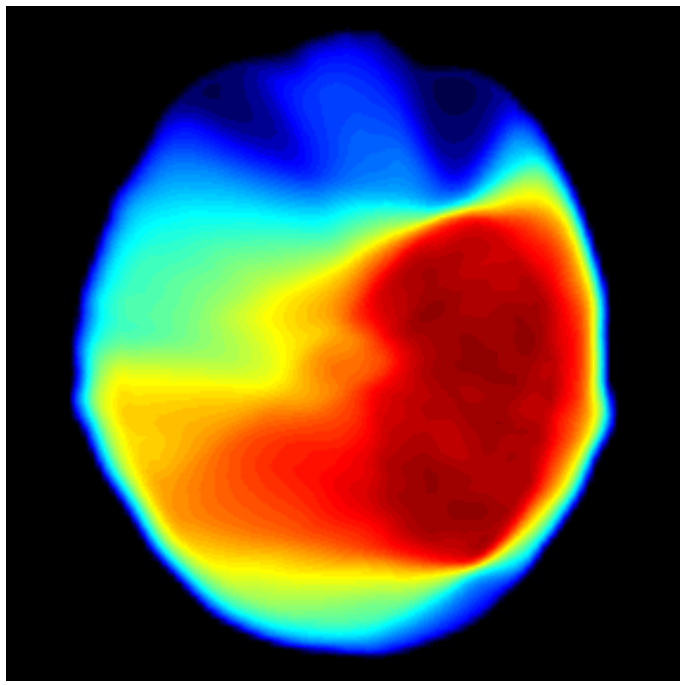

(b) Margin Map from convex hull

Figure A.13: Doseplan and response map patient 1.

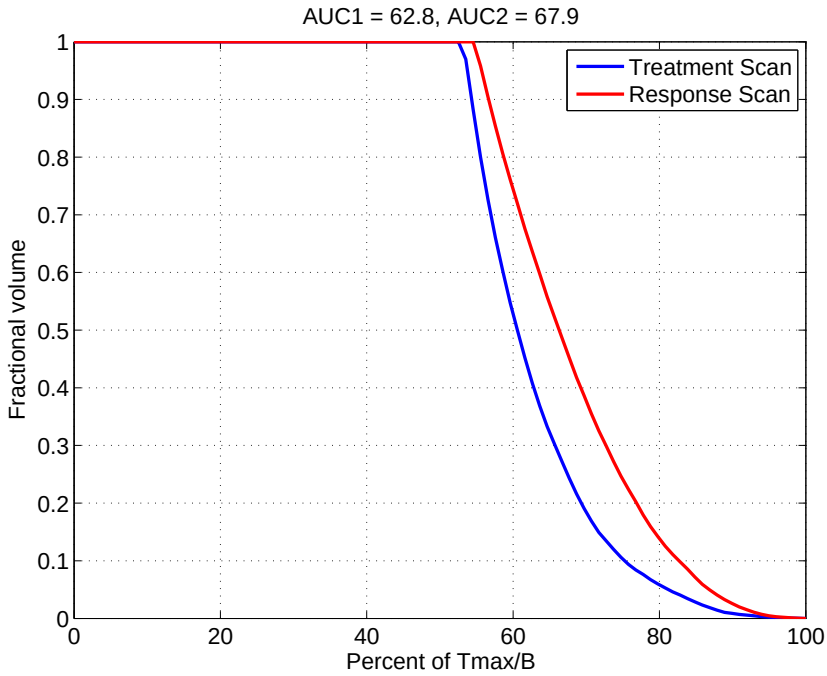

(a) Margin Map from convex hull

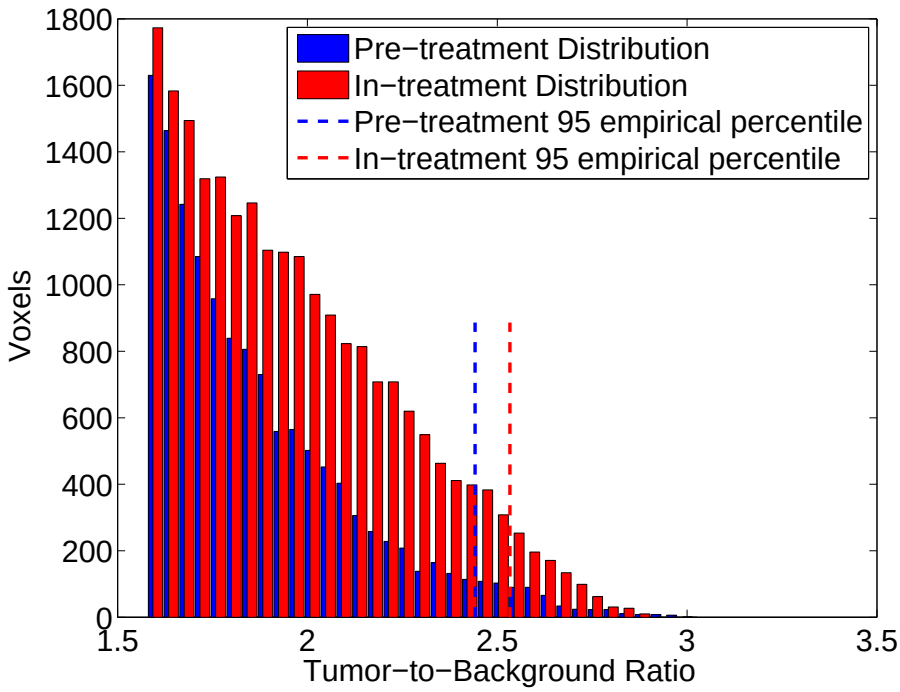

(b) Margin Map from convex hull

Figure A.14: Change in IVH and TBR distribution patient 1.

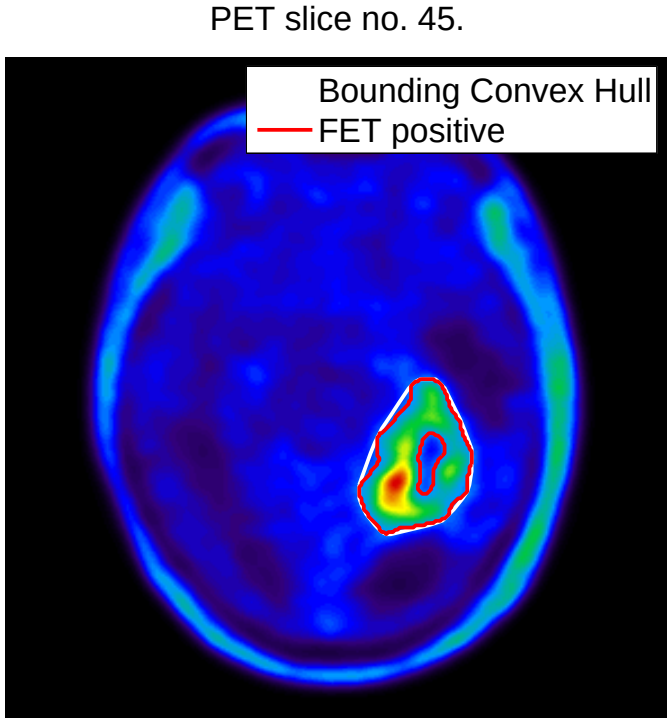

(a) Pre-treatment FET

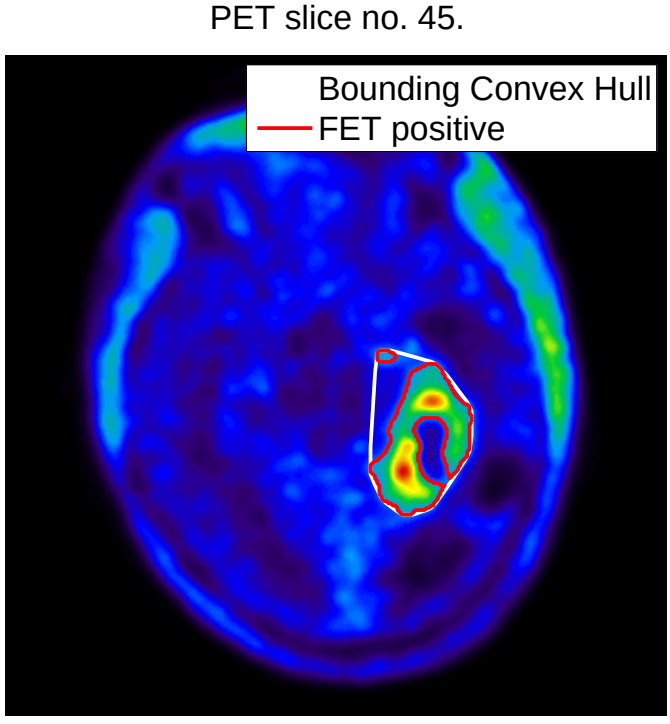

(b) Pre-treatment T1

Figure A.15: FET Scans patient 2.

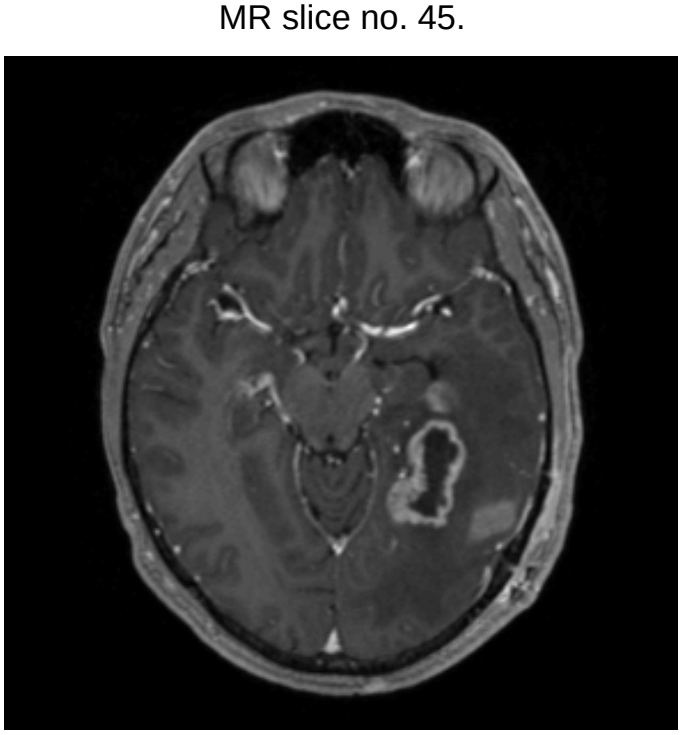

(a) Pre-treatment T1

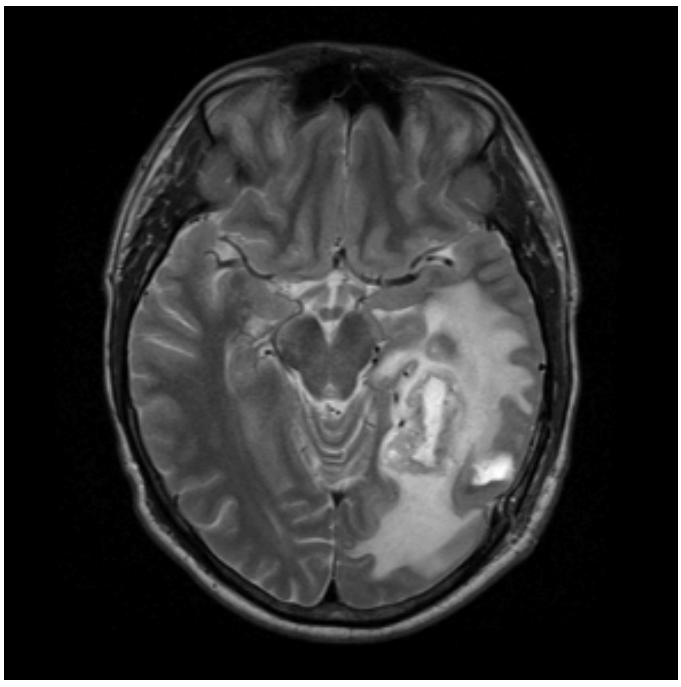

(b) Pre-treatment T2

Figure A.16: MRI patient 2.

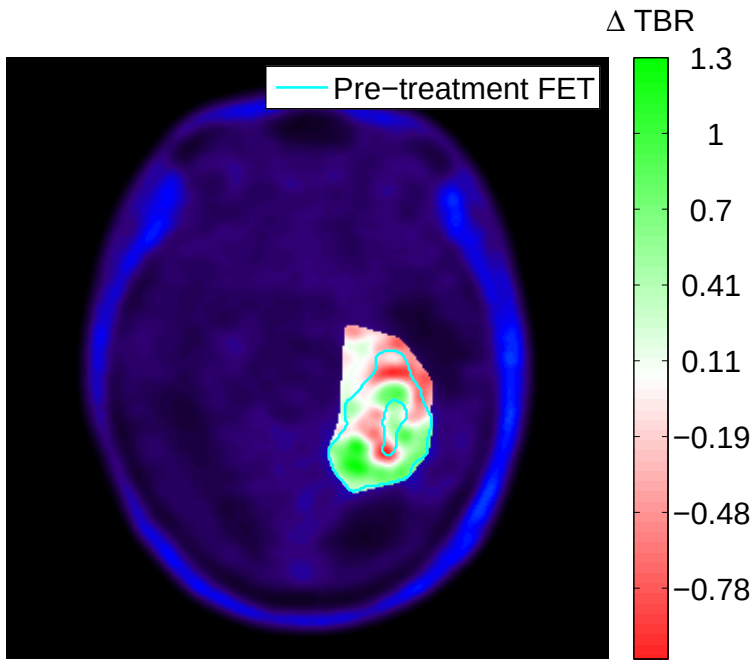

(a) Margin Map from FET volumes

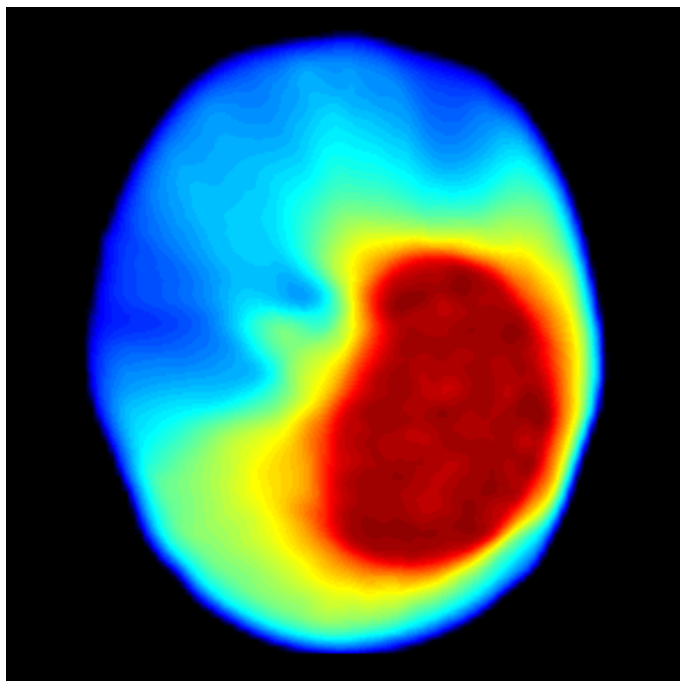

(b) Margin Map from convex hull

Figure A.17: Doseplan and response map patient 2.

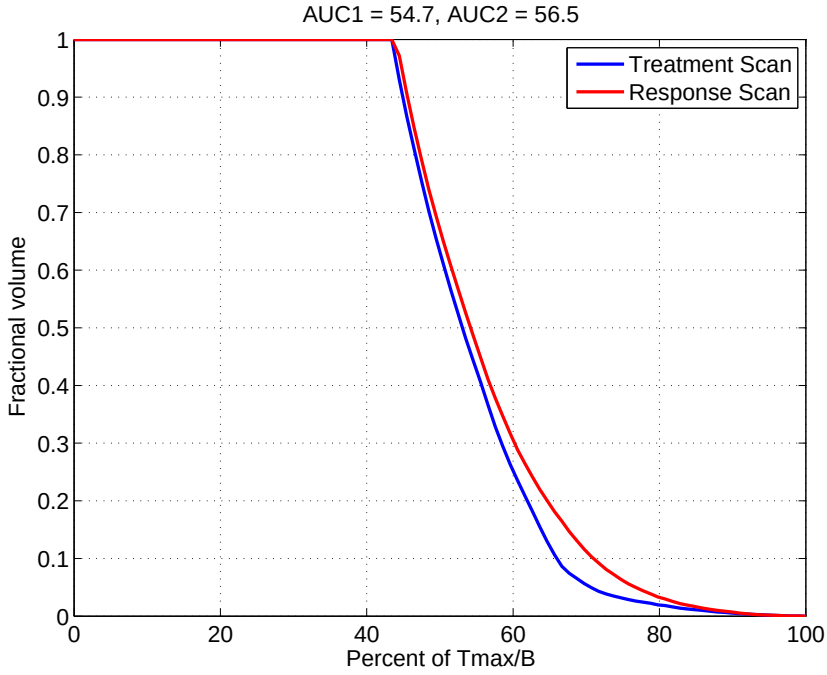

(a) Margin Map from convex hull

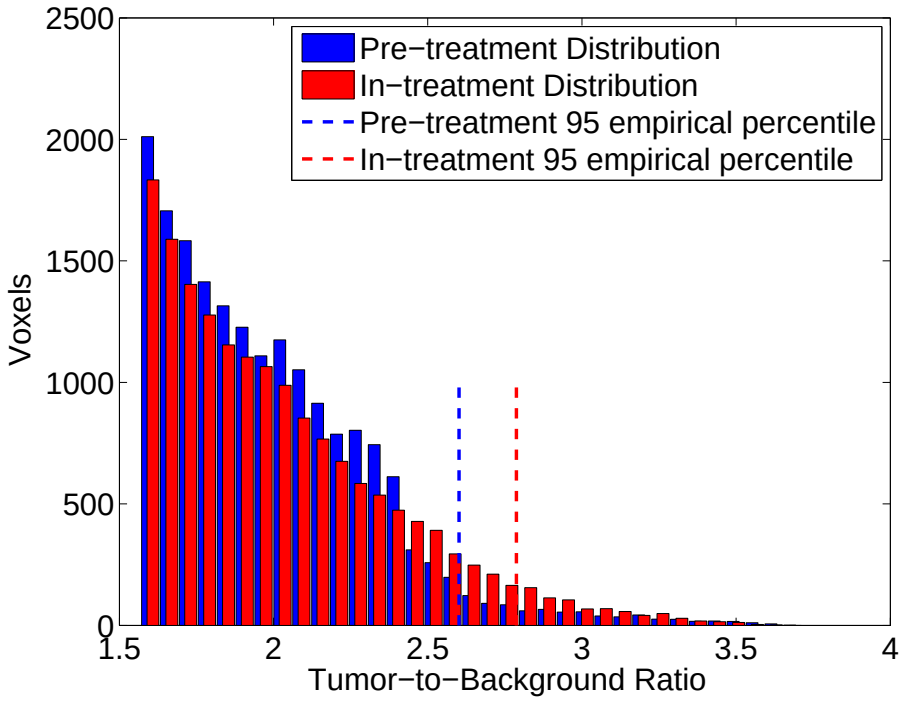

(b) Margin Map from convex hull

Figure A.18: Change in IVH and TBR distribution patient 2.

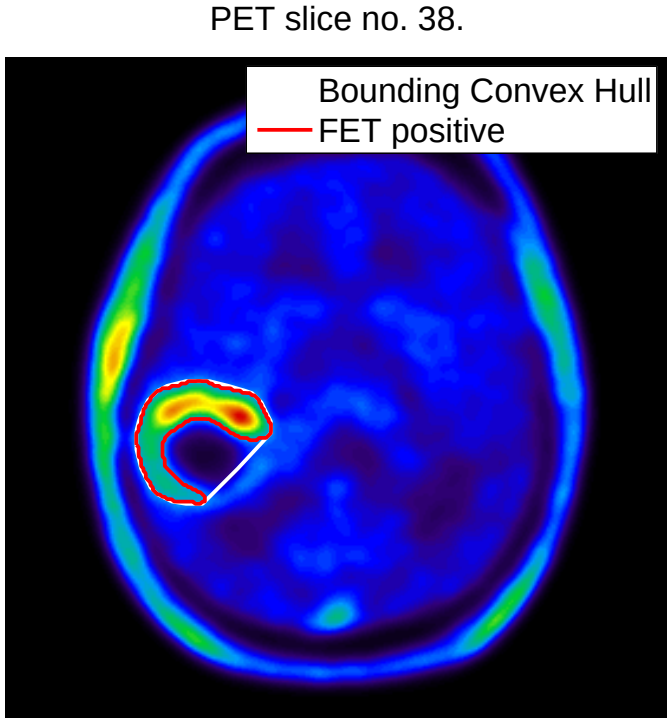

(a) Pre-treatment FET

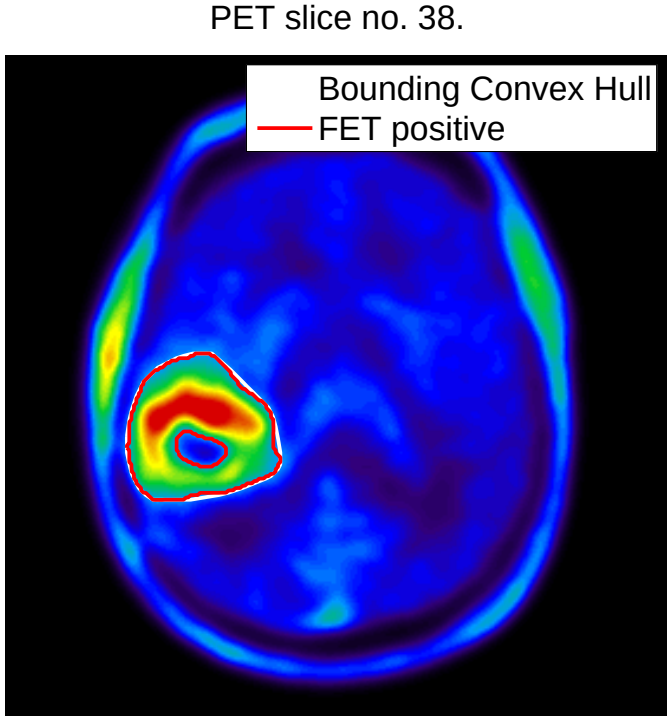

(b) Pre-treatment T1

Figure A.19: FET Scans patient 3.

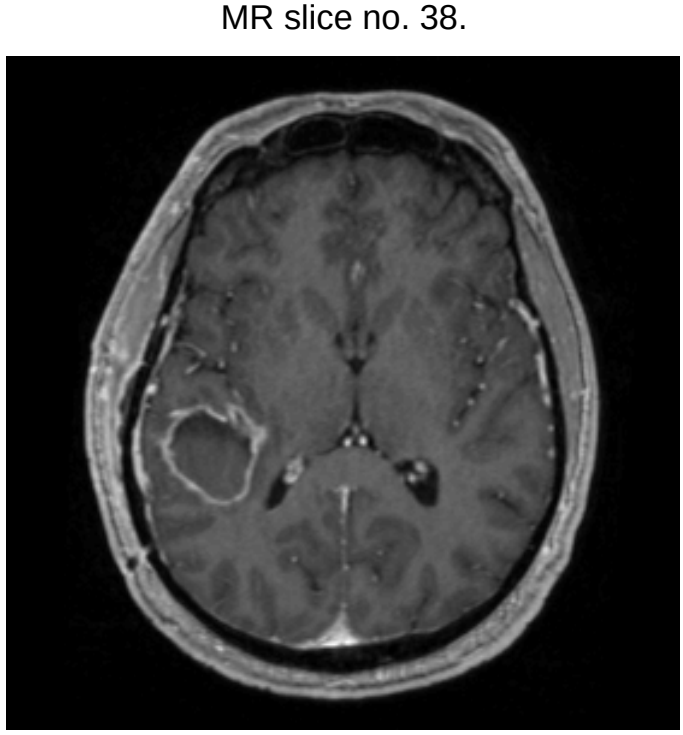

(a) Pre-treatment T1

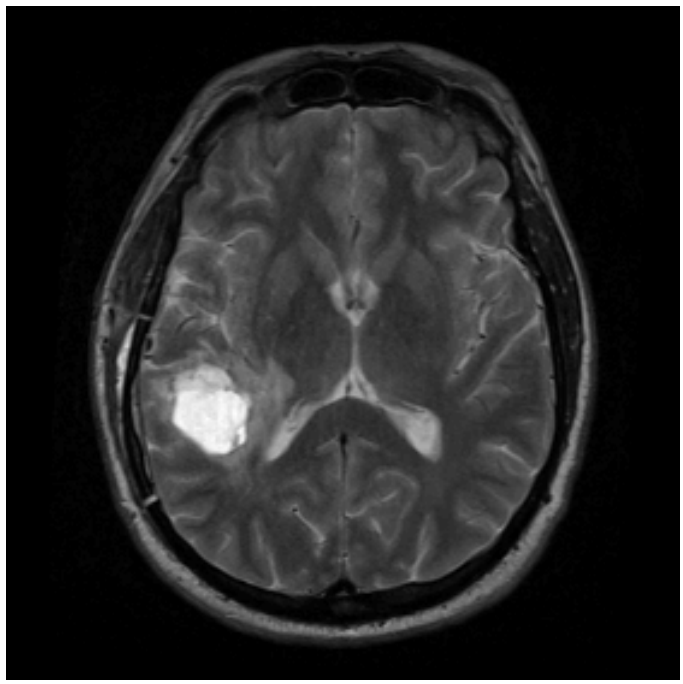

(b) Pre-treatment T2

Figure A.20: MRI patient 3.

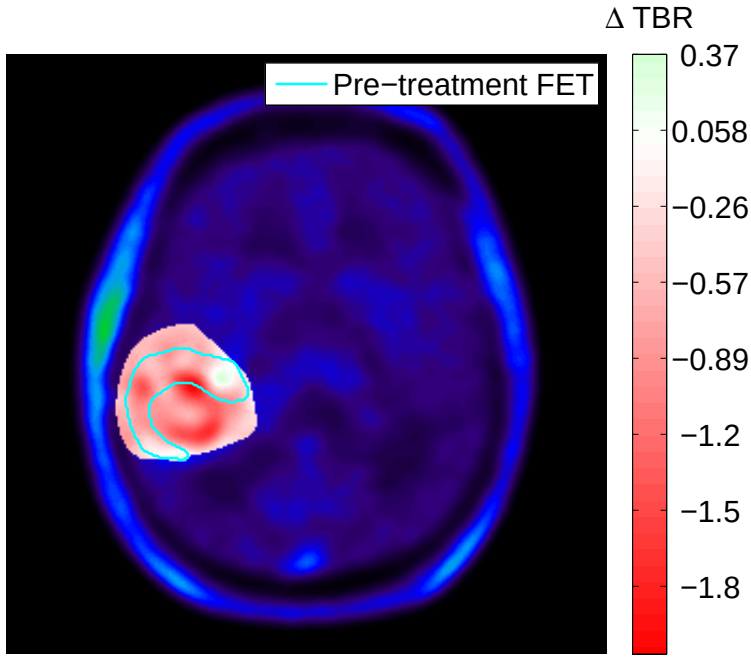

(a) Margin Map from FET volumes

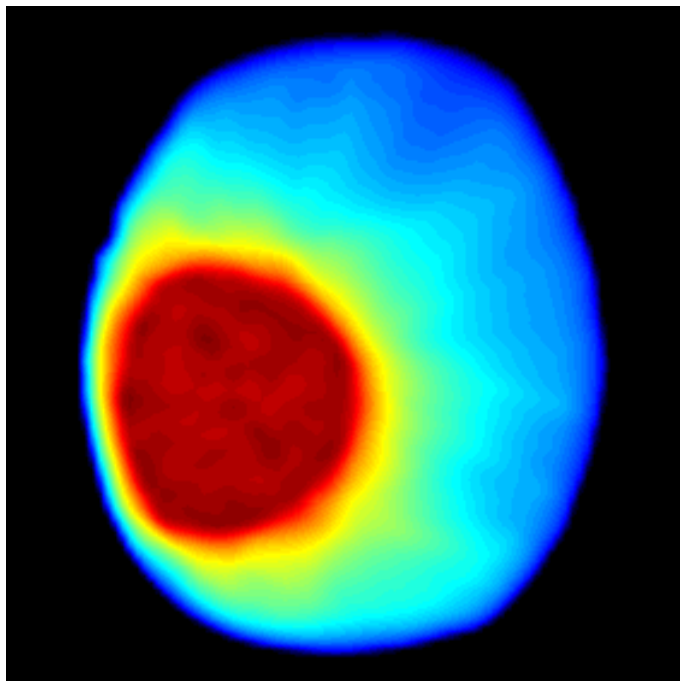

(b) Margin Map from convex hull

Figure A.21: Doseplan and response map patient 3.

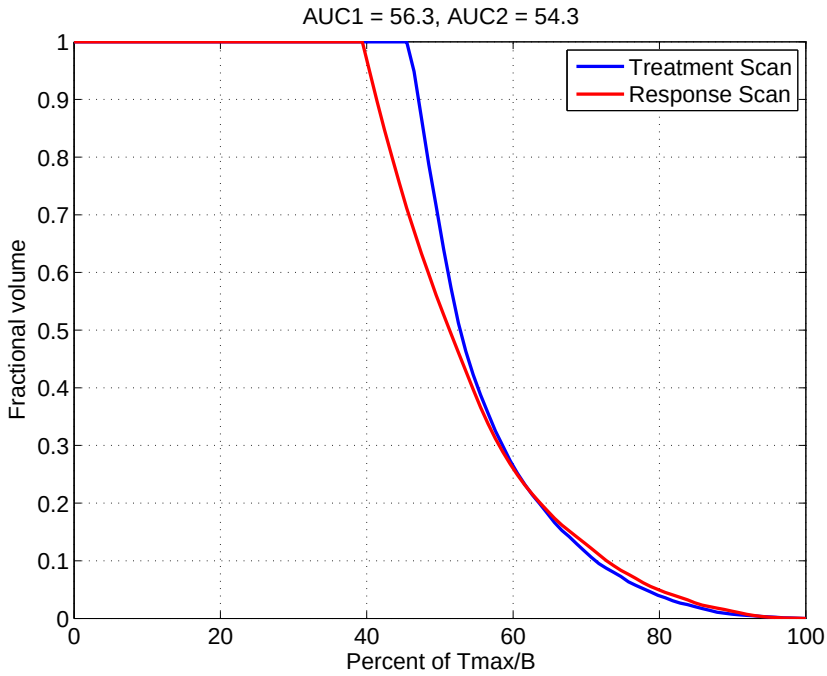

(a) Margin Map from convex hull

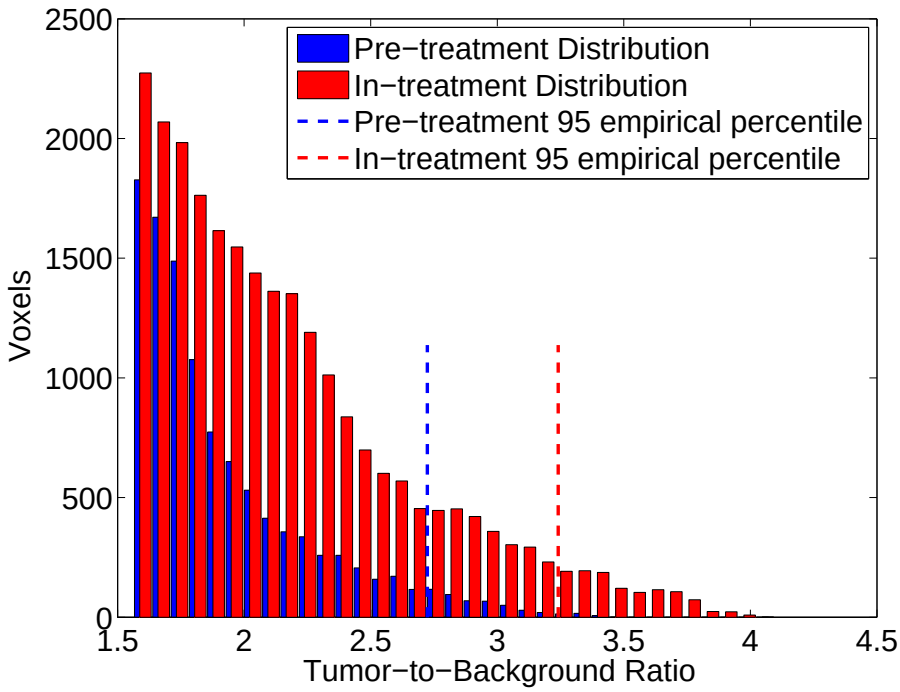

(b) Margin Map from convex hull

Figure A.22: Change in IVH and TBR distribution patient 3.

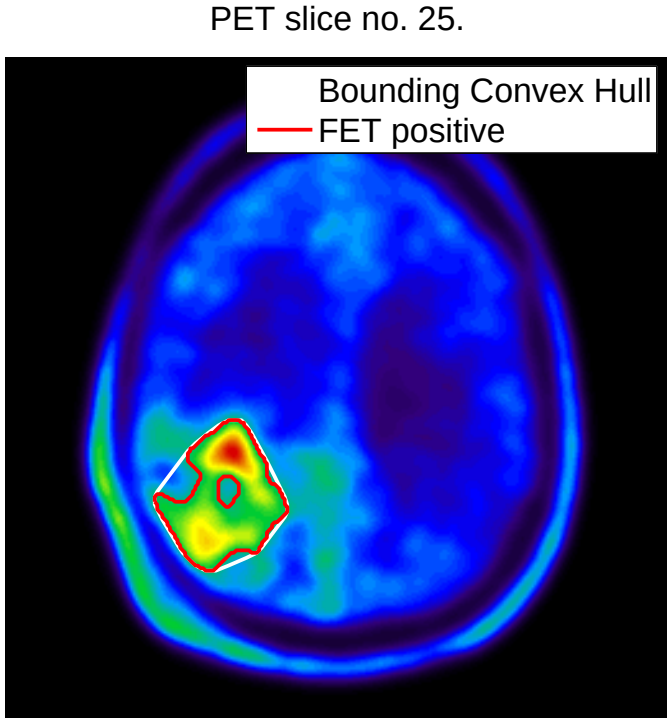

(a) Pre-treatment FET

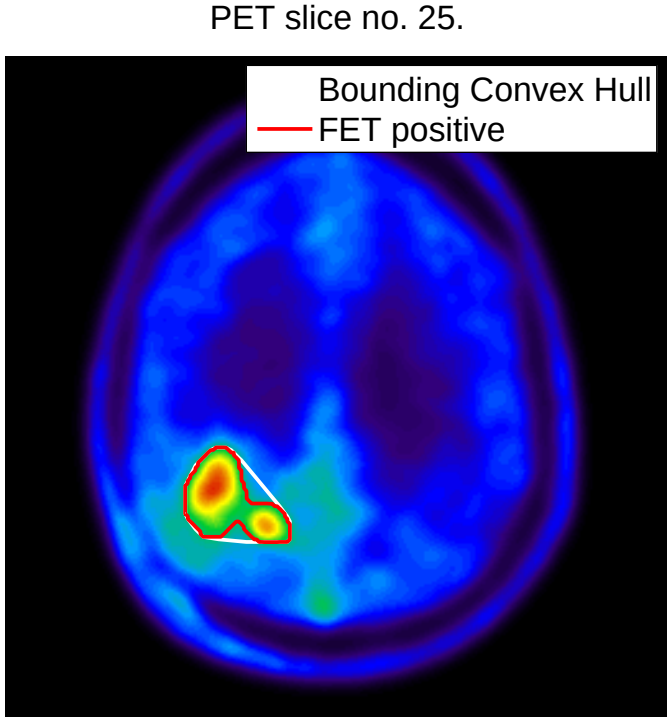

(b) Pre-treatment T1

Figure A.23: FET Scans patient 4.

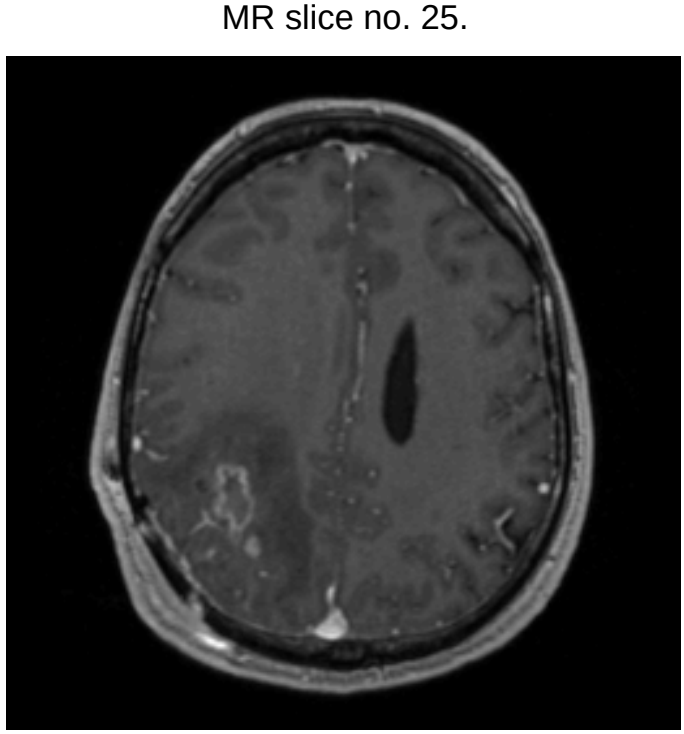

(a) Pre-treatment T1

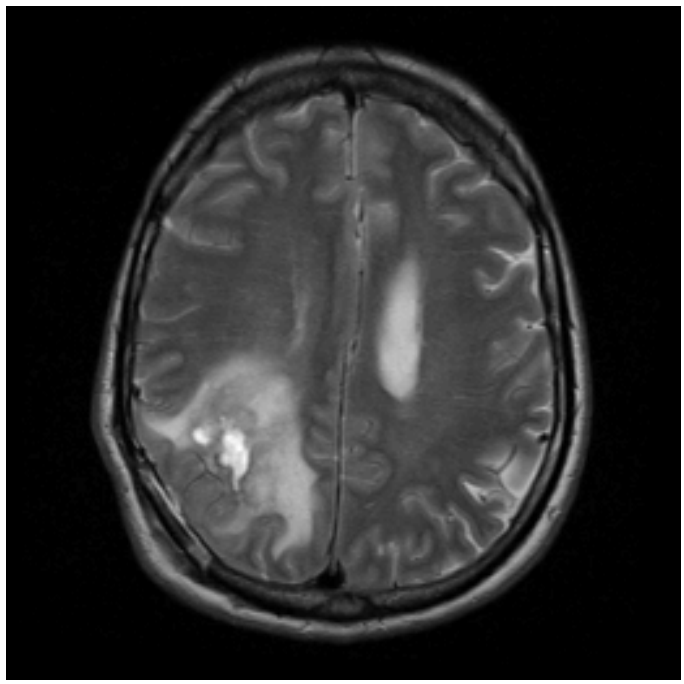

(b) Pre-treatment T2

Figure A.24: MRI patient 4.

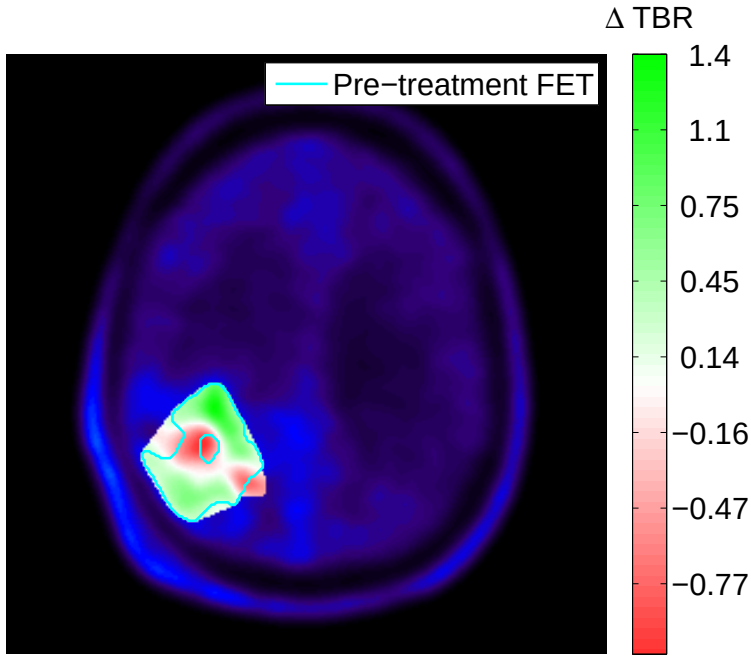

(a) Margin Map from FET volumes

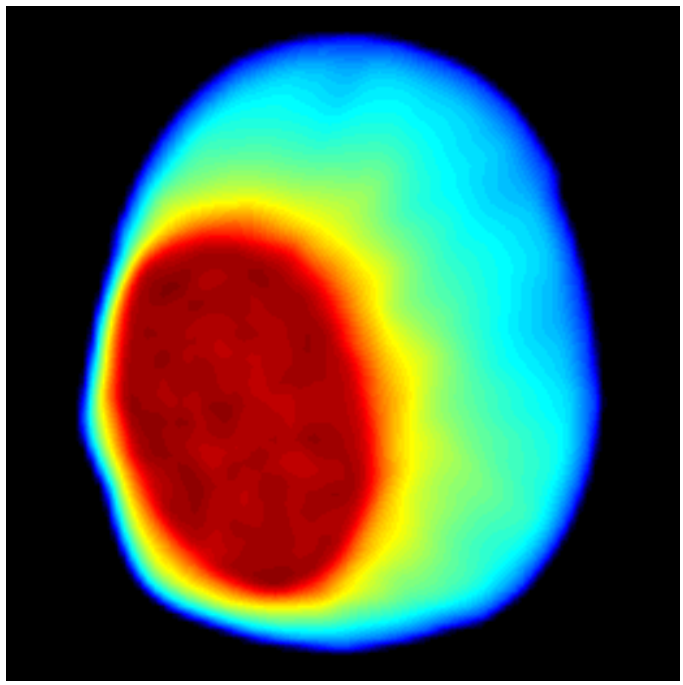

(b) Margin Map from convex hull

Figure A.25: Doseplan and response map patient 4.

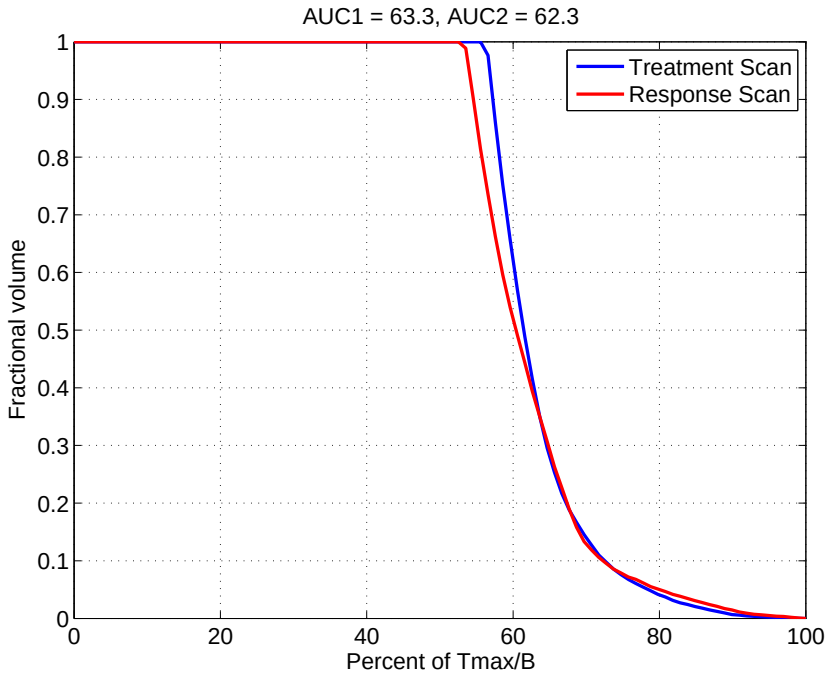

(a) Margin Map from convex hull

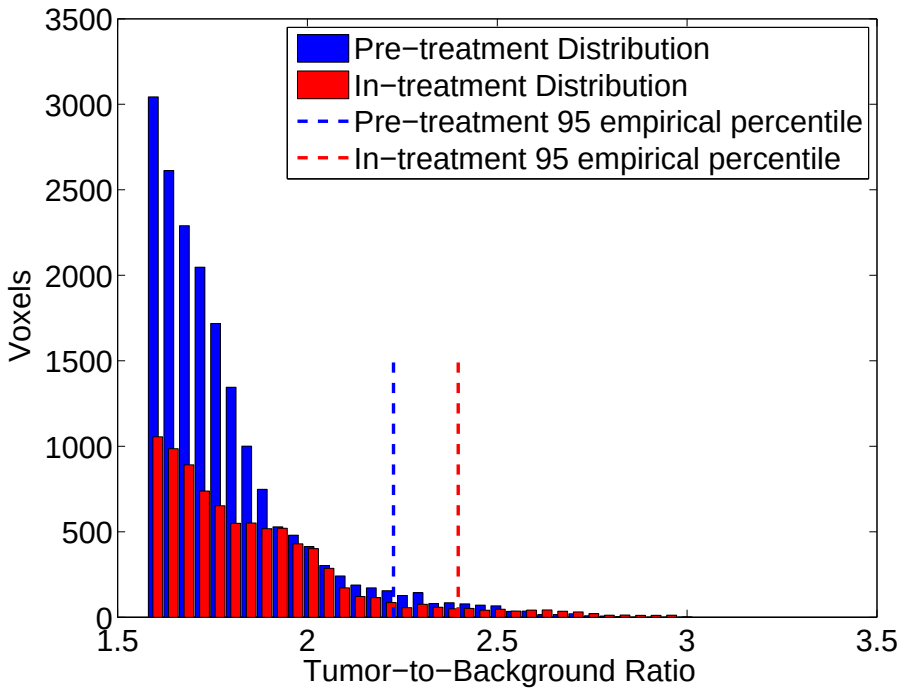

(b) Margin Map from convex hull

Figure A.26: Change in IVH and TBR distribution patient 4.

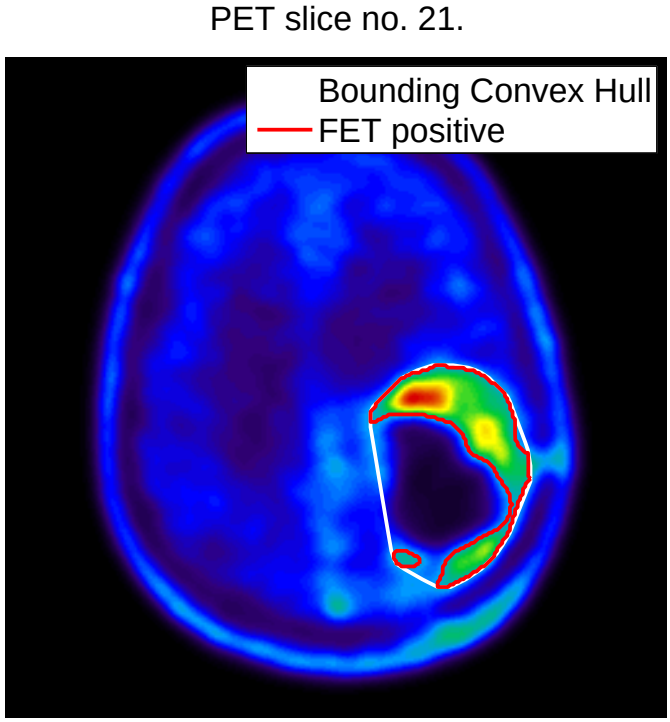

(a) Pre-treatment FET

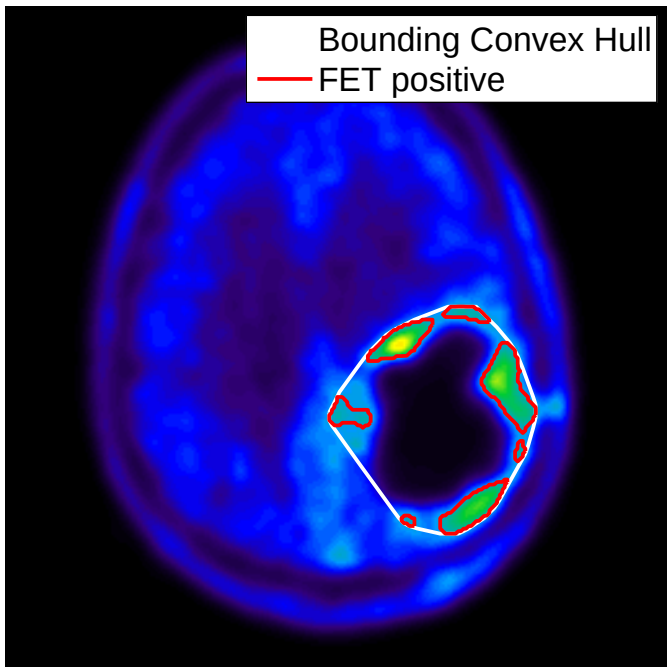

(b) Pre-treatment T1

Figure A.27: FET Scans patient 5.

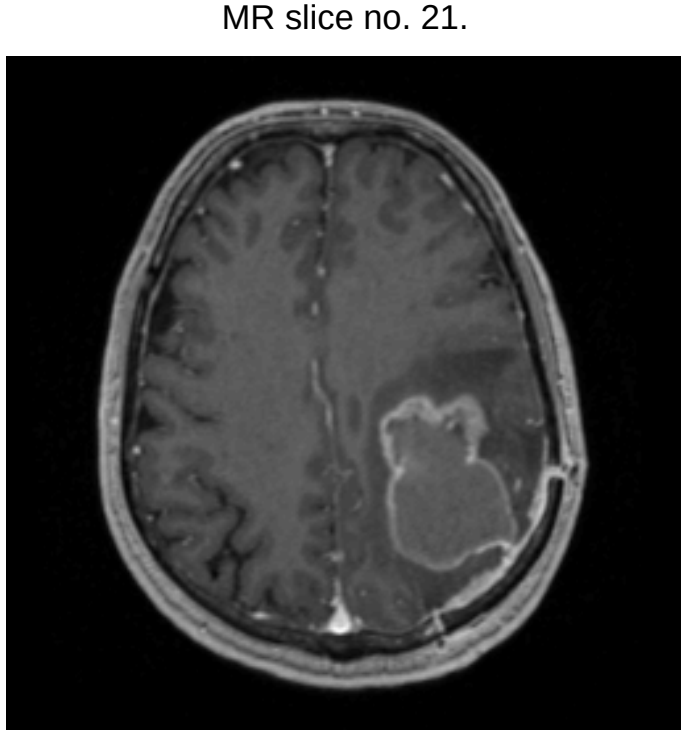

(a) Pre-treatment T1

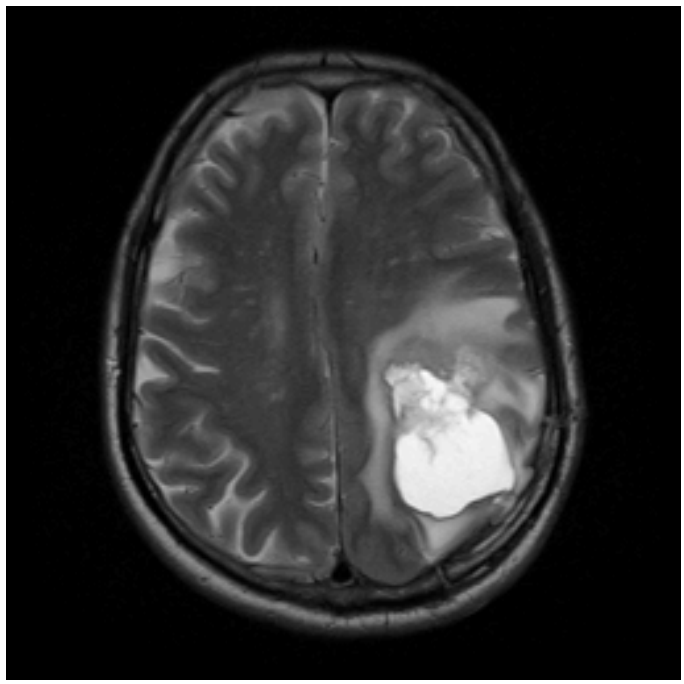

(b) Pre-treatment T2

Figure A.28: MRI patient 5.

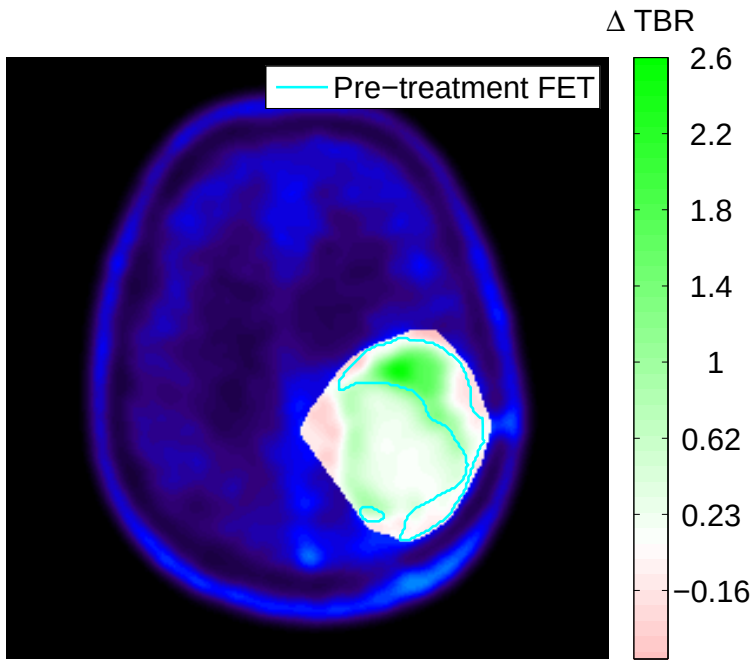

(a) Margin Map from FET volumes

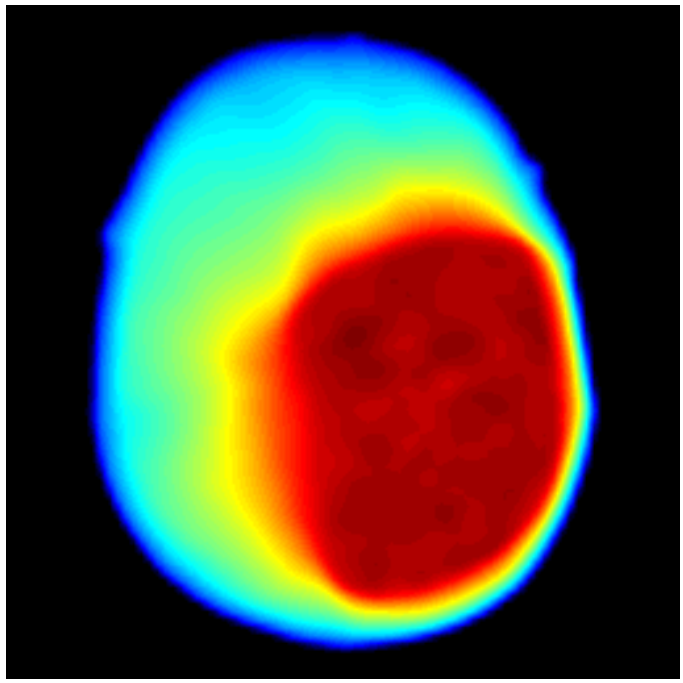

(b) Margin Map from convex hull

Figure A.29: Doseplan and response map patient 5.

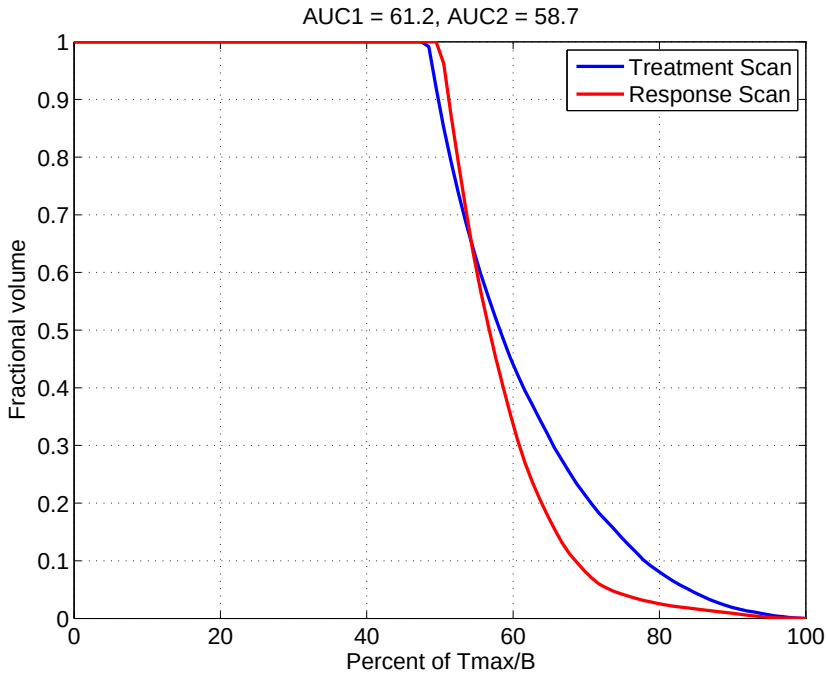

(a) Margin Map from convex hull

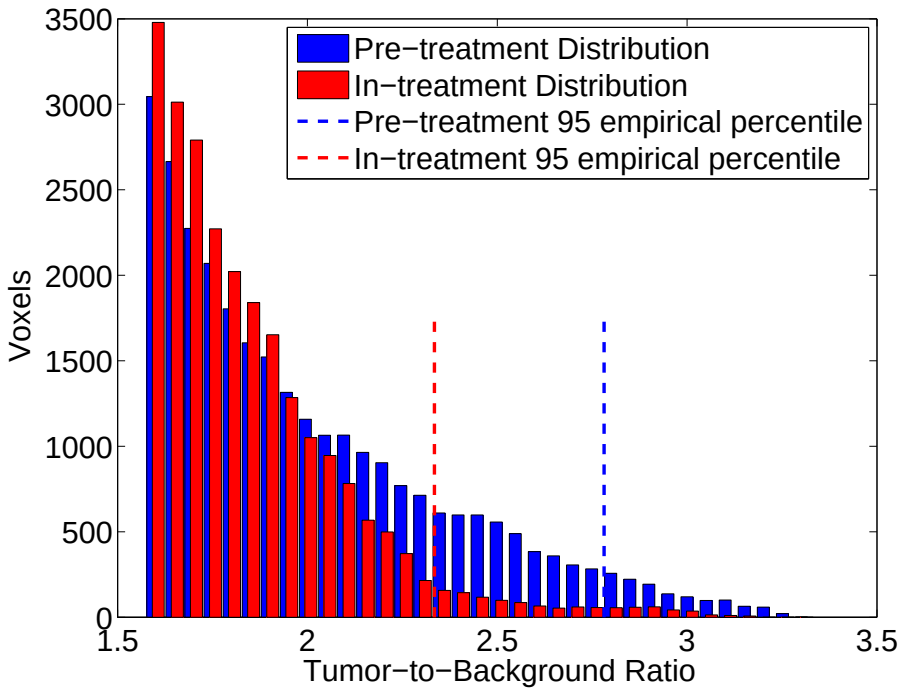

(b) Margin Map from convex hull

Figure A.30: Change in IVH and TBR distribution patient 5.

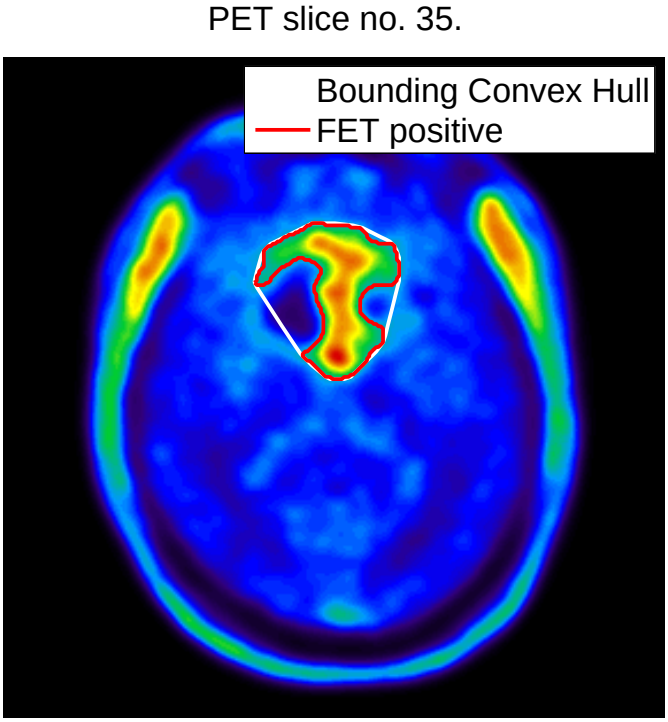

(a) Pre-treatment FET

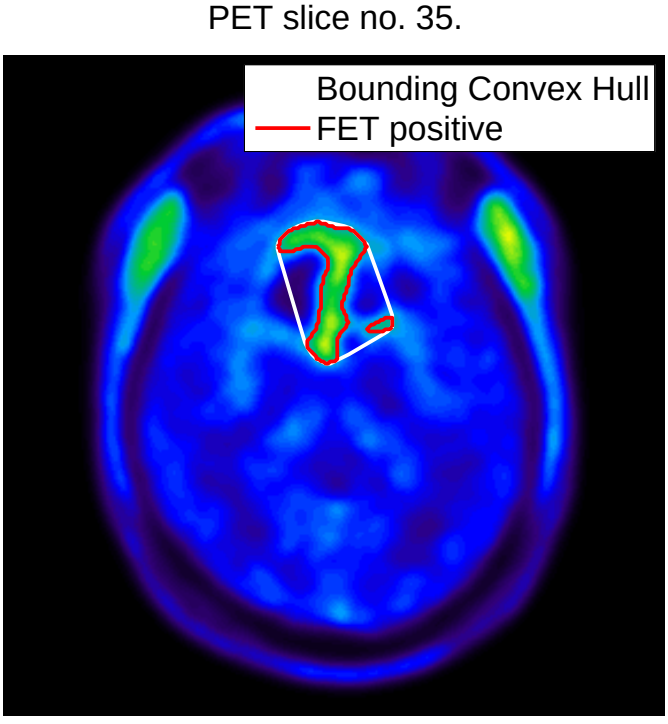

(b) Pre-treatment T1

Figure A.31: FET Scans patient 6.

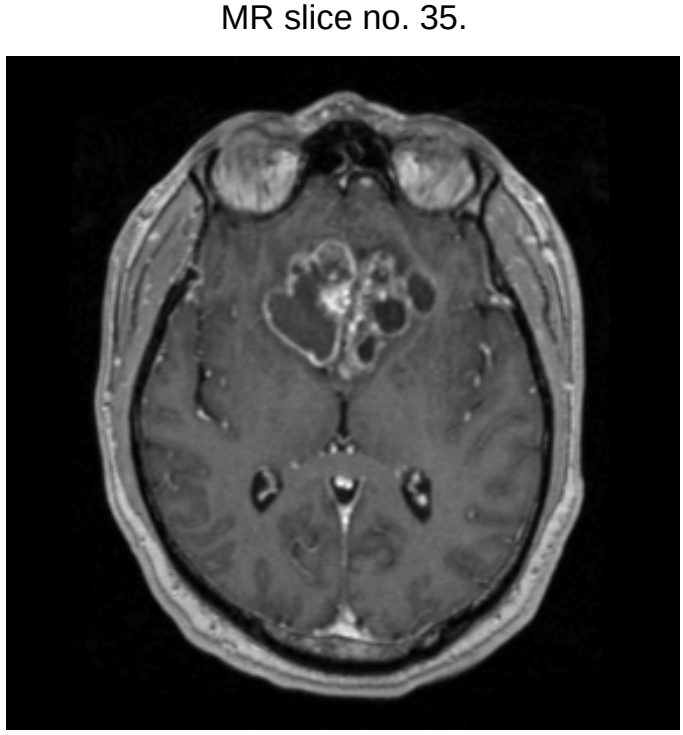

(a) Pre-treatment T1

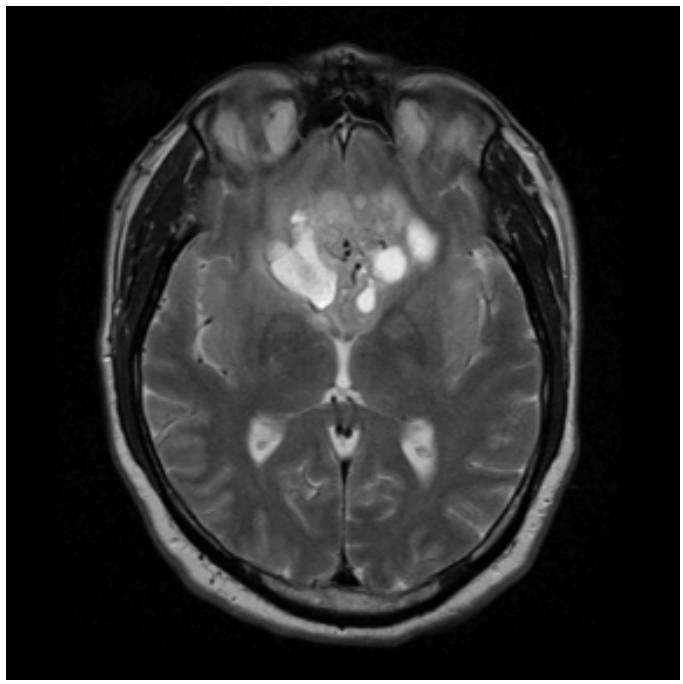

(b) Pre-treatment T2

Figure A.32: MRI patient 6.

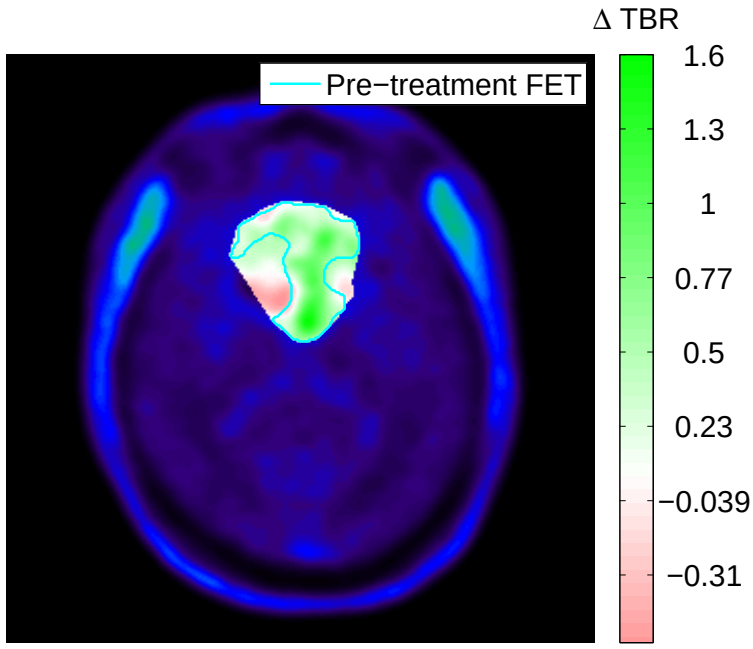

(a) Margin Map from FET volumes

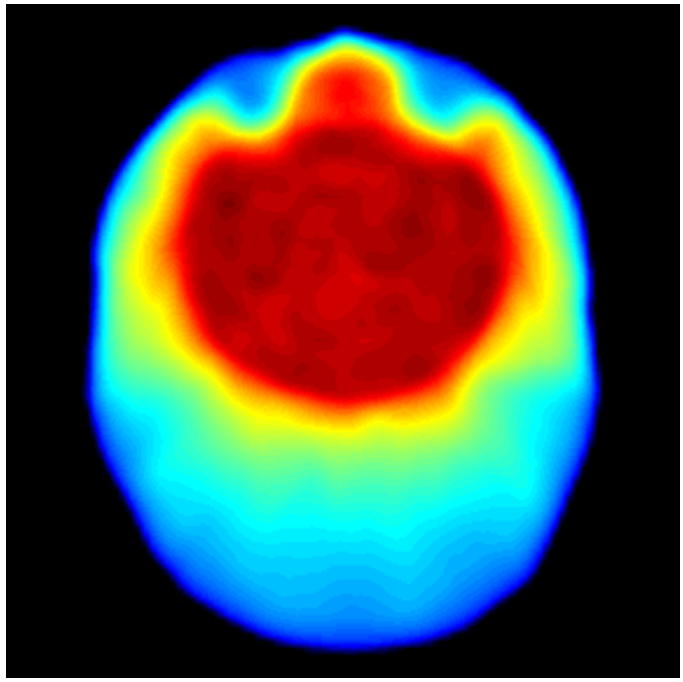

(b) Margin Map from convex hull

Figure A.33: Doseplan and response map patient 6.

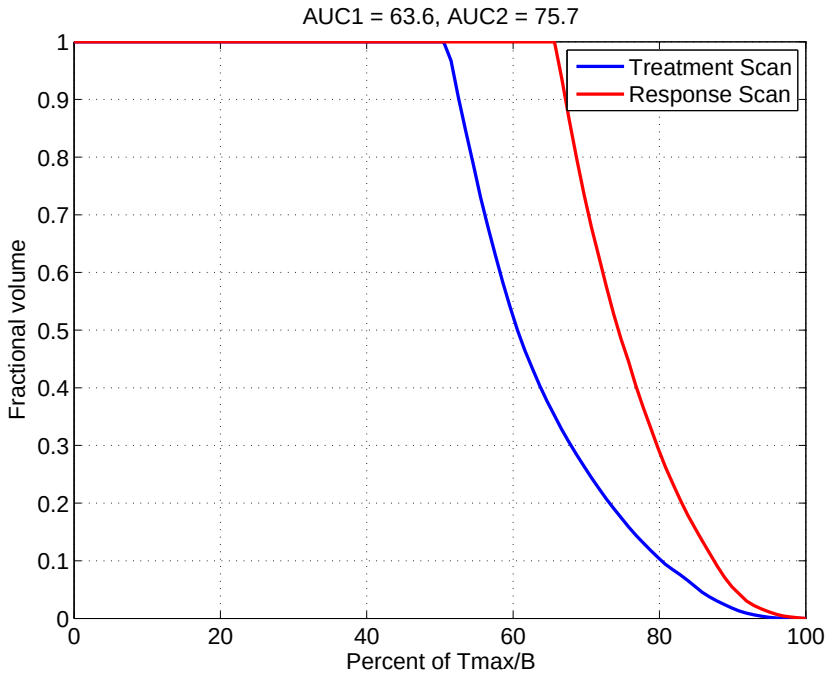

(a) Margin Map from convex hull

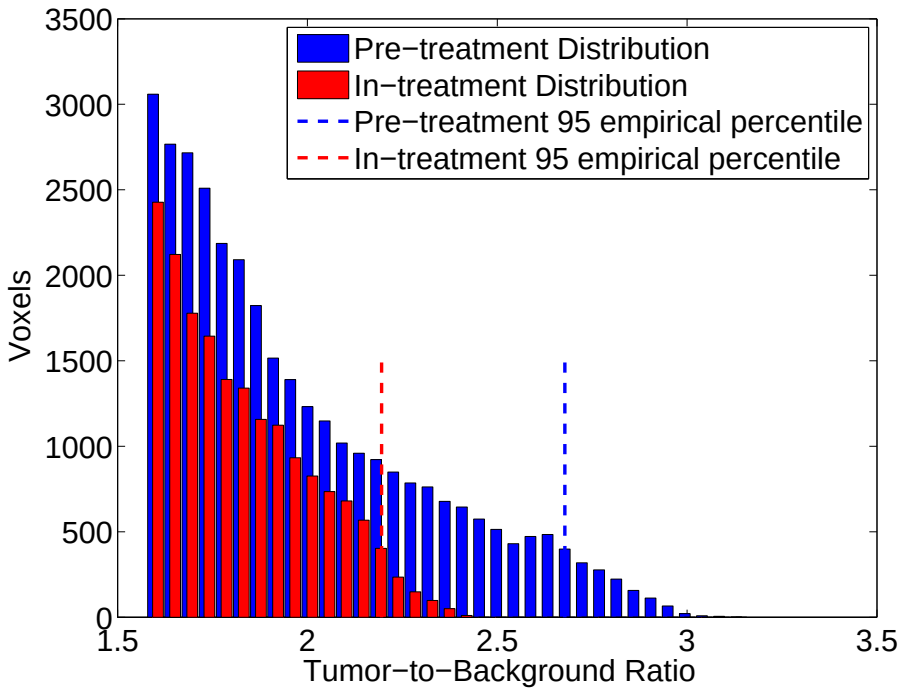

(b) Margin Map from convex hull

Figure A.34: Change in IVH and TBR distribution patient 6.

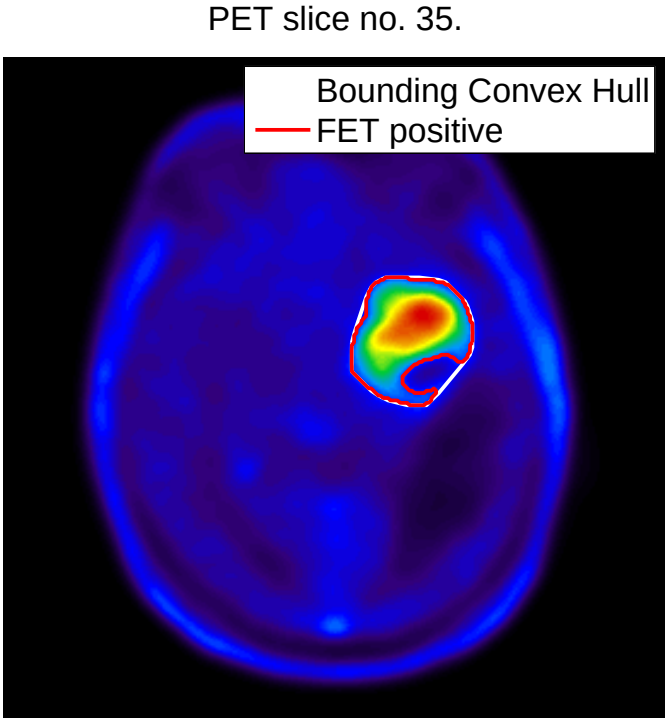

(a) Pre-treatment FET

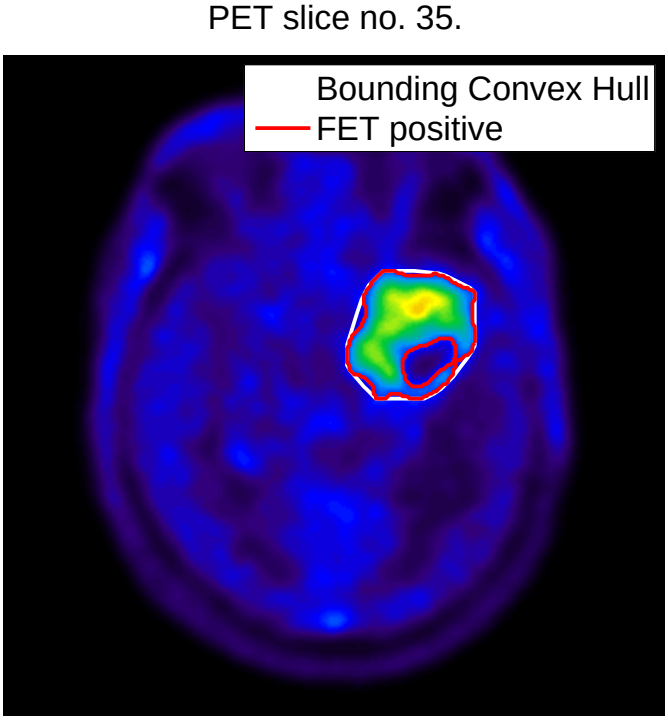

(b) Pre-treatment T1

Figure A.35: FET Scans patient 7.

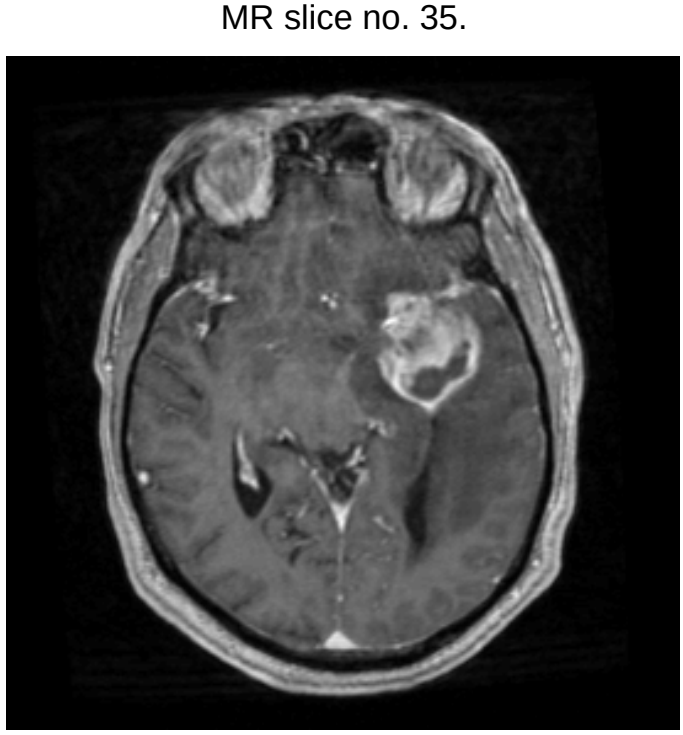

(a) Pre-treatment T1

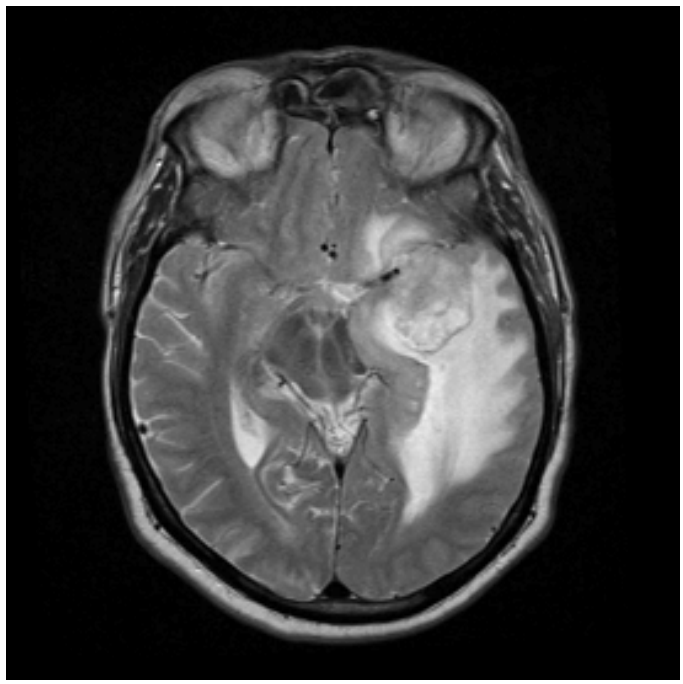

(b) Pre-treatment T2

Figure A.36: MRI patient 7.

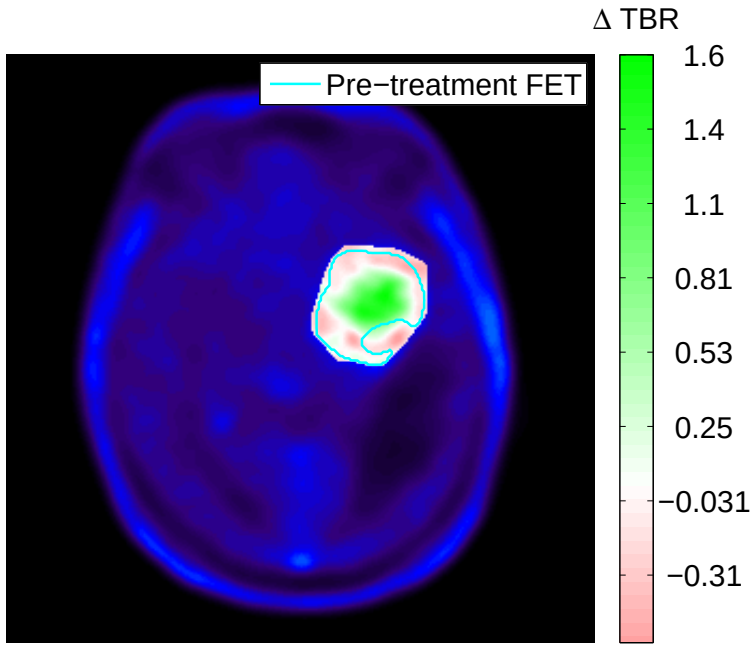

(a) Margin Map from FET volumes

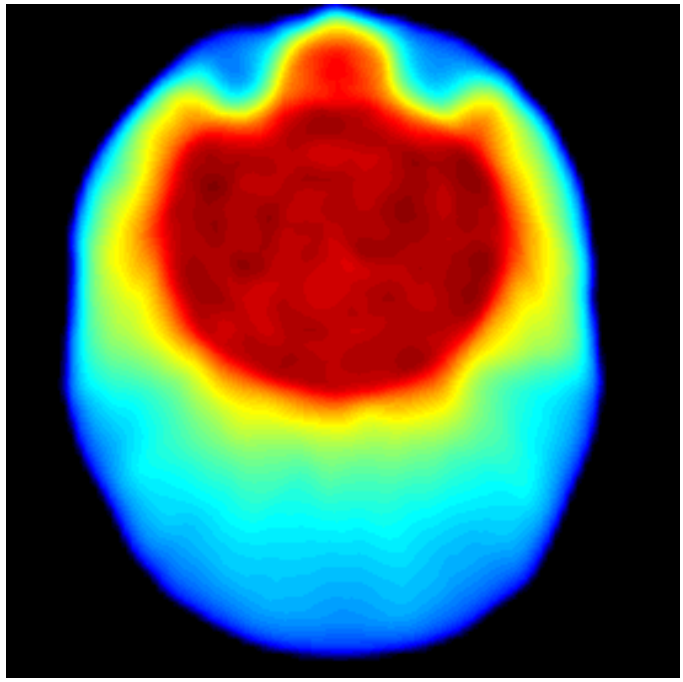

(b) Margin Map from convex hull

Figure A.37: Doseplan and response map patient 7.

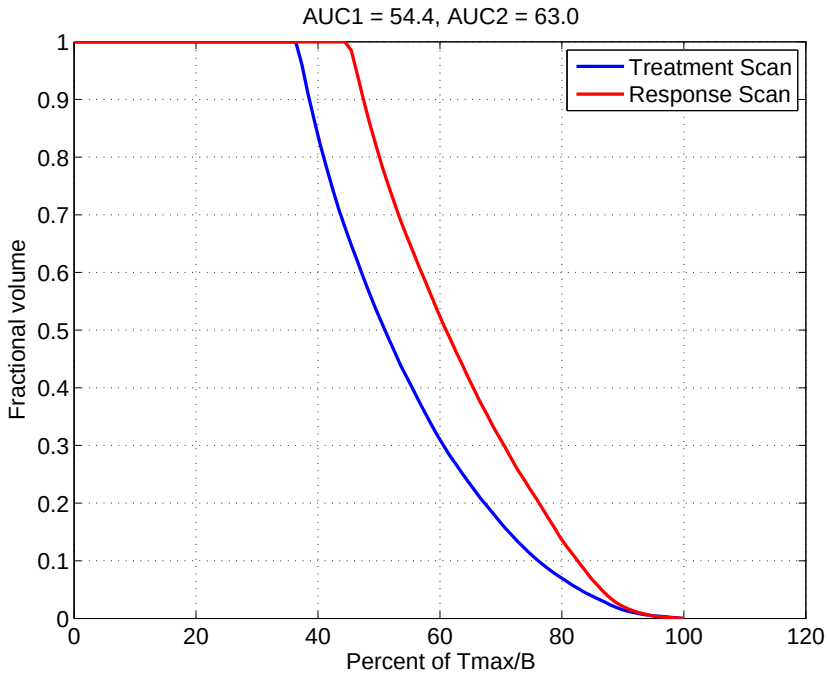

(a) Margin Map from convex hull

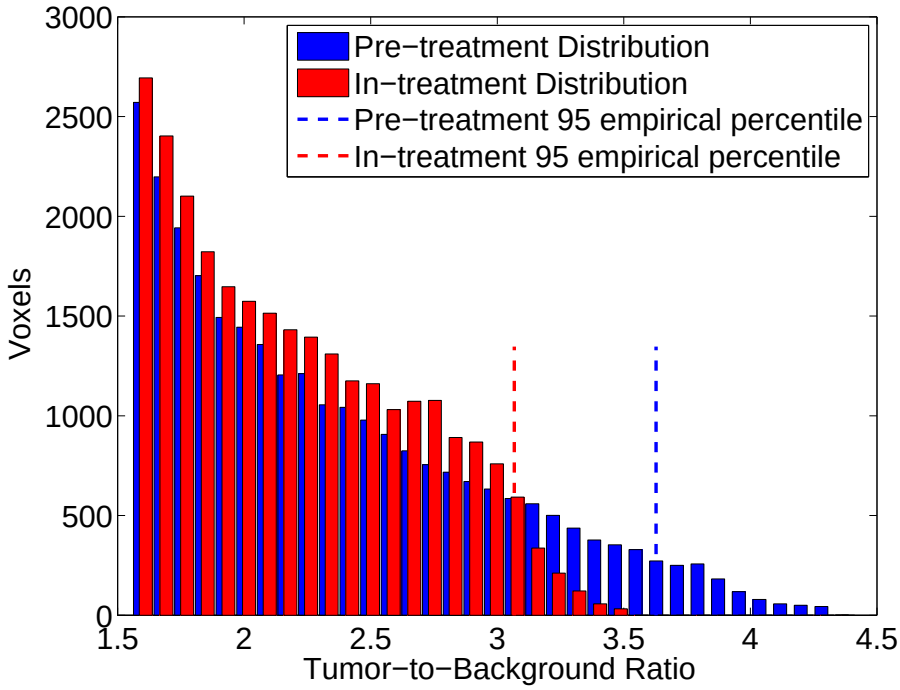

(b) Margin Map from convex hull

Figure A.38: Change in IVH and TBR distribution patient 7.

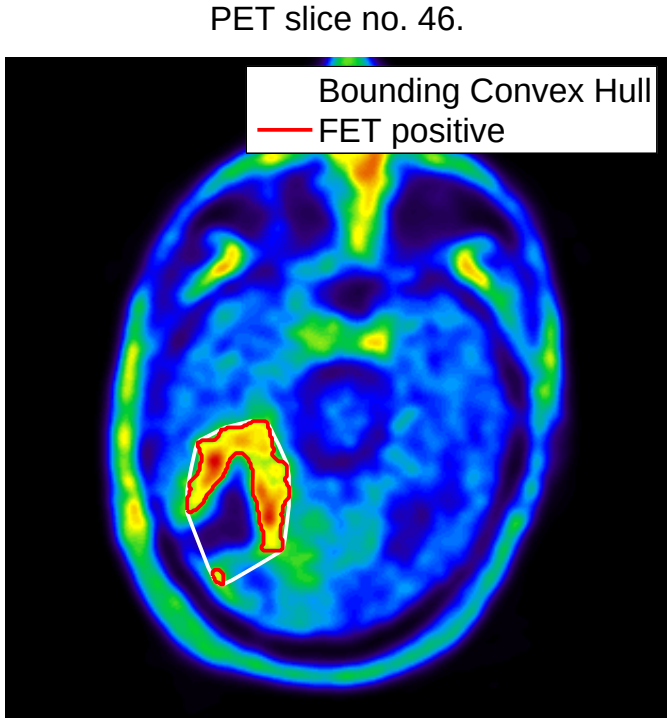

(a) Pre-treatment FET

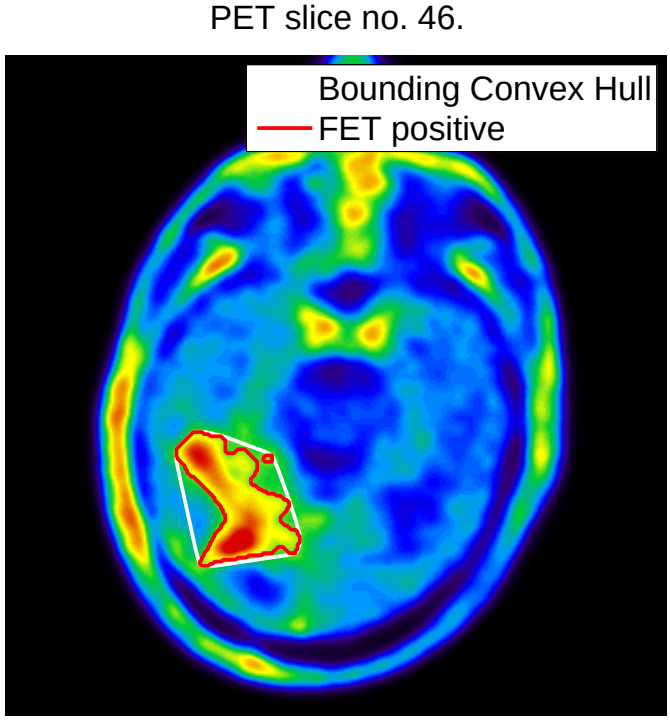

(b) Pre-treatment T1

Figure A.39: FET Scans patient 8.

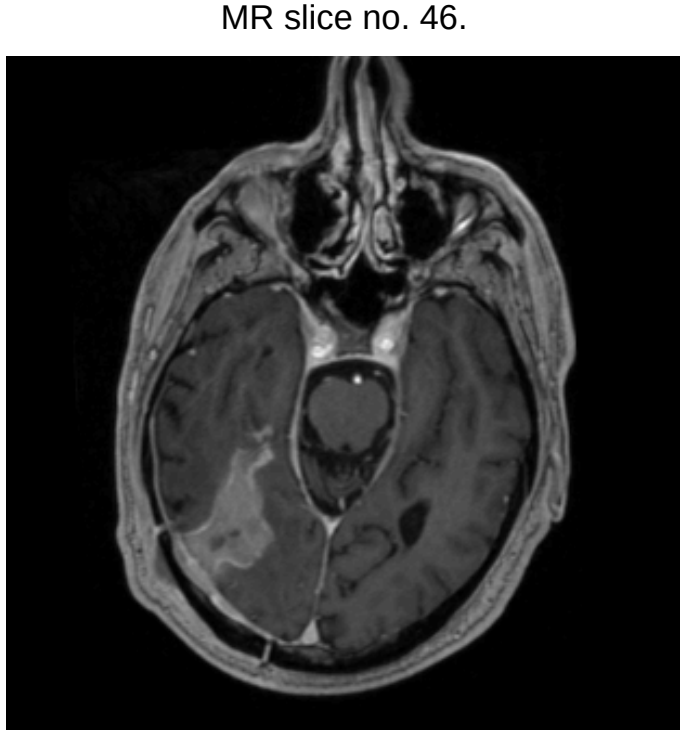

(a) Pre-treatment T1

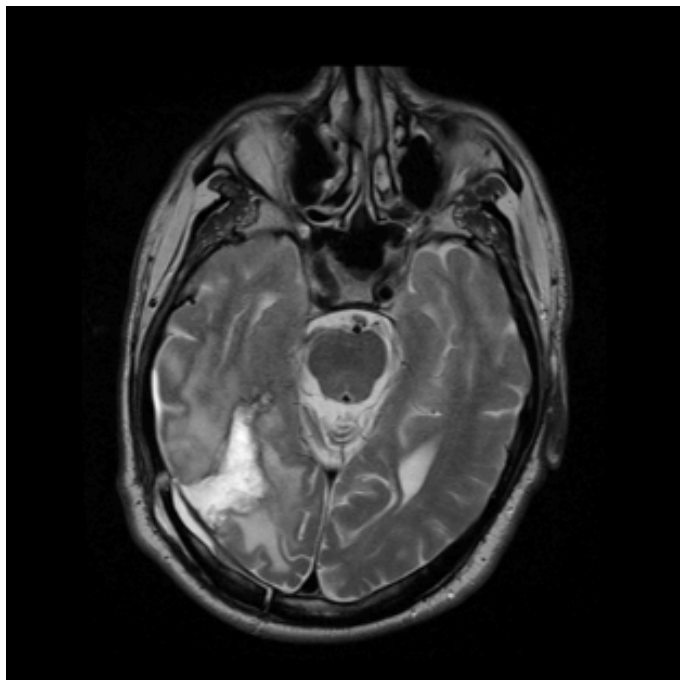

(b) Pre-treatment T2

Figure A.40: MRI patient 8.

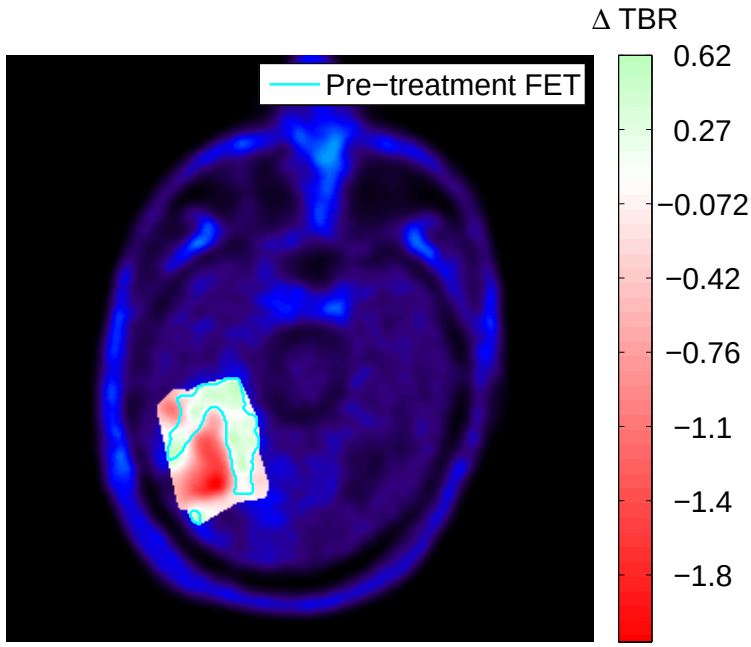

(a) Margin Map from FET volumes

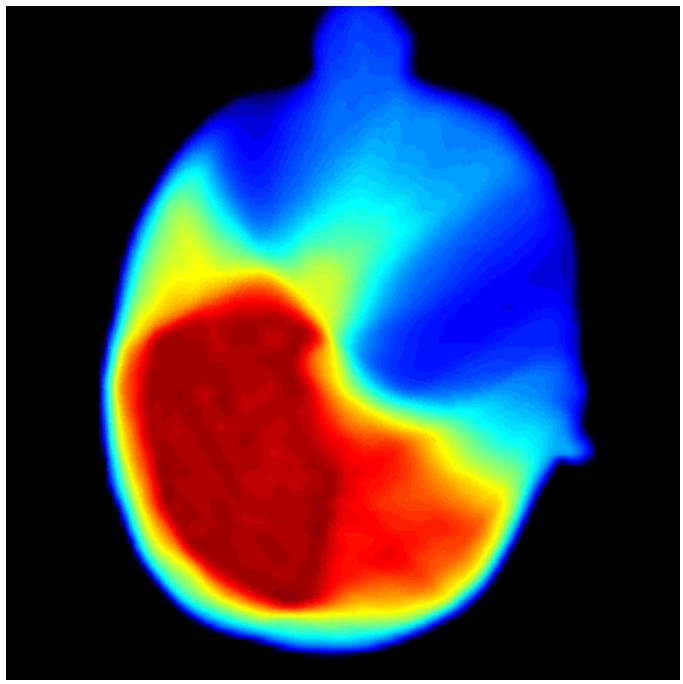

(b) Margin Map from convex hull

Figure A.41: Doseplan and response map patient 8.

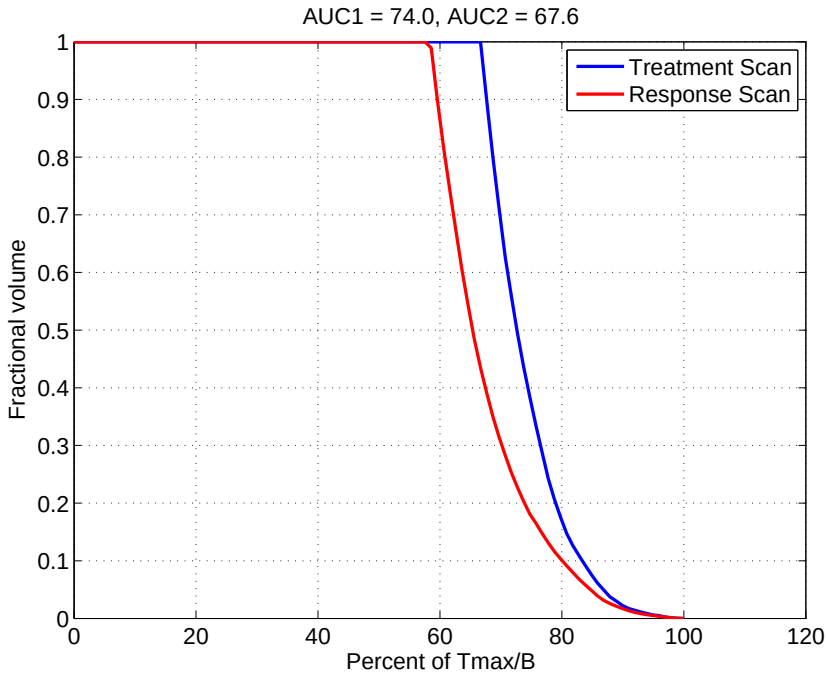

(a) Margin Map from convex hull

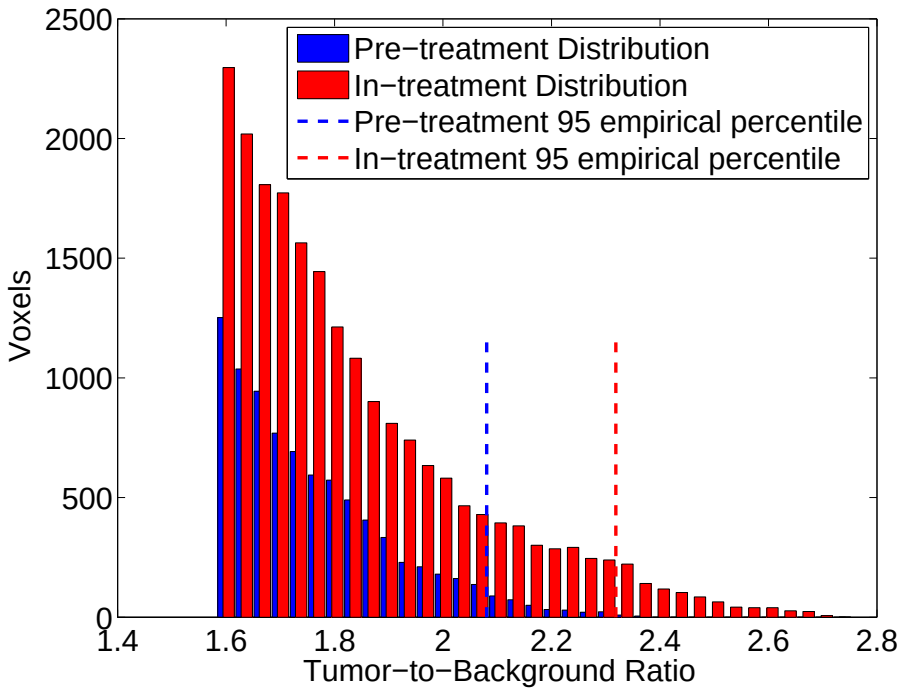

(b) Margin Map from convex hull

Figure A.42: Change in IVH and TBR distribution patient 8.

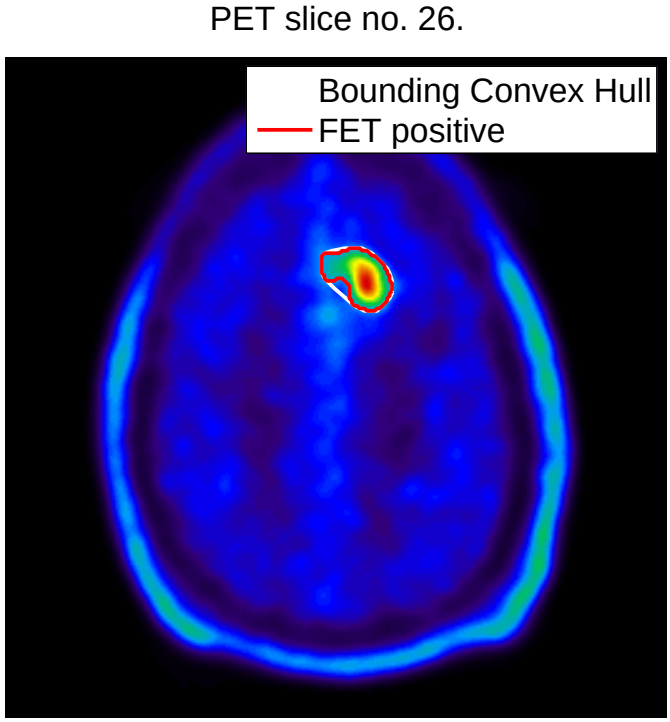

(a) Pre-treatment FET

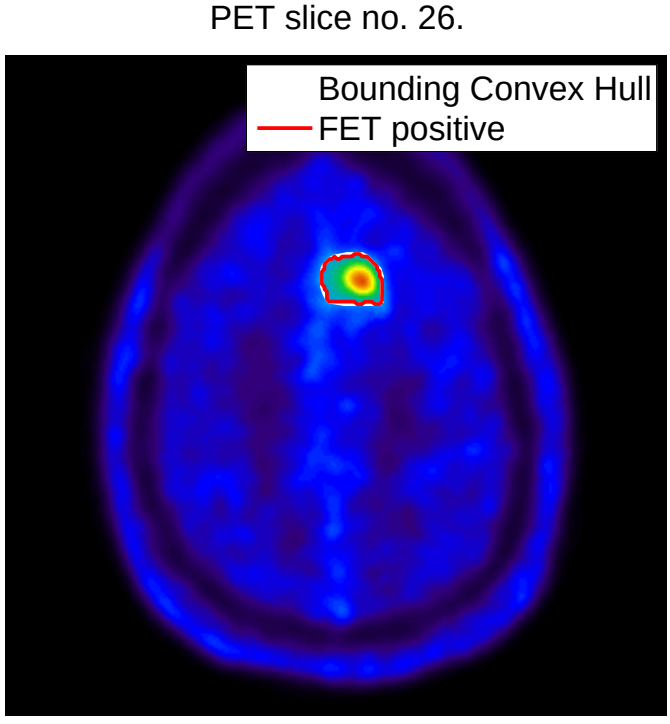

(b) Pre-treatment T1

Figure A.43: FET Scans patient 9.

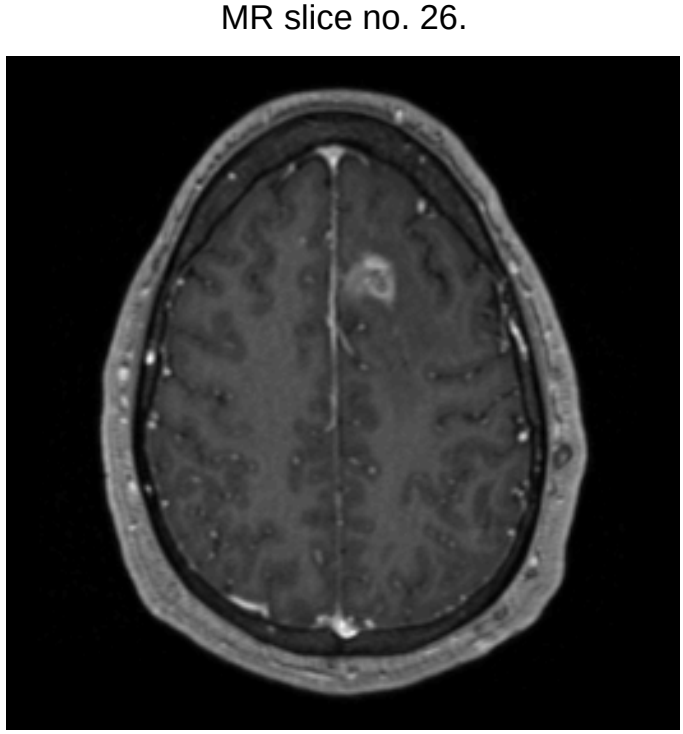

(a) Pre-treatment T1

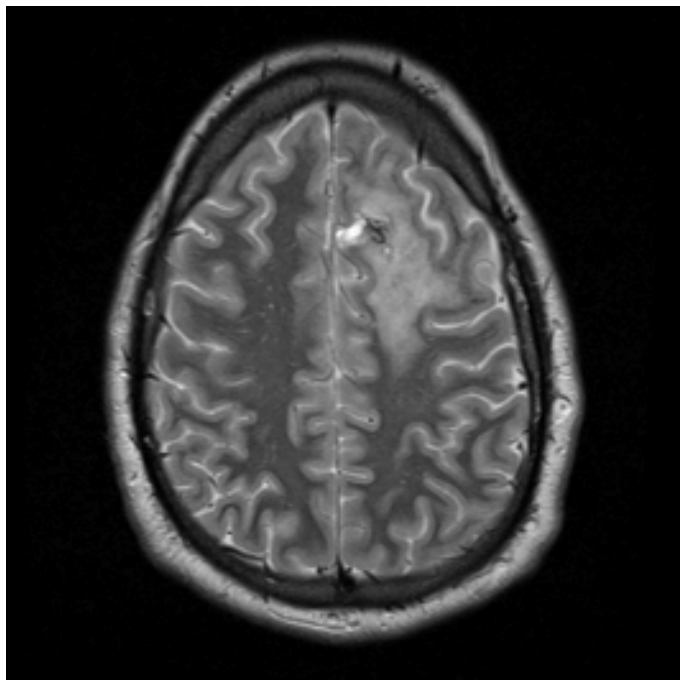

(b) Pre-treatment T2

Figure A.44: MRI patient 9.

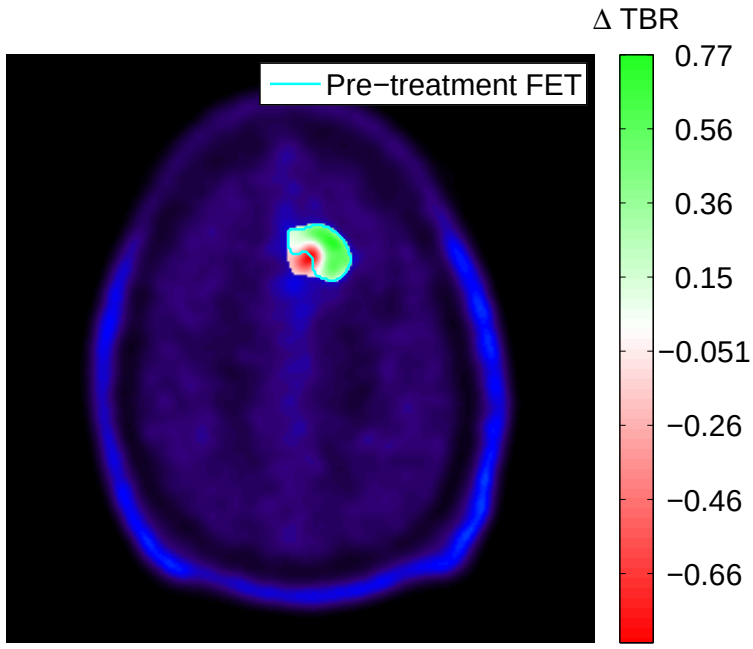

(a) Margin Map from FET volumes

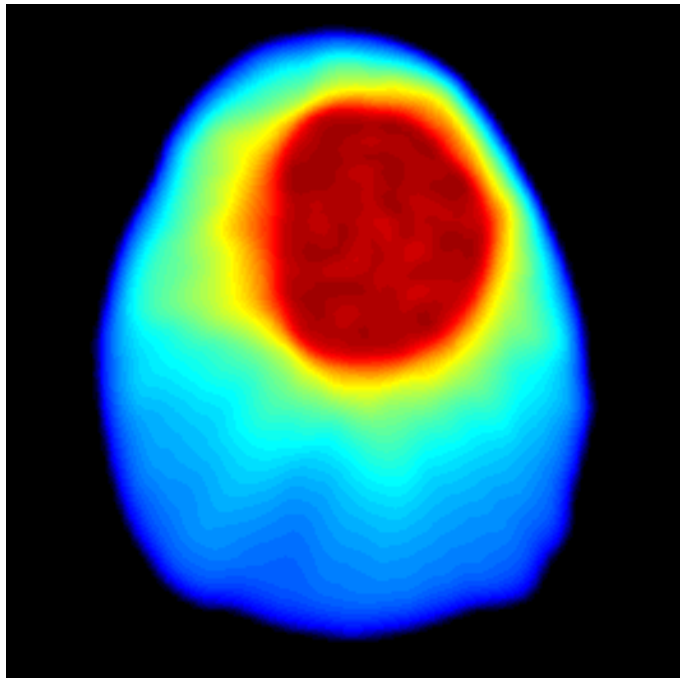

(b) Margin Map from convex hull

Figure A.45: Doseplan and response map patient 9.

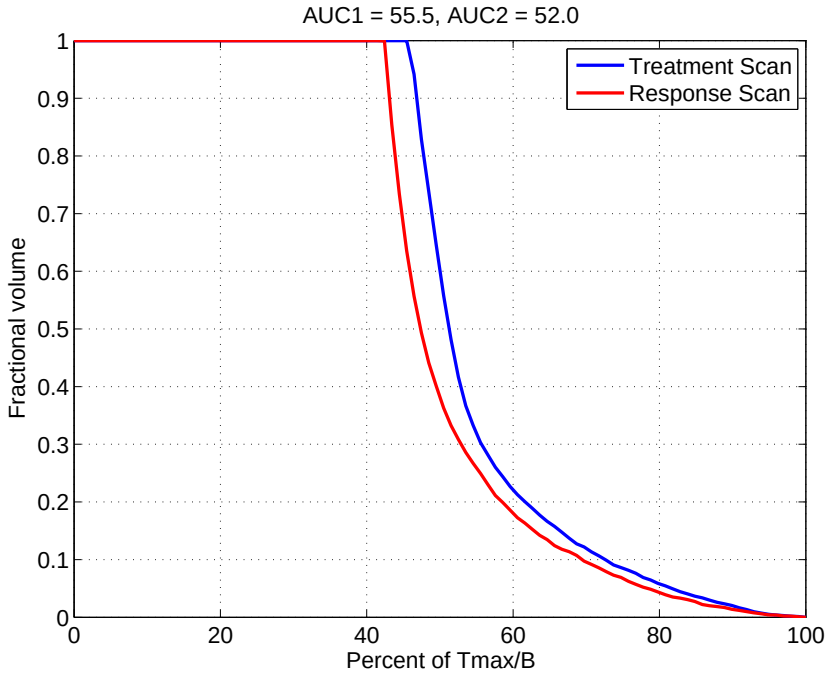

(a) Margin Map from convex hull

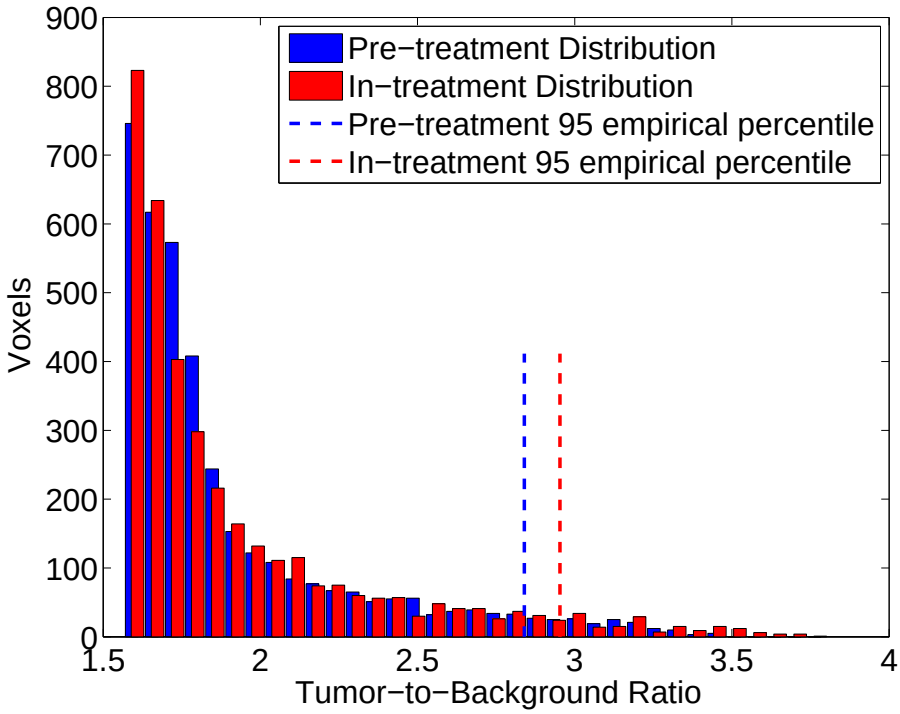

(b) Margin Map from convex hull

Figure A.46: Change in IVH and TBR distribution patient 9.

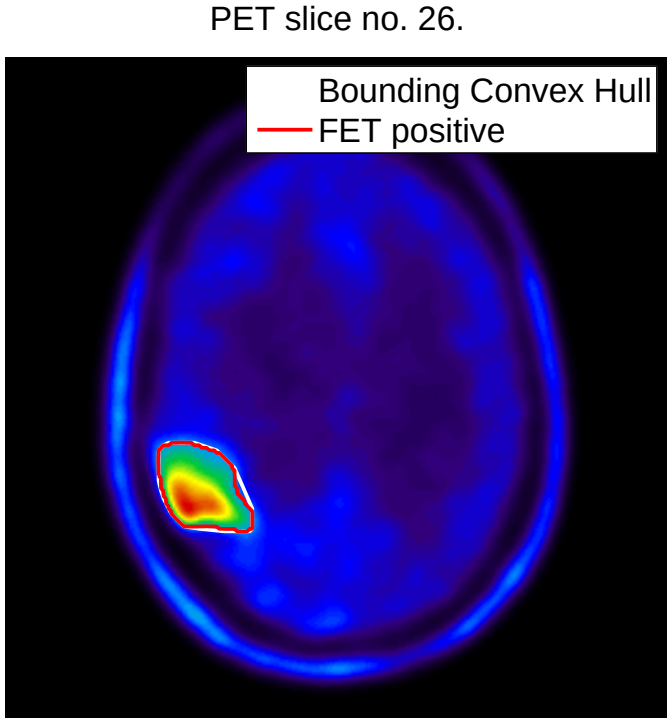

(a) Pre-treatment FET

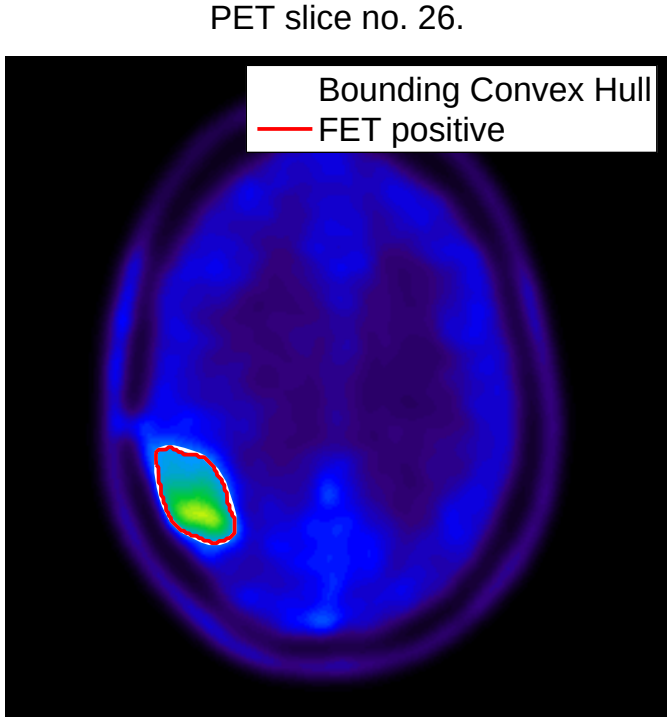

(b) Pre-treatment T1

Figure A.47: FET Scans patient 10.

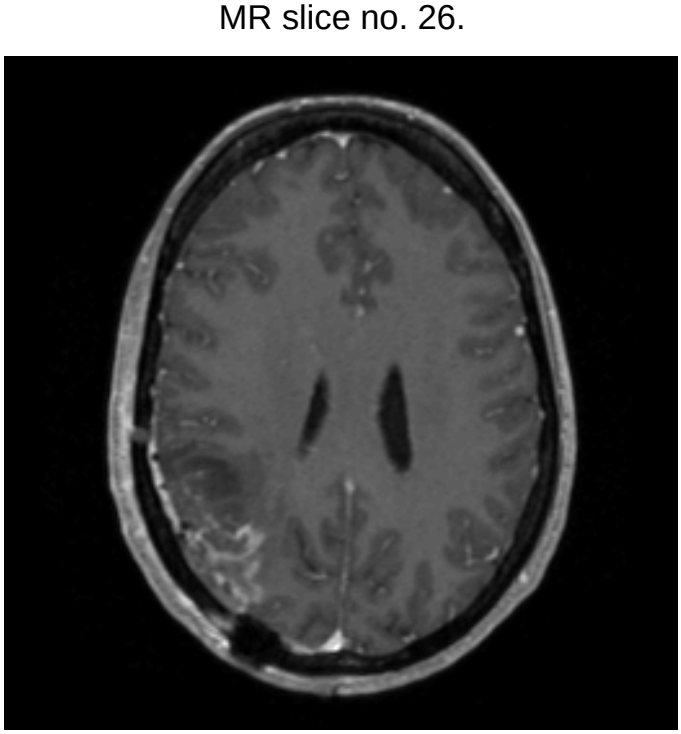

(a) Pre-treatment T1

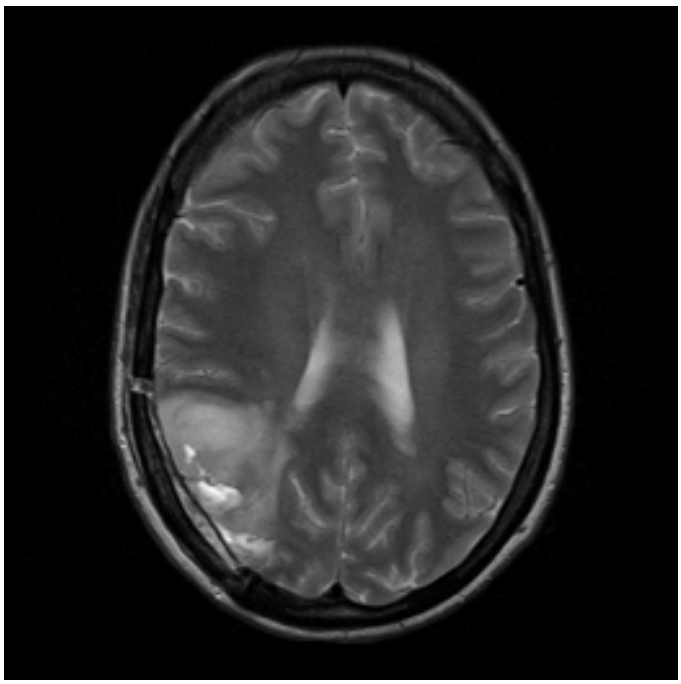

(b) Pre-treatment T2

Figure A.48: MRI patient 10.

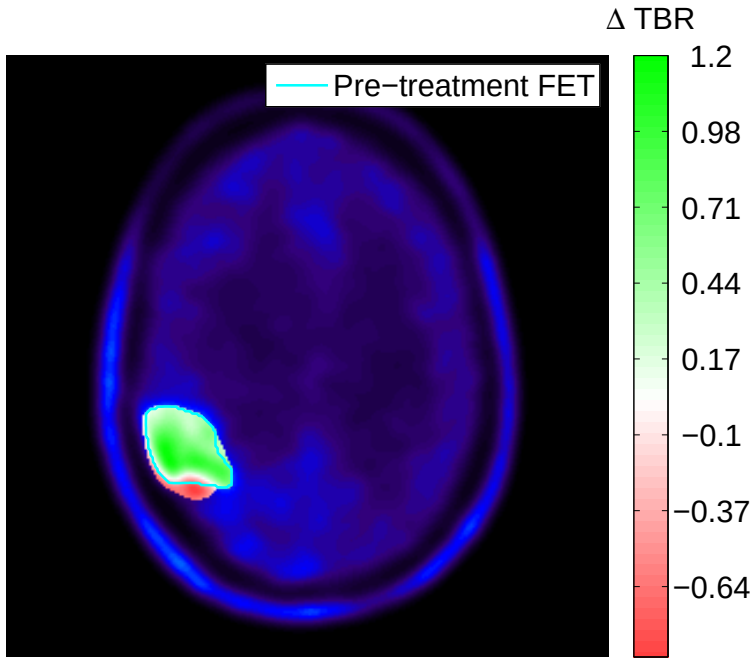

(a) Margin Map from FET volumes

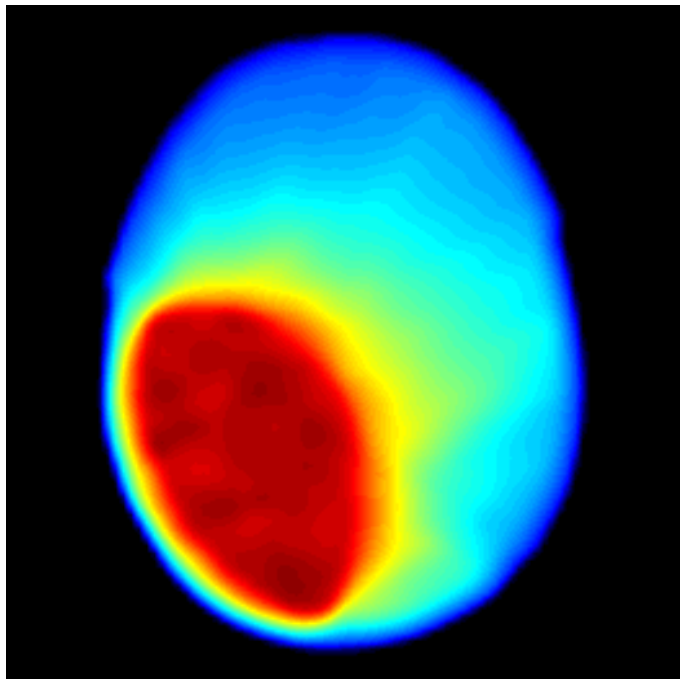

(b) Margin Map from convex hull

Figure A.49: Doseplan and response map patient 10.

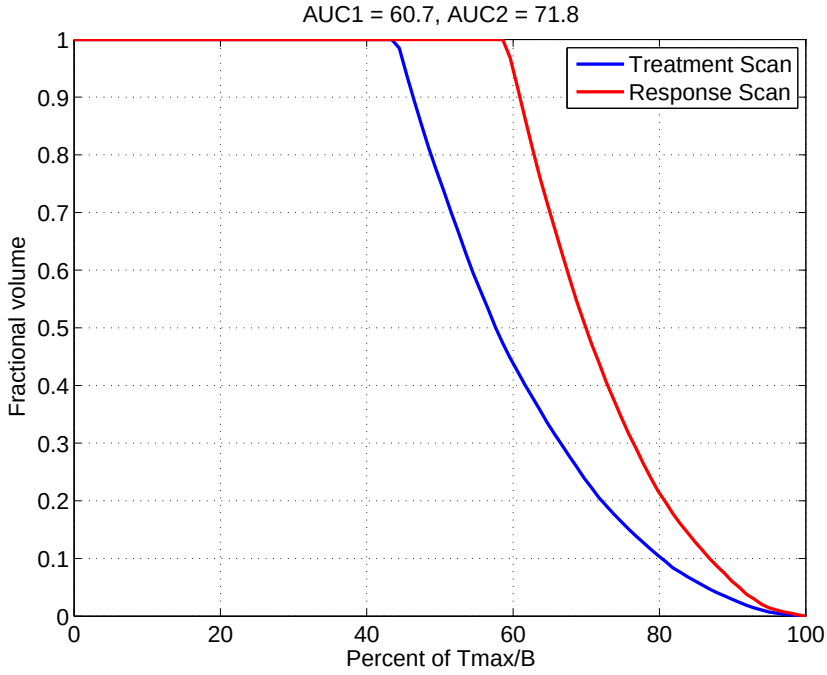

(a) Margin Map from convex hull

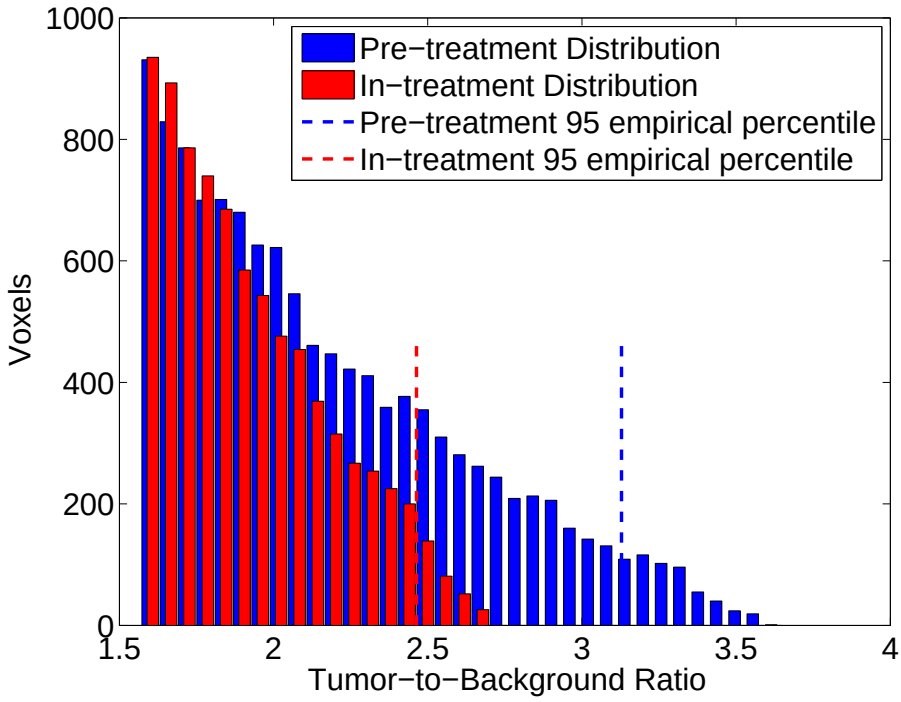

(b) Margin Map from convex hull

Figure A.50: Change in IVH and TBR distribution patient 10.

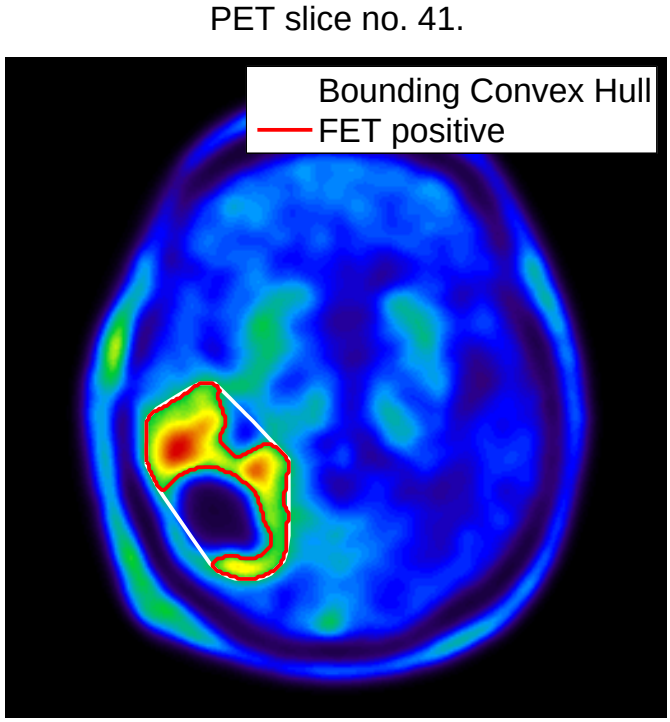

(a) Pre-treatment FET

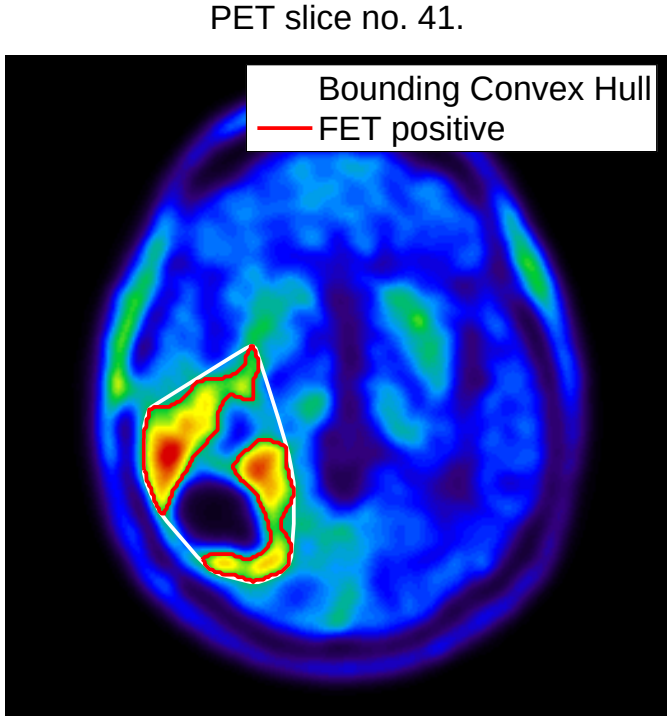

(b) Pre-treatment T1

Figure A.51: FET Scans patient 11.

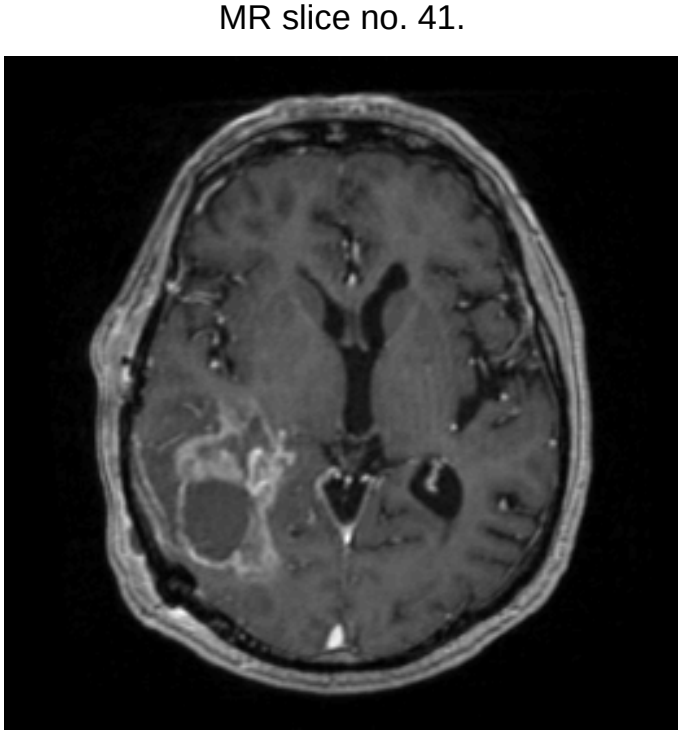

(a) Pre-treatment T1

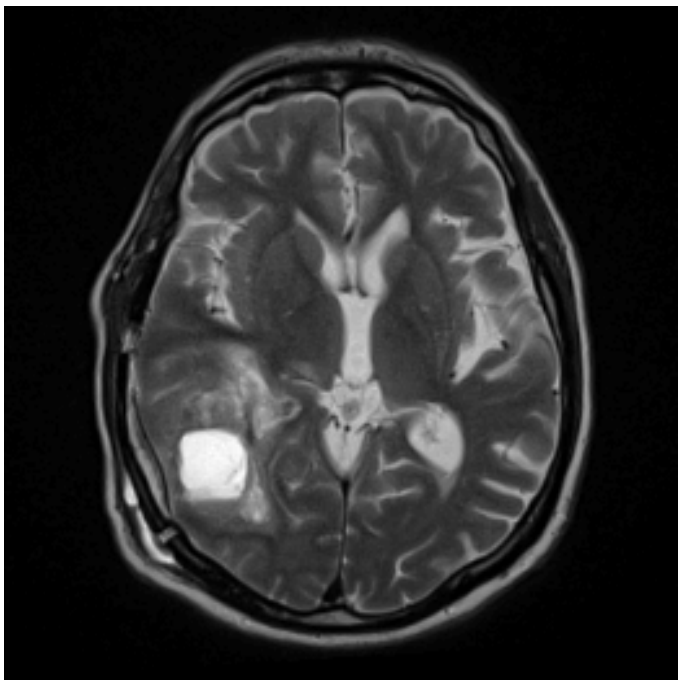

(b) Pre-treatment T2

Figure A.52: MRI patient 11.

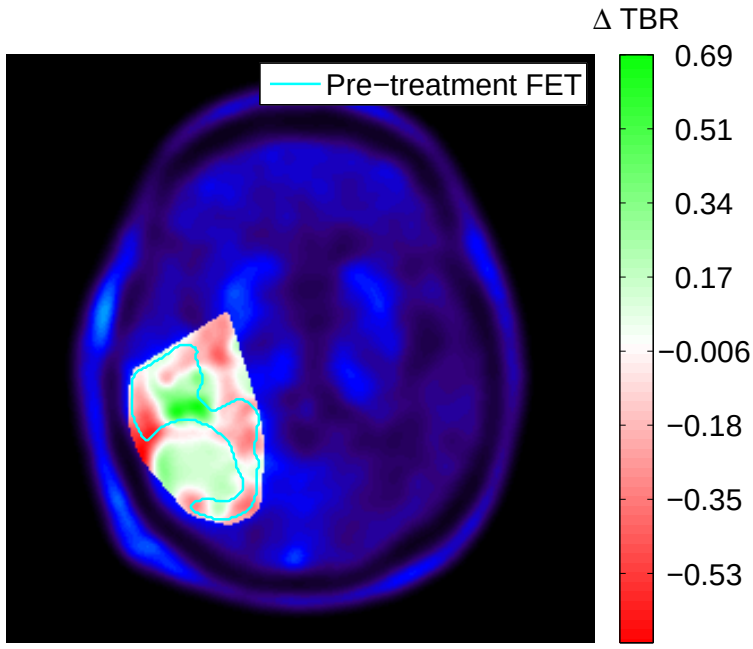

(a) Margin Map from FET volumes

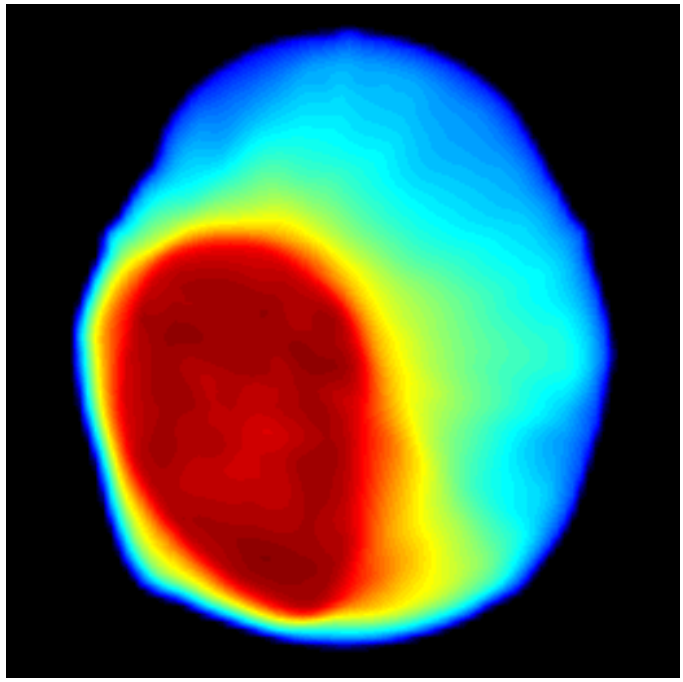

(b) Margin Map from convex hull

Figure A.53: Doseplan and response map patient 11.

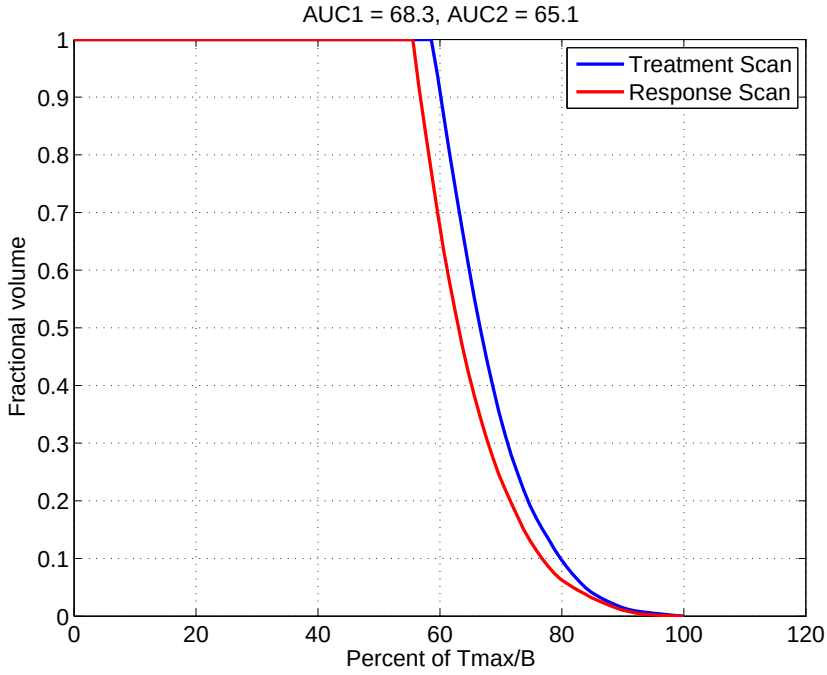

(a) Margin Map from convex hull

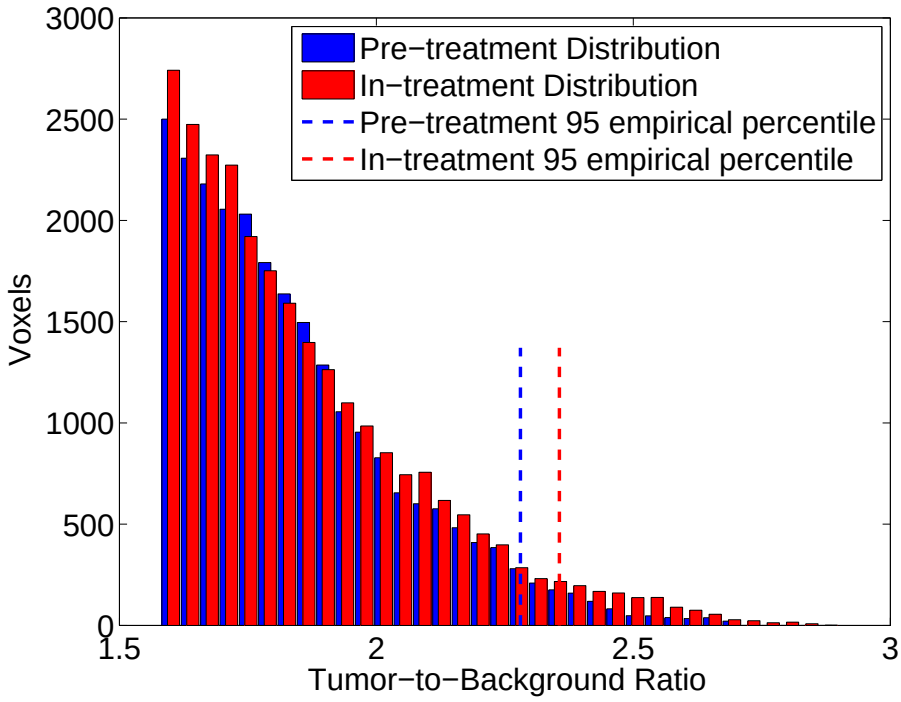

(b) Margin Map from convex hull

Figure A.54: Change in IVH and TBR distribution patient 11.

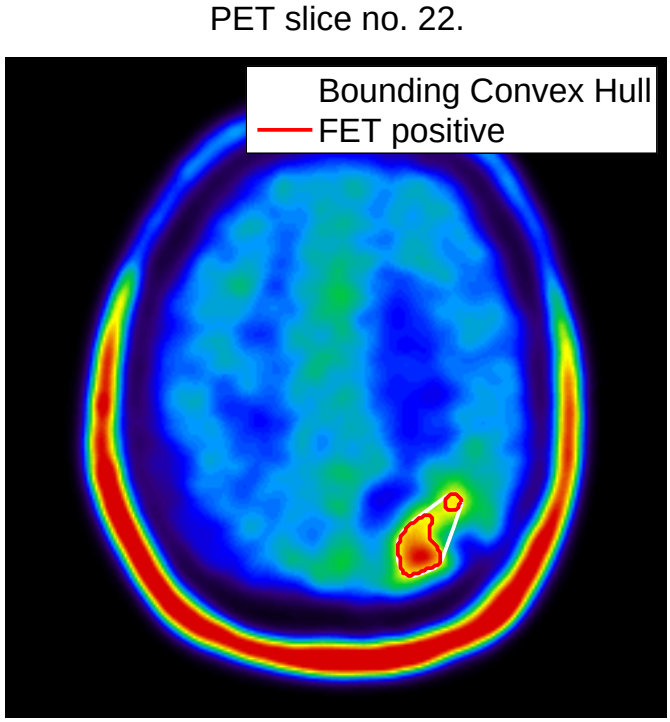

(a) Pre-treatment FET

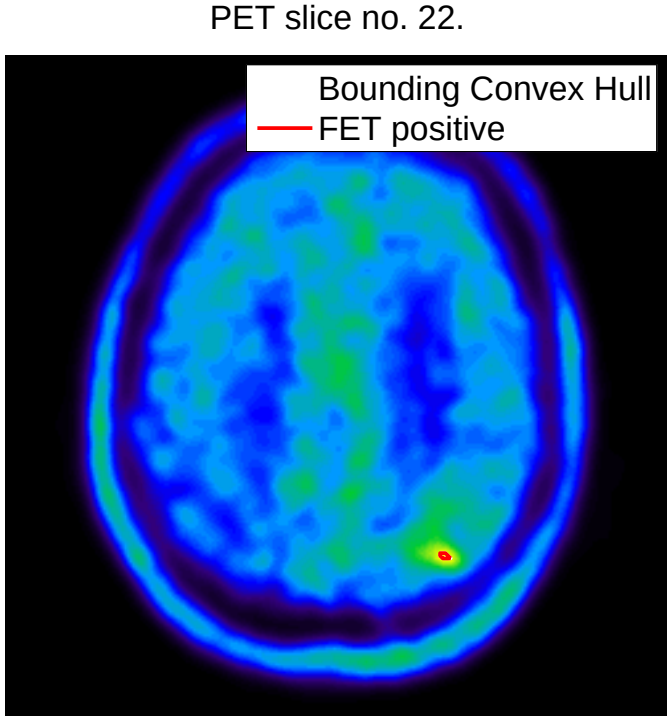

(b) Pre-treatment T1

Figure A.55: FET Scans patient 12.

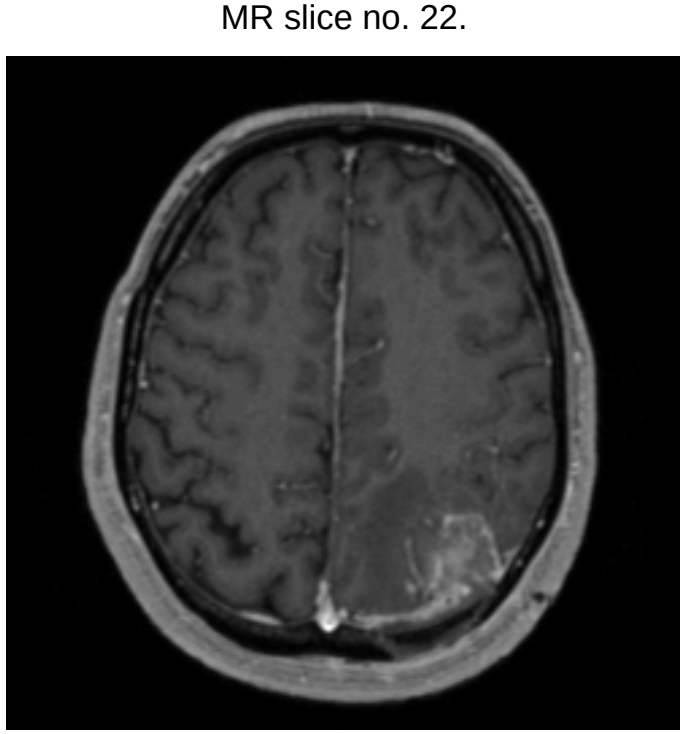

(a) Pre-treatment T1

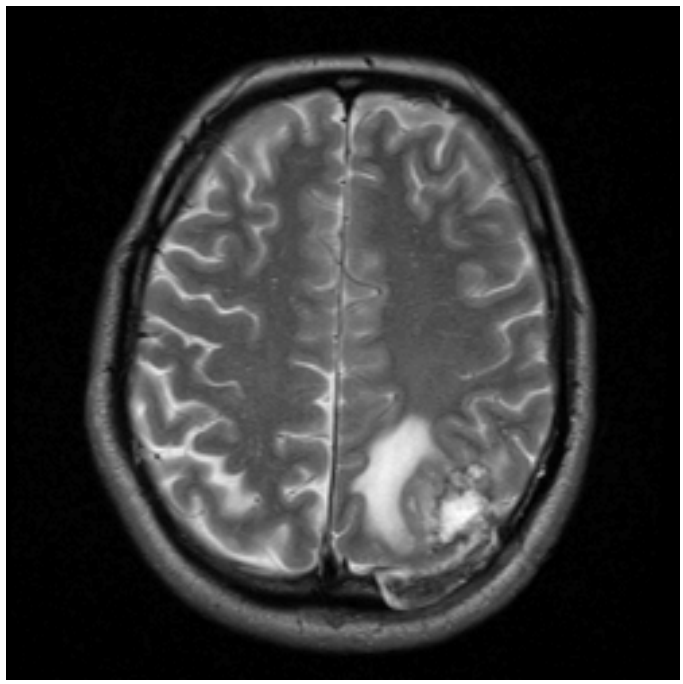

(b) Pre-treatment T2

Figure A.56: MRI patient 12.

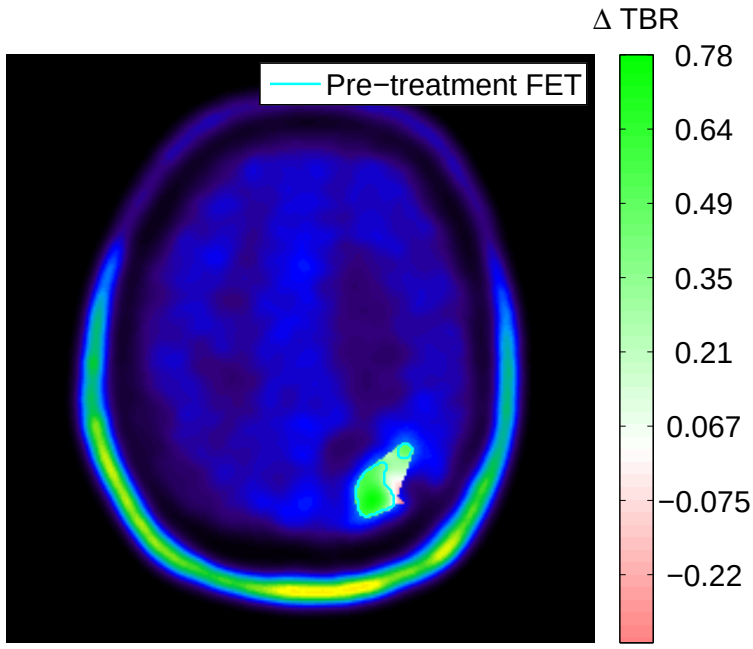

(a) Margin Map from FET volumes

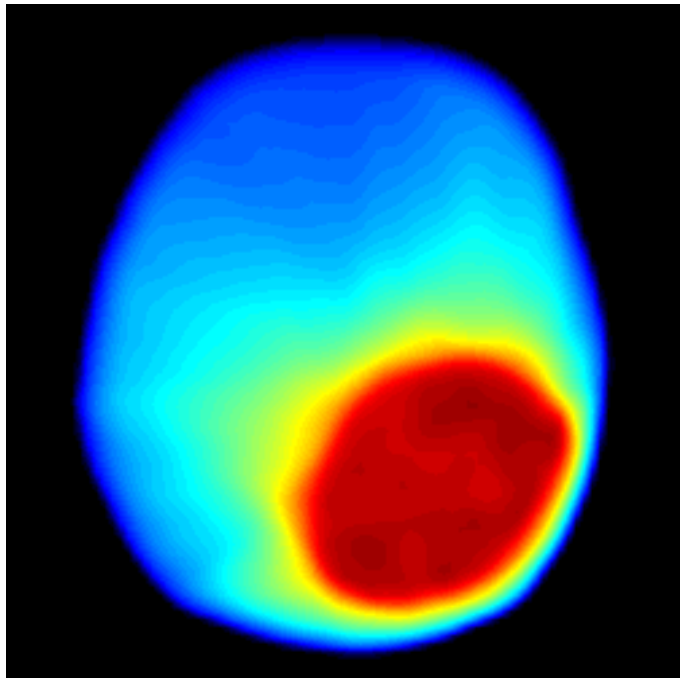

(b) Margin Map from convex hull

Figure A.57: Doseplan and response map patient 12.

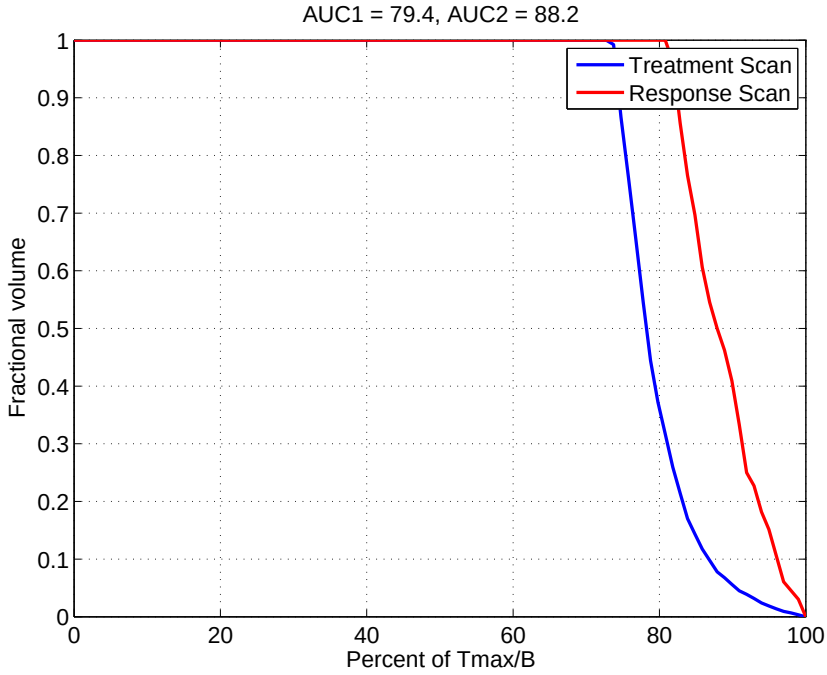

(a) Margin Map from convex hull

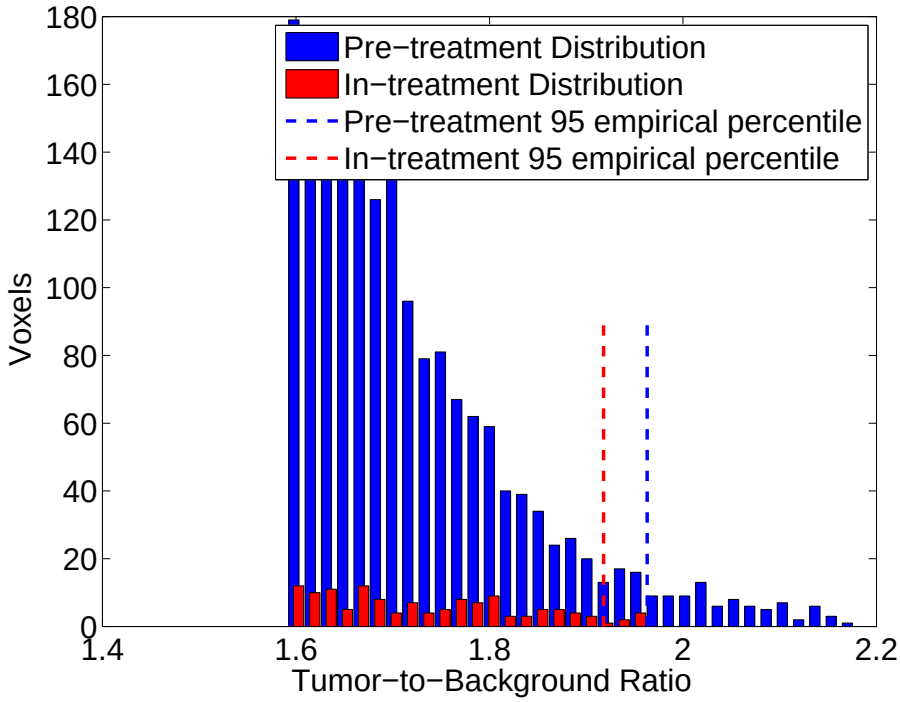

(b) Margin Map from convex hull

Figure A.58: Change in IVH and TBR distribution patient 12.

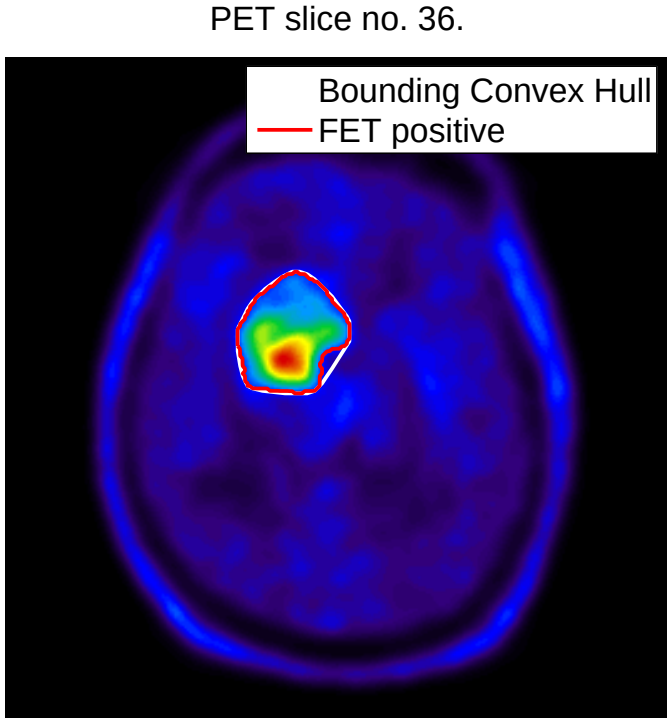

(a) Pre-treatment FET

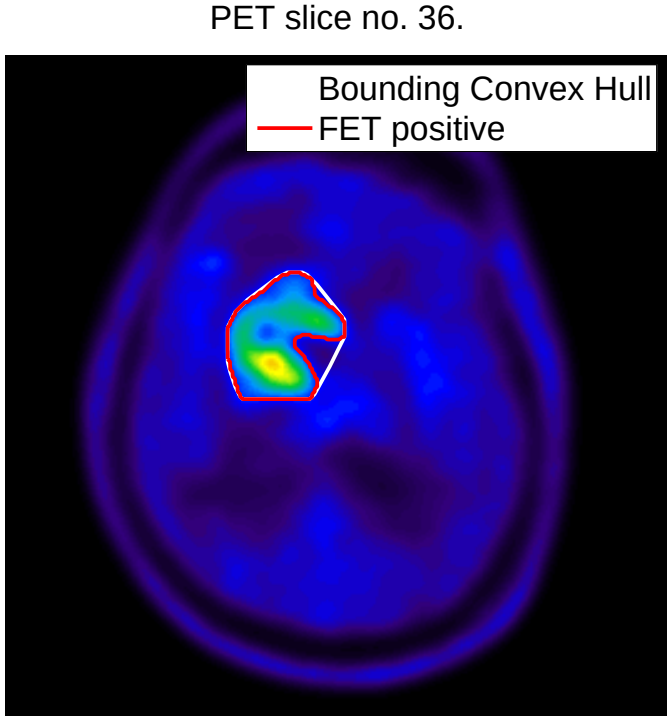

(b) Pre-treatment T1

Figure A.59: FET Scans patient 13.

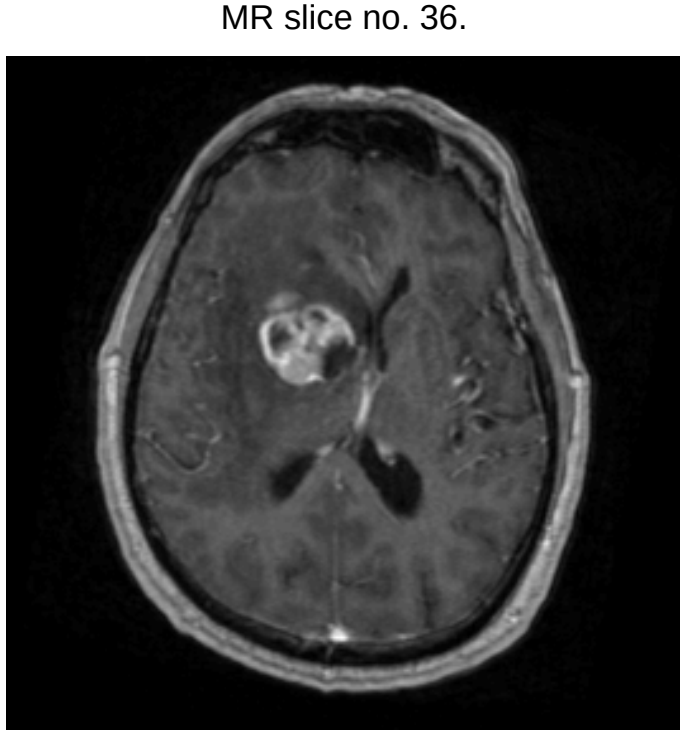

(a) Pre-treatment T1

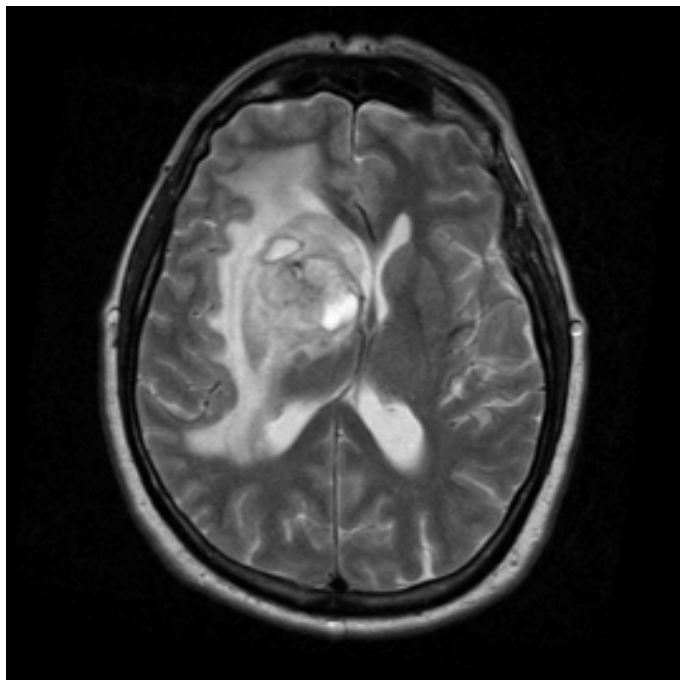

(b) Pre-treatment T2

Figure A.60: MRI patient 13.

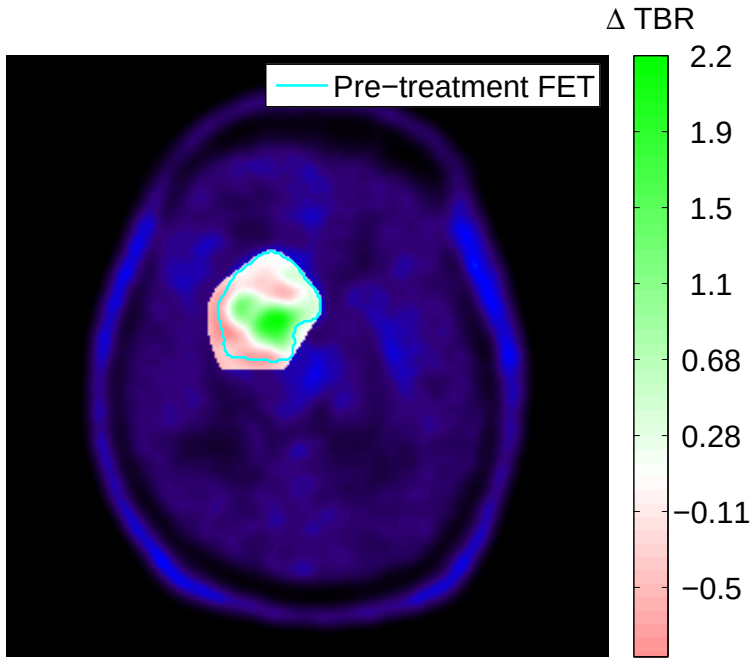

(a) Margin Map from FET volumes

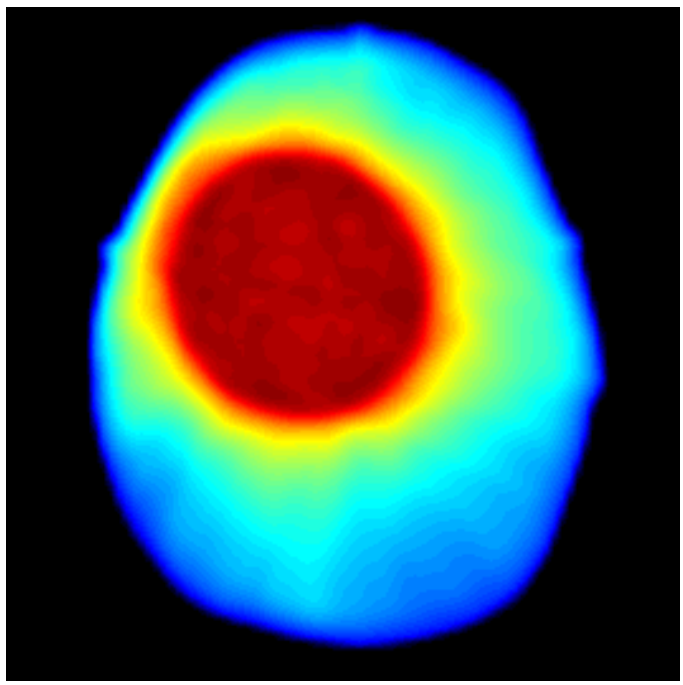

(b) Margin Map from convex hull

Figure A.61: Doseplan and response map patient 13.

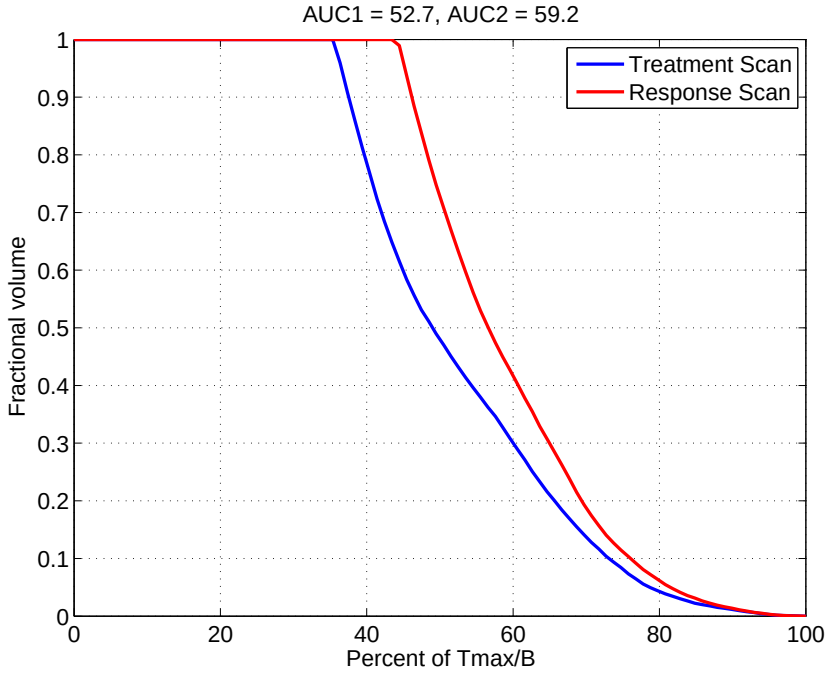

(a) Margin Map from convex hull

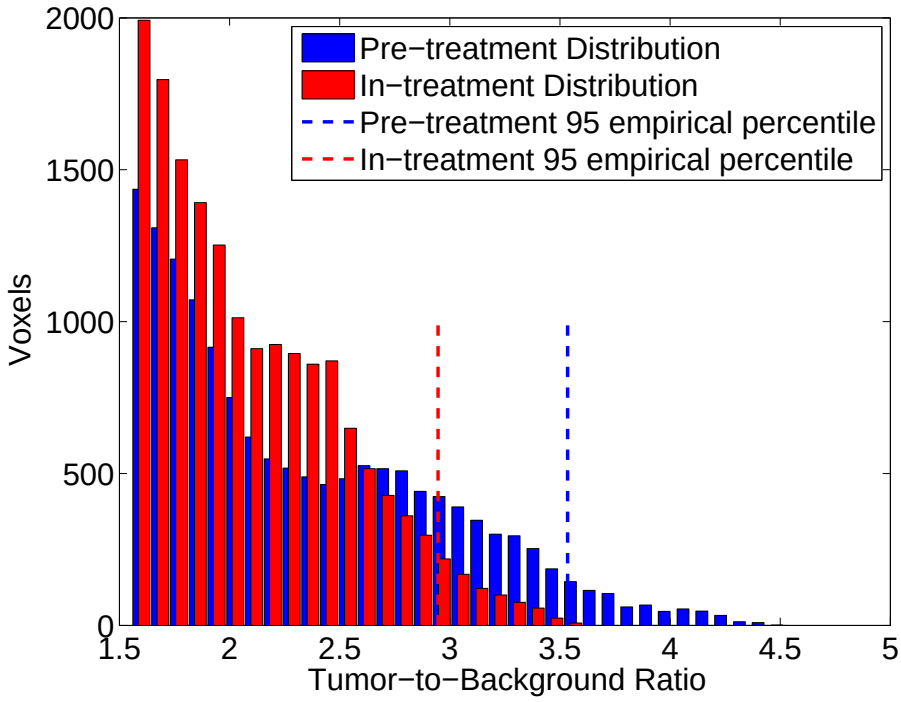

(b) Margin Map from convex hull

Figure A.62: Change in IVH and TBR distribution patient 13.

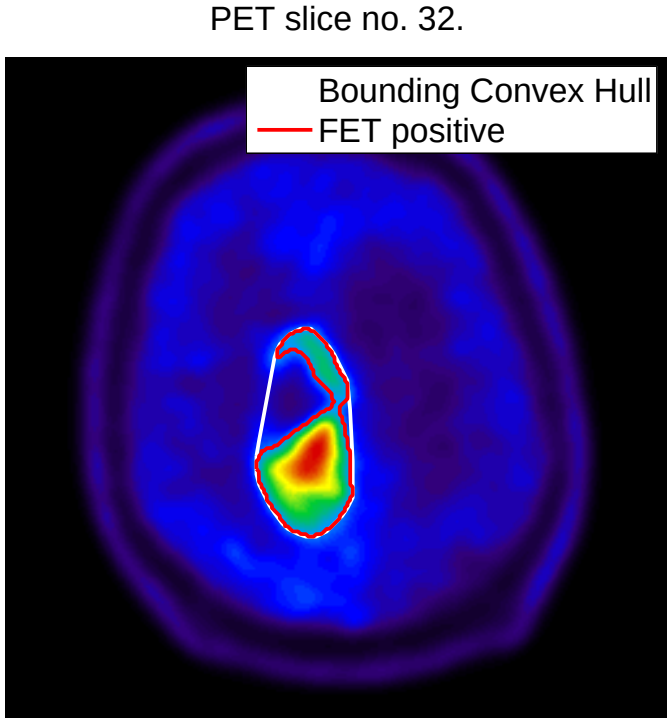

(a) Pre-treatment FET

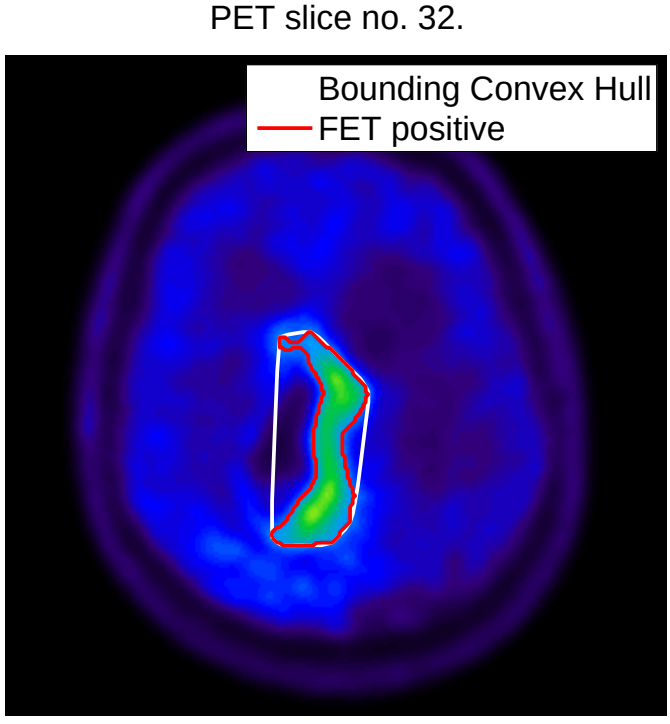

(b) Pre-treatment T1

Figure A.63: FET Scans patient 14.

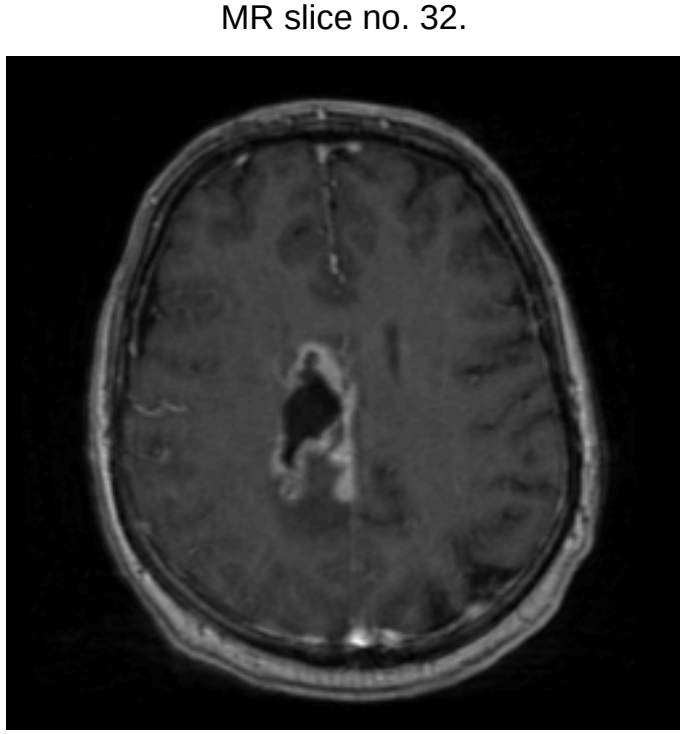

(a) Pre-treatment T1

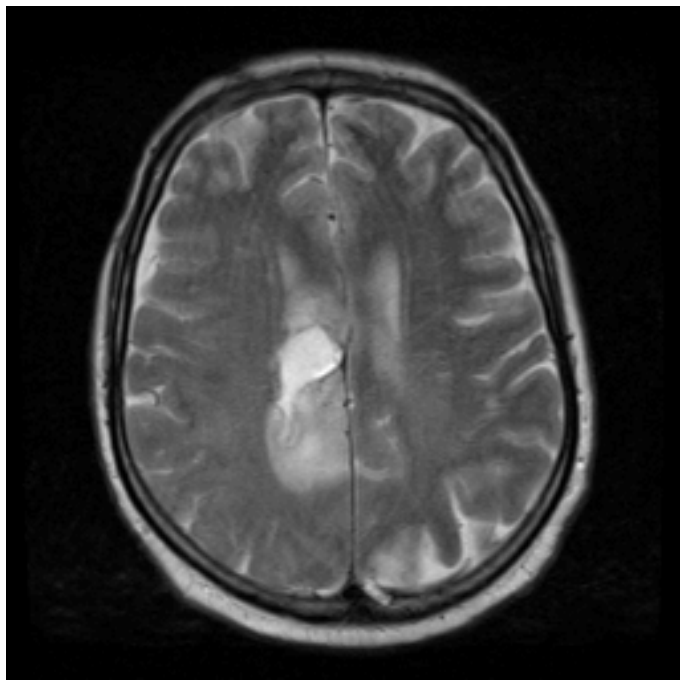

(b) Pre-treatment T2

Figure A.64: MRI patient 14.

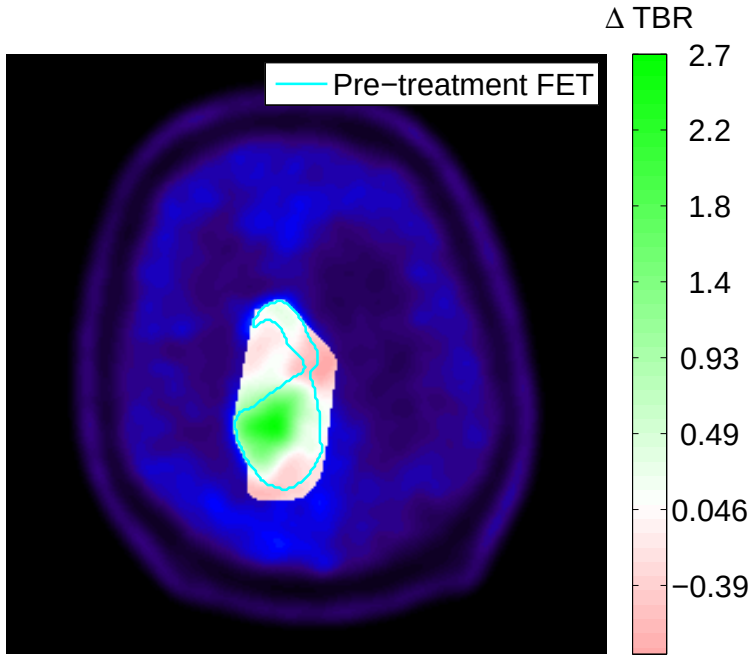

(a) Margin Map from FET volumes

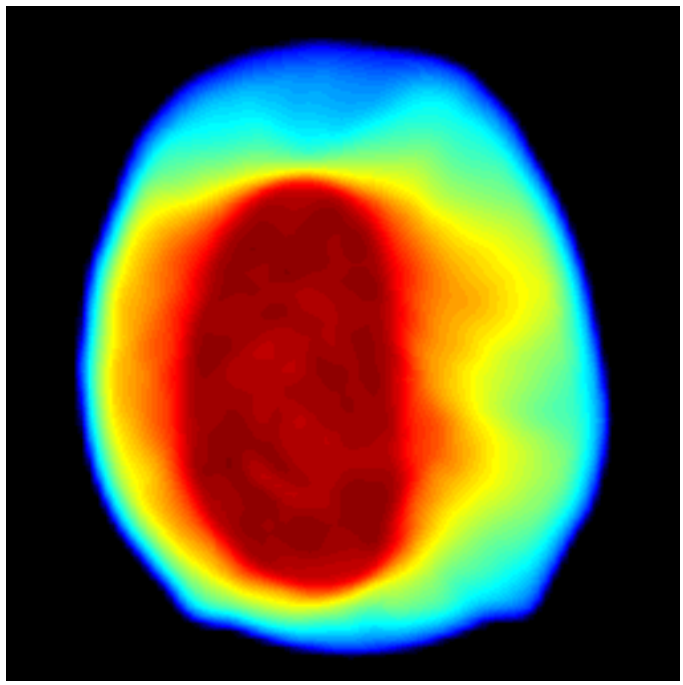

(b) Margin Map from convex hull

Figure A.65: Doseplan and response map patient 14.

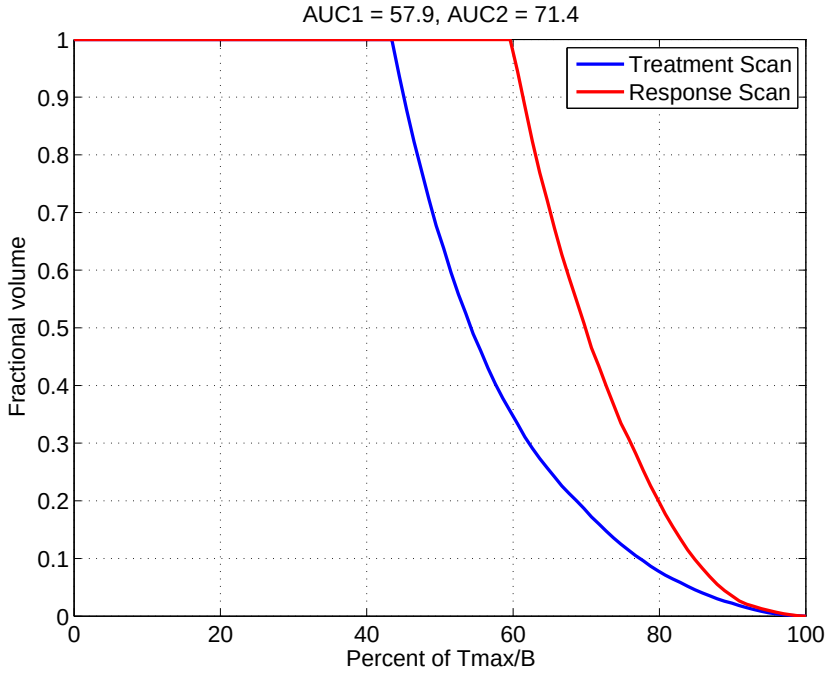

(a) Margin Map from convex hull

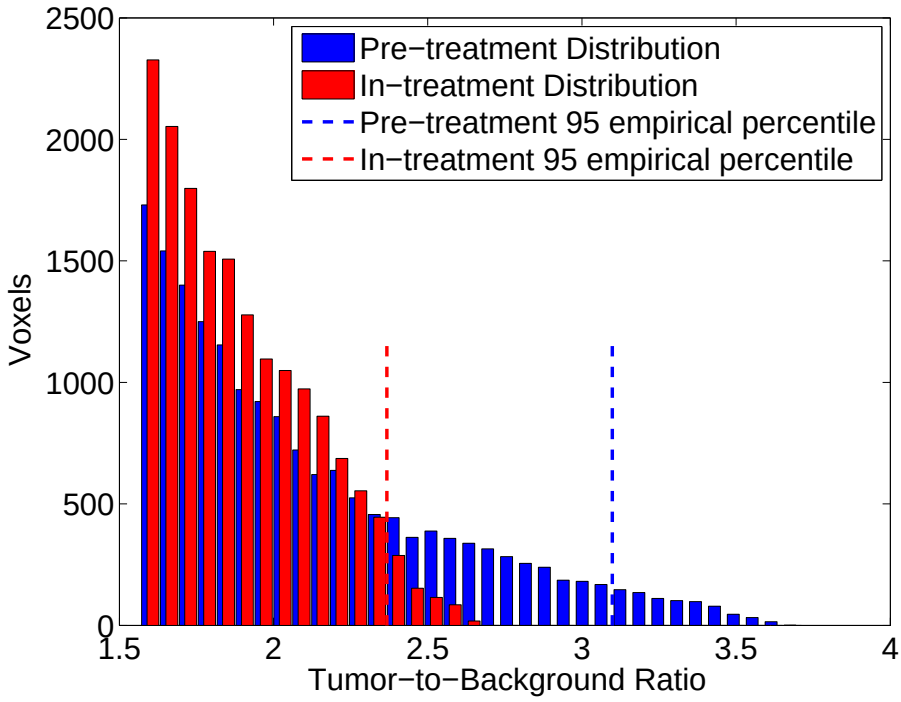

(b) Margin Map from convex hull

Figure A.66: Change in IVH and TBR distribution patient 14.

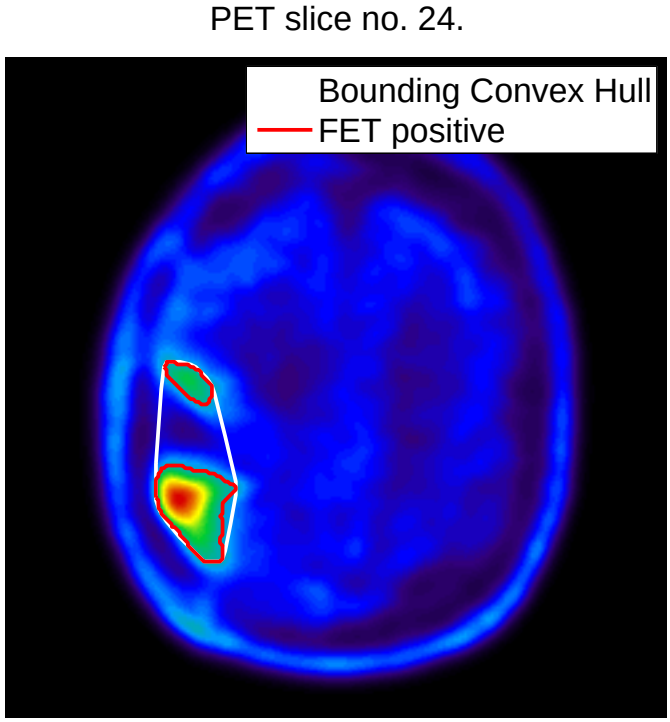

(a) Pre-treatment FET

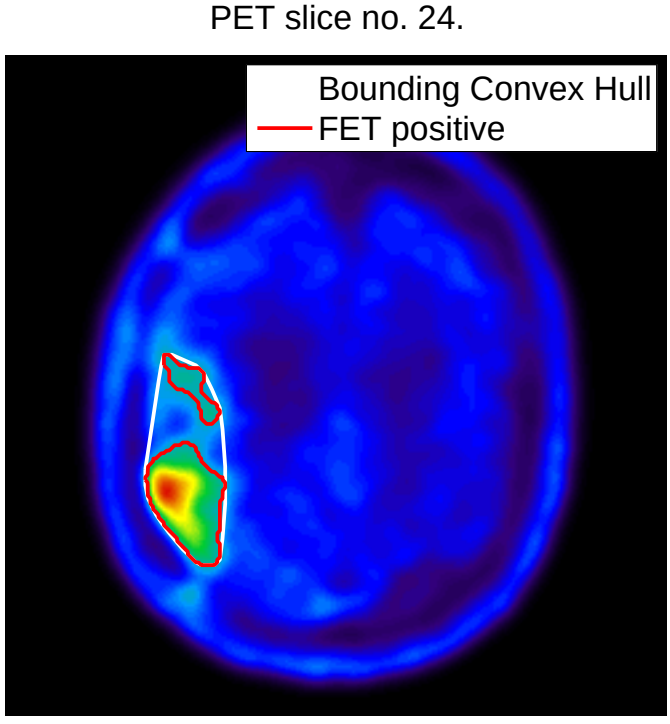

(b) Pre-treatment T1

Figure A.67: FET Scans patient 15.

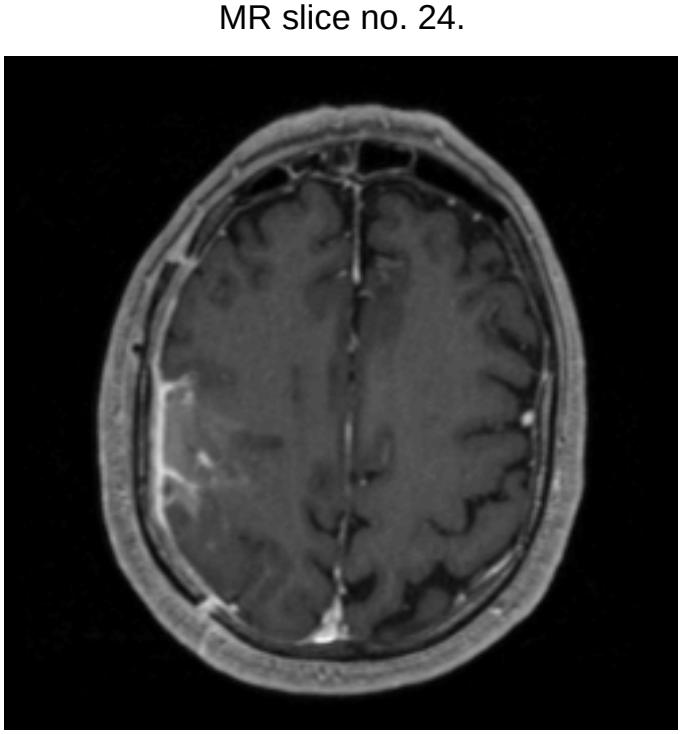

(a) Pre-treatment T1

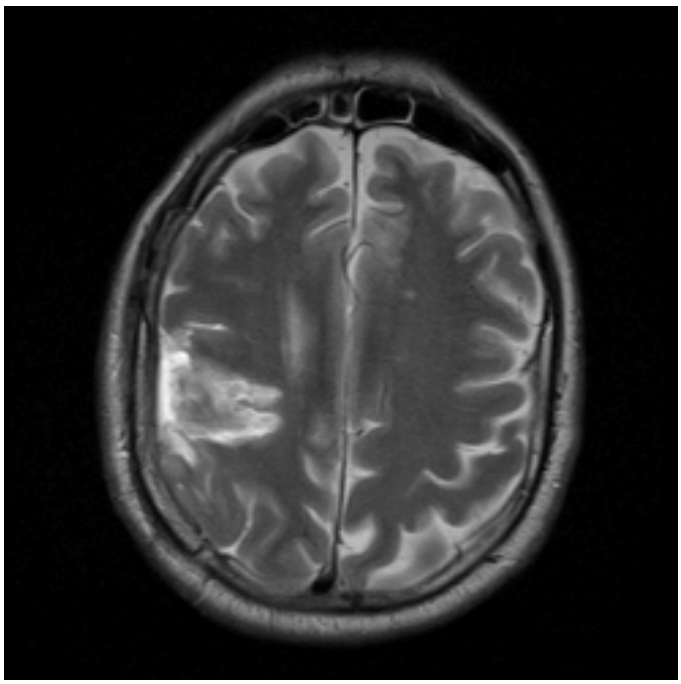

(b) Pre-treatment T2

Figure A.68: MRI patient 15.

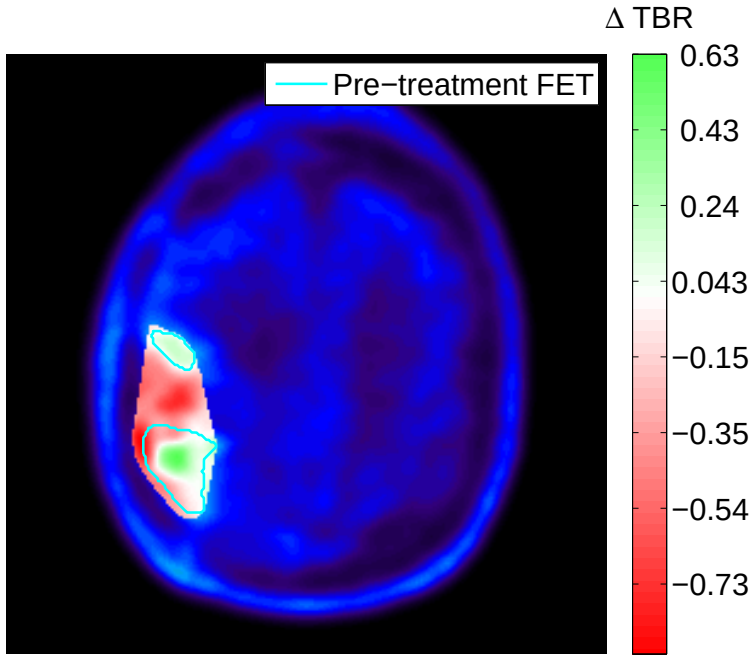

(a) Margin Map from FET volumes

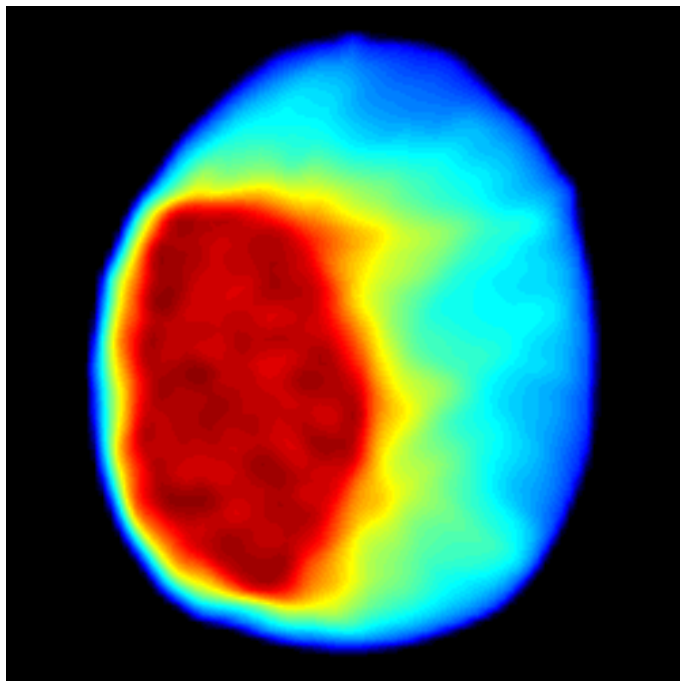

(b) Margin Map from convex hull

Figure A.69: Doseplan and response map patient 15.

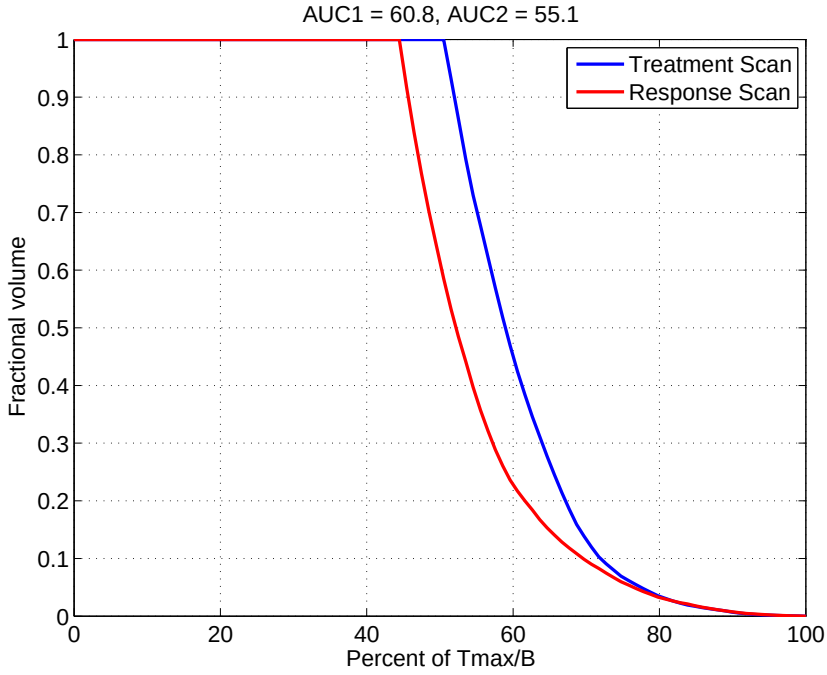

(a) Margin Map from convex hull

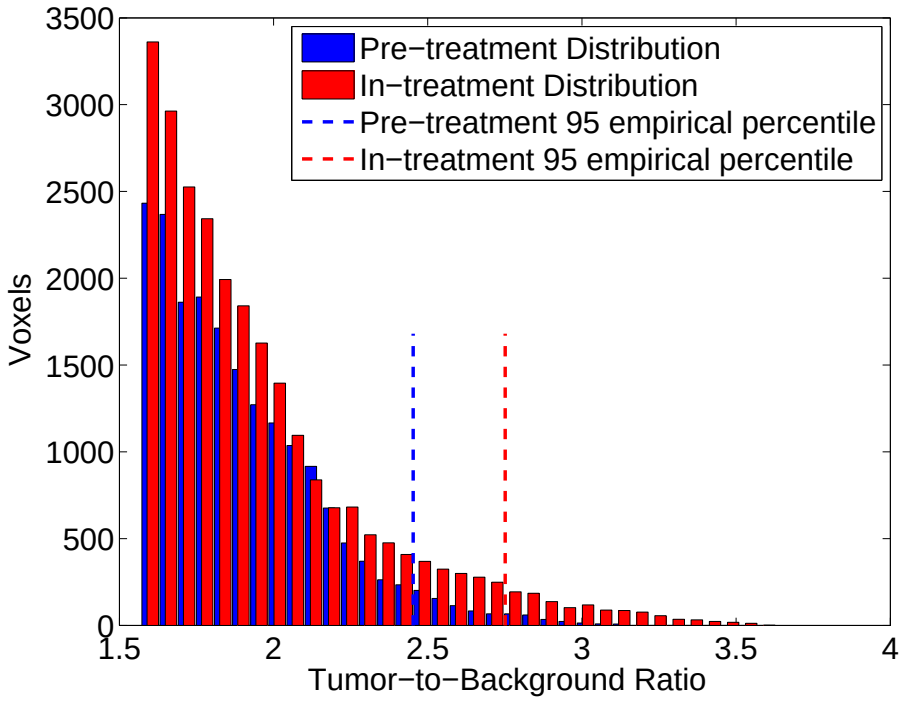

(b) Margin Map from convex hull

Figure A.70: Change in IVH and TBR distribution patient 15.

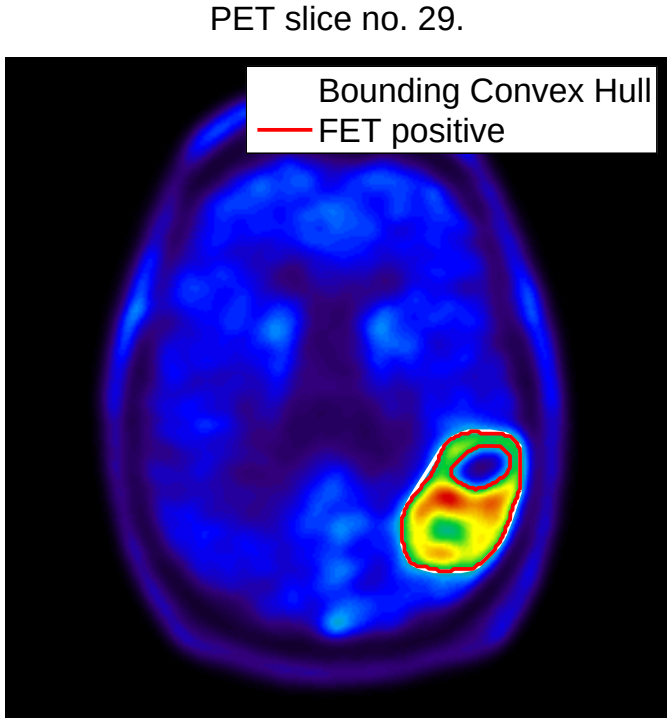

(a) Pre-treatment FET

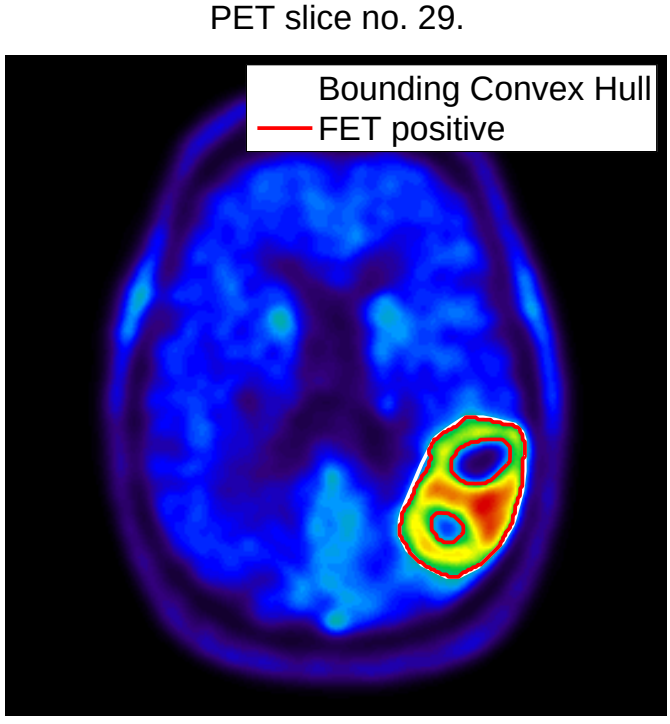

(b) Pre-treatment T1

Figure A.71: FET Scans patient 16.

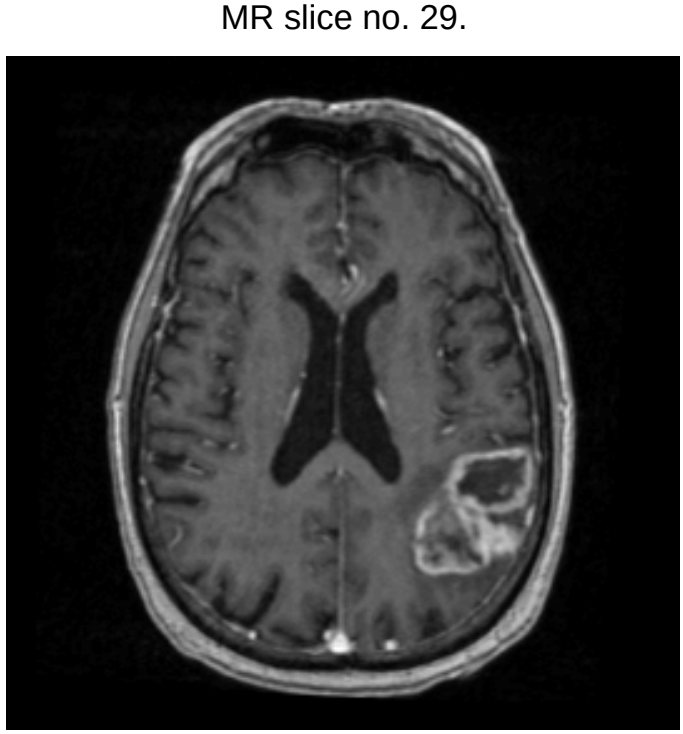

(a) Pre-treatment T1

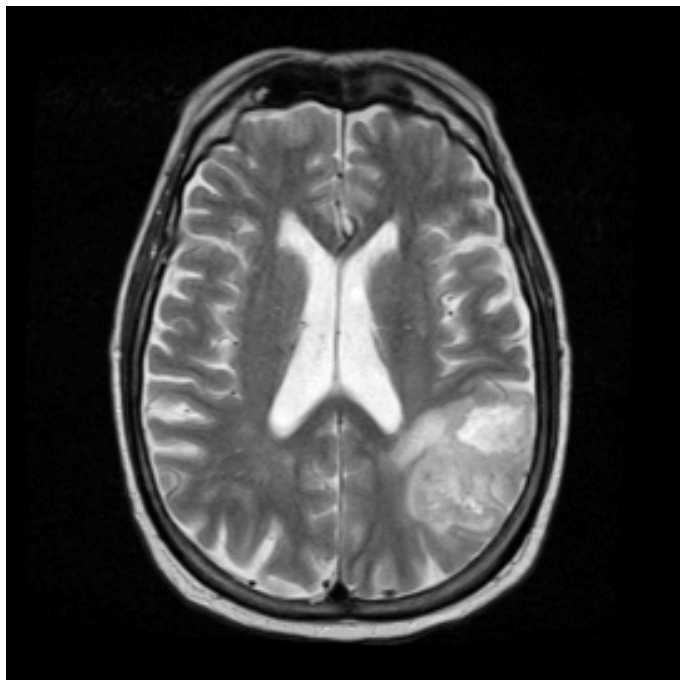

(b) Pre-treatment T2

Figure A.72: MRI patient 16.

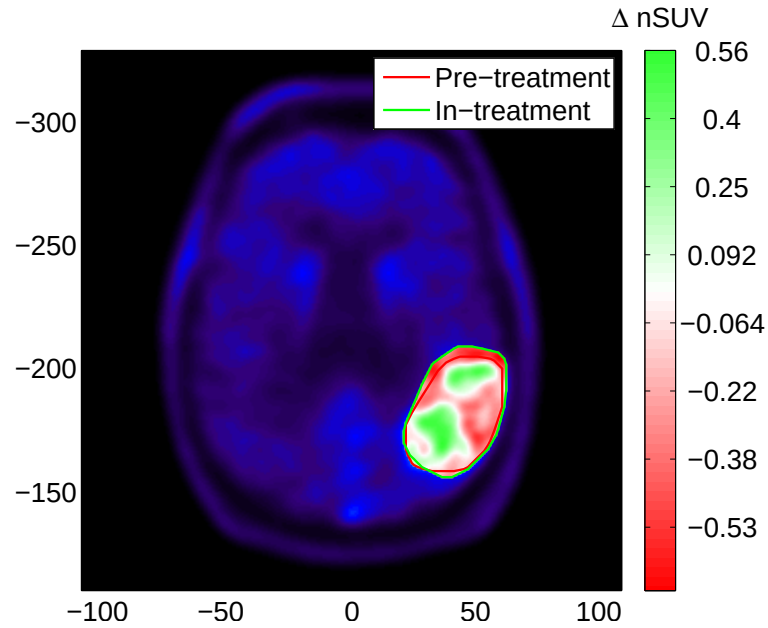

(a) Margin Map from FET volumes

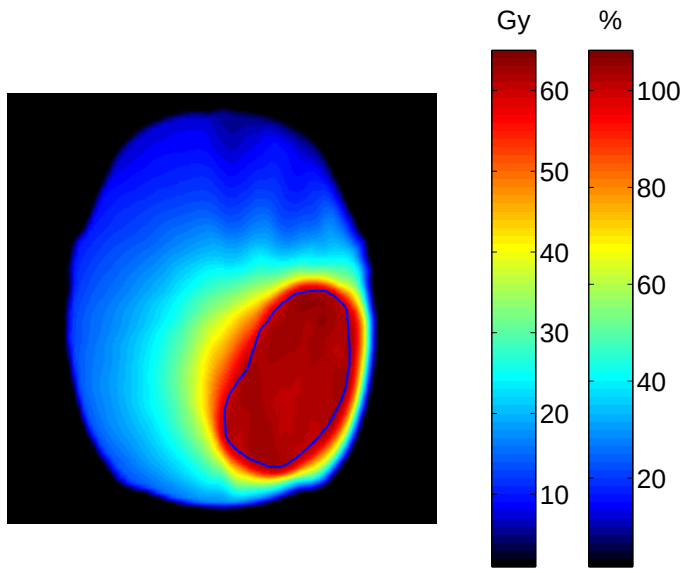

(b) Margin Map from convex hull

Figure A.73: Doseplan and response map patient 16.

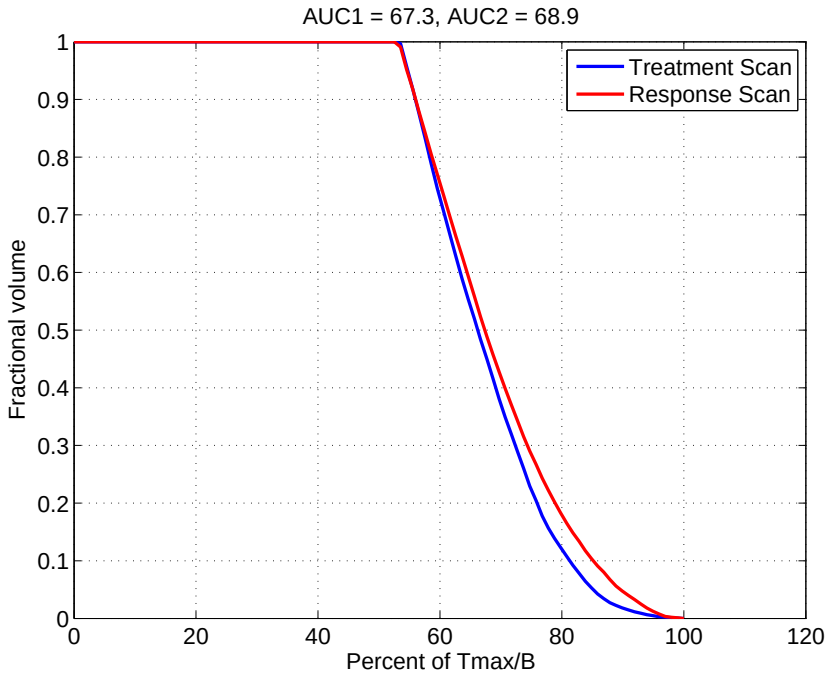

(a) Margin Map from convex hull

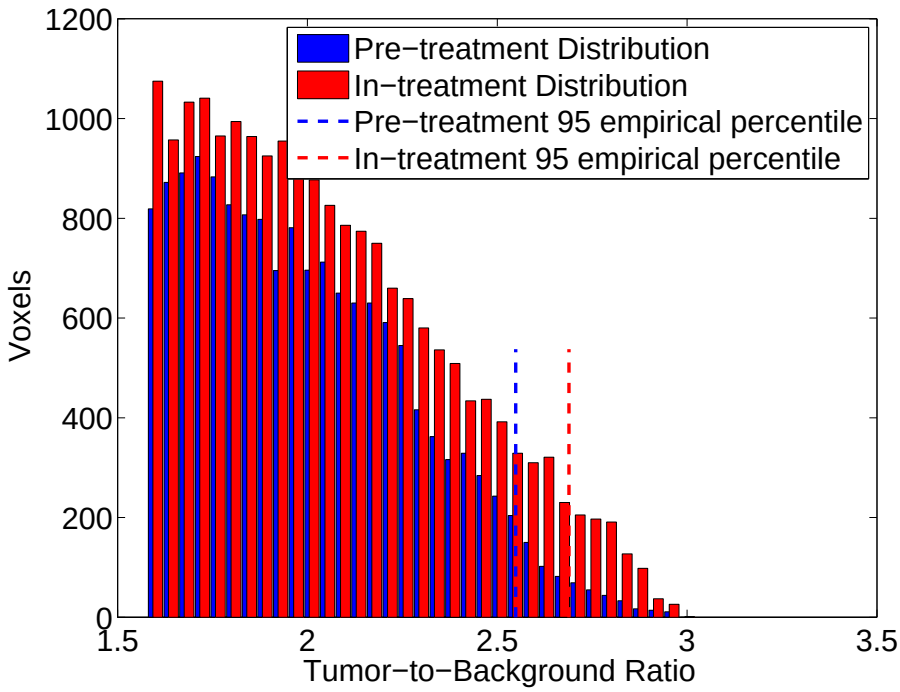

(b) Margin Map from convex hull

Figure A.74: Change in IVH and TBR distribution patient 16.

Bibliography

[1] D. N. Louis, H. Ohgaki, O. D. Wiestler, W. K. Cavenee, P. C. Burger, A. Jouvet, B. W. Scheithauer, and P. Kleihues, "The 2007 WHO classification of tumours of the central nervous system.," *Acta neuropathologica*, vol. 114, pp. 97–109, Aug. 2007.

[2] M. Preusser, S. de Ribaupierre, A. Wöhrer, S. C. Erridge, M. Hegi, M. Weller, and R. Stupp, "Current concepts and management of glioblastoma.," *Annals of neurology*, vol. 70, pp. 9–21, July 2011.

[3] C. Adamson, O. O. Kanu, A. I. Mehta, C. Di, N. Lin, A. K. Mattox, and D. D. Bigner, "Glioblastoma multiforme: a review of where we have been and where we are going.," *Expert opinion on investigational drugs*, vol. 18, pp. 1061–83, Aug. 2009.

[4] D. Pauleit, F. Floeth, H. Herzog, K. Hamacher, L. Tellmann, H.-W. Müller, H. H. Coenen, and K.-J. Langen, "Whole-body distribution and dosimetry of O-(2-[18F]fluoroethyl)-L-tyrosine.," *European journal of nuclear medicine and molecular imaging*, vol. 30, pp. 519–24, Apr. 2003.

[5] K.-J. Langen, K. Hamacher, M. Weckesser, F. Floeth, G. Stoffels, D. Bauer, H. H. Coenen, and D. Pauleit, "O-(2-[18F]fluoroethyl)-L-tyrosine: uptake mechanisms and clinical applications.," *Nuclear medicine and biology*, vol. 33, pp. 287–94, Apr. 2006.

[6] M. D. Piroth, M. Pinkawa, R. Holy, J. Klotz, S. Nussen, G. Stoffels, H. H. Coenen, H. J. Kaiser, K. J. Langen, and M. J. Eble, "Prognostic value of early [18F]fluoroethyltyrosine positron emission tomography after radiochemotherapy in glioblastoma multiforme.," *International journal of radiation oncology, biology, physics*, vol. 80, pp. 176–84, May 2011.

[7] D. Pauleit, F. Floeth, K. Hamacher, M. J. Riemenschneider, G. Reifenberger, H.-W. Müller, K. Zilles, H. H. Coenen, and K.-J. Langen, "O-(2-[18F]fluoroethyl)-L-tyrosine PET combined with MRI improves the diagnostic assessment of cerebral gliomas.," *Brain : a journal of neurology*, vol. 128, pp. 678–87, Mar. 2005.

[8] F. Tixier, C. C. Le Rest, M. Hatt, N. Albarghach, O. Pradier, J.-P. Metges, L. Corcos, and D. Visvikis, "Intratumor heterogeneity characterized by textural features on baseline 18F-FDG PET images predicts response to concomitant radiochemotherapy in esophageal cancer.," *Journal of nuclear medicine : official publication, Society of Nuclear Medicine*, vol. 52, pp. 369–78, Mar. 2011.

[9] I. El Naqa, P. Grigsby, A. Apte, E. Kidd, E. Donnelly, D. Khullar, S. Chaudhari, D. Yang, M. Schmitt, R. Laforest, W. Thorstad, and J. O. Deasy, "Exploring feature-based approaches in PET images for predicting cancer treatment outcomes.," *Pattern recognition*, vol. 42, pp. 1162–1171, June 2009.

[10] N. Galldiks and K. Langen, "Assessment of Treatment Response in Patients with Glioblastoma Using O-(2-18F-Fluoroethyl)-l-Tyrosine PET in Comparison to MRI," *Journal of Nuclear . . .*, vol. 53, no. 7, pp. 1048–1057, 2012.

[11] T. Studios, "Techpool lifeart medical illustration."

[12] R. S. T. S. P. Tate, *Anatomy and physiology.* McGraw-Hill, 7 ed., 2006.

[13] H. Poulsen, "Primære hjernetumorer hos voksne," *Strålebiologisk Laboratorium, 6321 Finsencenter, Rigshospitalet*, pp. 1–14, 2007.

[14] R. Stupp, W. P. Mason, M. J. van den Bent, M. Weller, B. Fisher, M. J. B. Taphoorn, K. Belanger, A. a. Brandes, C. Marosi, U. Bogdahn, J. Curschmann, R. C. Janzer, S. K. Ludwin, T. Gorlia, A. Allgeier, D. Lacombe, J. G. Cairncross, E. Eisenhauer, and R. O. Mirimanoff, "Radiotherapy plus concomitant and adjuvant temozolomide for glioblastoma.," *The New England journal of medicine*, vol. 352, pp. 987–96, Mar. 2005.

[15] a. Del Sole, a. Falini, L. Ravasi, L. Ottobrini, D. De Marchis, E. Bombardieri, and G. Lucignani, "Anatomical and biochemical investigation of primary brain tumours.," *European journal of nuclear medicine*, vol. 28, pp. 1851–72, Dec. 2001.

[16] H. Ohgaki and P. Kleihues, "Epidemiology and etiology of gliomas.," *Acta neuropathologica*, vol. 109, pp. 93–108, Jan. 2005.

[17] C. M. W. D. Leaver, *Principles and Practice of Radiation Therapy.* Mosby, Elsevier, 3rd ed., 2010.

[18] T. V. S. S. S. J. H. J. Aldershvile, *Basisbog i Medicin og Kirurgi*. Munksgaard, 3 ed., 2005.

[19] T. J. N. A. G. Handford, *Pathophysiology: Concepts and Application for Health Care Professionals*. McGraw-Hill, 3rd ed., 2004.

[20] J. Gomme, *Isotopteknik - Radioaktive isotoper og ioniserende stråling i biologi og medicin*. Gads Forlag, 1 ed., 1997.

[21] D. L. B. D. W. T. P. E. Valk, *Positron Emission Tomography: Basic Sciences*. Springer, 2 ed., 2005.

[22] H. Hudson and R. Larkin, "Accelerated image reconstruction using ordered subsets of projection data," *Medical Imaging, IEEE Transactions ...*, vol. 13, no. 4, pp. 601–609, 1994.

[23] J. Qi, R. Leahy, and C. Hsu, "Fully 3D Bayesian image reconstruction for the ECAT EXACT HR+," *Nuclear Science, IEEE ...*, vol. 45, no. 3, pp. 1096–1103, 1998.

[24] K. Zasadny and R. Wahl, "Standardized uptake values of normal tissues at PET with 2–fluoro-2-deoxy-D-glucose: variations with body weight and a method for correction.," *Radiology*, pp. 847–850, 1993.

[25] J. W. Keyes, "SUV: standard uptake or silly useless value?," *Journal of nuclear medicine : official publication, Society of Nuclear Medicine*, vol. 36, pp. 1836–9, Oct. 1995.

[26] M. C. Adams, T. G. Turkington, J. M. Wilson, and T. Z. Wong, "A systematic review of the factors affecting accuracy of SUV measurements.," *AJR. American journal of roentgenology*, vol. 195, pp. 310–20, Aug. 2010.

[27] W. Weber, H. Wester, and A. Grosu, "O-(2- fluoroethyl)-L-tyrosine and L- methionine uptake in brain tumours: initial results of a comparative study," *European Journal of ...*, vol. 27, no. 5, 2000.

[28] T. Ogawa, F. Shishido, and I. Kanno, "Cerebral glioma: evaluation with methionine PET.," *Radiology*, no. 186, pp. 45–53, 1993.

[29] R. Haubner, "PET radiopharmaceuticals in radiation treatment planning - synthesis and biological characteristics.," *Radiotherapy and oncology : journal of the European Society for Therapeutic Radiology and Oncology*, vol. 96, pp. 280–7, Sept. 2010.

[30] K.-j. Langen, K. Ziemons, C. W. Kiwit, H. Herzog, T. Kuwert, W. J. Bock, G. Stã, L. E. Feinendegen, and H.-w. Mãller-g a, "3-[123I]iodo-alpha-methyltyrosine and [methyl-11C]-L-methionine uptake in cerebral gliomas: a comparative study using SPECT and PET.," *Journal of Nuclear Medicine*, no. 19, pp. 517–522, 1997.

[31] P. Jager and W. Vaalburg, "Radiolabeled Amino Acids: Basic Aspects and Clinical Applications in Oncology*," *Journal of Nuclear . . .*, vol. 42, no. 3, pp. 432–445, 2001.

[32] B. N. L. National Nuclear Data Center, "Nuclear structure and decay data," August 2012.

[33] H. Wester, M. Herz, and W. Weber, "Synthesis and radiopharmacology of O-(2- fluoroethyl)-L-tyrosine for tumor imaging.," *Journal of nuclear . . .*, pp. 205–212, 1999.

[34] K. Hamacher and H. H. Coenen, "Efficient routine production of the 18F-labelled amino acid O-2-18F fluoroethyl-L-tyrosine.," *Applied radiation and isotopes : including data, instrumentation and methods for use in agriculture, industry and medicine*, vol. 57, pp. 853–6, Dec. 2002.

[35] B. Stöber, U. Tanase, M. Herz, C. Seidl, M. Schwaiger, and R. Senekowitsch-Schmidtke, "Differentiation of tumour and inflammation: characterisation of [methyl-3H]methionine (MET) and O-(2-[18F]fluoroethyl)-L-tyrosine (FET) uptake in human tumour and inflammatory cells.," *European journal of nuclear medicine and molecular imaging*, vol. 33, pp. 932–9, Aug. 2006.

[36] G. Pöpperl, F. W. Kreth, J. H. Mehrkens, J. Herms, K. Seelos, W. Koch, F. J. Gildehaus, H. a. Kretzschmar, J. C. Tonn, and K. Tatsch, "FET PET for the evaluation of untreated gliomas: correlation of FET uptake and uptake kinetics with tumour grading.," *European journal of nuclear medicine and molecular imaging*, vol. 34, pp. 1933–42, Dec. 2007.

[37] J. J. M. B. Jerrold T. Bushberg J. Anthony Seibert Edwin M. Leidholdt, *The Essential Physics of Medical Imaging*. Lippincott Williams & Wilkins, 2nd ed., 2002.

[38] S. R. C. M. Dahlbom, *PET: Physics, Instrumentation and Scanners*. Springer, 2006.

[39] M. Levitt, *Spin Dynamics - Basics of Nuclear Magnetic Resonance*. Wiley, 2 ed., 2001.

[40] D. G. Nishimura, *Principles of Magnetic Resonance Imaging*. Stanford, , CA: Stanford University, 2010.

[41] K. V. L. R. Larsen, *Medical Image Analysis*. IMM DTU, 2011.

[42] M. V. Christensen, *Image Registration and Optimization in the Virtual Slaugtherhouse*. PhD thesis, Technical University of Denmark, 2008.

[43] R. Stupp, M. E. Hegi, W. P. Mason, M. J. van den Bent, M. J. B. Taphoorn, R. C. Janzer, S. K. Ludwin, A. Allgeier, B. Fisher, K. Belanger, P. Hau, A. a. Brandes, J. Gijtenbeek, C. Marosi, C. J. Vecht, K. Mokhtari, P. Wesseling, S. Villa, E. Eisenhauer, T. Gorlia, M. Weller, D. Lacombe, J. G. Cairncross, and R.-O. Mirimanoff, "Effects of radiotherapy with concomitant and adjuvant temozolomide versus radiotherapy alone on survival in glioblastoma in a randomised phase III study: 5-year analysis of the EORTC-NCIC trial.," *The lancet oncology*, vol. 10, pp. 459–66, May 2009.

[44] M. Salcman, "Resection and reoperation in neuro-oncology. rationale and approach.," *Neurologic clinics.*, vol. 3, pp. 831–842, 1985.

[45] F. M. K. B. J. Gerbi, *Treatment Planning in Radiation Oncology*. Wolters Kluwer/Lippincott Williams & Wilkins, 3rd ed., 2012.

[46] M. J. A. van der Kogel, *Basic Clinical Radiobiology*. Hodder Arnold, 4th ed., 2009.

[47] "Icru report 50. prescribing, recording and reporting photon beam therapy.," 1993.

[48] "Icru report 62. prescribing, recording and reporting photon beam therapy (supplement to icru report 50)," 1999.

[49] E. Newlands, M. Stevens, and S. Wedge, "Temozolomide: a review of its discovery, chemical properties, pre-clinical development and clinical trials.," *Cancer treatment*, pp. 35–61, 1997.

[50] I. M. J. Freund, *Probability and Statistics for Engineers*. Pearson, 7 ed., 2006.

[51] H. A. D. H. Nagaraje, *Order Statistics*. Wiley, 3 ed., 2003.

[52] A. Dekkers, J. Einmahl, and L. D. Haan, "A moment estimator for the index of an extreme-value distribution," *The Annals of Statistics*, vol. 17, no. 4, pp. 1833–1855, 1989.

[53] M. D. Piroth, R. Holy, M. Pinkawa, G. Stoffels, H. J. Kaiser, N. Galldiks, H. Herzog, H. H. Coenen, M. J. Eble, and K. J. Langen, "Prognostic impact of postoperative, pre-irradiation (18)F-fluoroethyl-l-tyrosine uptake in glioblastoma patients treated with radiochemotherapy.," *Radiotherapy and oncology : journal of the European Society for Therapeutic Radiology and Oncology*, vol. 99, pp. 218–24, May 2011.

[54] K. J. Langen, N. Roosen, H. H. Coenen, J. T. Kuikka, T. Kuwert, H. Herzog, G. Stöcklin, and L. E. Feinendegen, "Brain and brain tumor uptake of L-3-[123I]iodo-alpha-methyl tyrosine: competition with natural L-amino acids.," *Journal of nuclear medicine : official publication, Society of Nuclear Medicine*, vol. 32, pp. 1225–9, June 1991.

[55] J. P. III, "Statistical inference using extreme order statistics," *the Annals of Statistics*, vol. 3, no. 1, pp. 119–131, 1975.

[56] F. H. P. van Velden, P. Cheebsumon, M. Yaqub, E. F. Smit, O. S. Hoekstra, A. a. Lammertsma, and R. Boellaard, "Evaluation of a cumulative SUV-volume histogram method for parameterizing heterogeneous intratumoural FDG uptake in non-small cell lung cancer PET studies.," *European journal of nuclear medicine and molecular imaging*, vol. 38, pp. 1636–47, Sept. 2011.

[57] D. Brandsma, L. Stalpers, W. Taal, and P. Sminia, "Clinical features, mechanisms, and management of pseudoprogression in malignant gliomas," *The lancet oncology*, 2008.

[58] A.-L. Grosu and W. A. Weber, "PET for radiation treatment planning of brain tumours.," *Radiotherapy and oncology : journal of the European Society for Therapeutic Radiology and Oncology*, vol. 96, pp. 325–7, Sept. 2010.

[59] A. P. Krishnan, I. M. Asher, D. Davis, P. Okunieff, and W. G. O'Dell, "Evidence that MR diffusion tensor imaging (tractography) predicts the natural history of regional progression in patients irradiated conformally for primary brain tumors.," *International journal of radiation oncology, biology, physics*, vol. 71, pp. 1553–62, Aug. 2008.

[60] B. G. Baumert, J. Lutterbach, R. Bernays, J. Davis, and F. L. Heppner, "Fractionated stereotactic radiotherapy boost after post-operative radiotherapy in patients with high-grade gliomas," *Radiotherapy and Oncology*, vol. 67, pp. 183–190, May 2003.

[61] E. L. Chang, S. Akyurek, T. Avalos, N. Rebueno, C. Spicer, J. Garcia, R. Famiglietti, P. K. Allen, K. S. C. Chao, A. Mahajan, S. Y. Woo, and M. H. Maor, "Evaluation of peritumoral edema in the delineation of radiotherapy clinical target volumes for glioblastoma.," *International journal of radiation oncology, biology, physics*, vol. 68, pp. 144–50, May 2007.

[62] I. H. Lee, M. Piert, D. Gomez-Hassan, L. Junck, L. Rogers, J. Hayman, R. K. Ten Haken, T. S. Lawrence, Y. Cao, and C. Tsien, "Association of 11C-methionine PET uptake with site of failure after concurrent temozolomide and radiation for primary glioblastoma multiforme.," *International journal of radiation oncology, biology, physics*, vol. 73, pp. 479–85, Feb. 2009.

[63] C. I. Tsien, D. Brown, D. Normolle, M. Schipper, M. Piert, L. Junck, J. Heth, D. Gomez-Hassan, R. K. Ten Haken, T. Chenevert, Y. Cao, and T. Lawrence, "Concurrent temozolomide and dose-escalated intensity-modulated radiation therapy in newly diagnosed glioblastoma.," *Clinical*

cancer research : an official journal of the American Association for Cancer Research, vol. 18, pp. 273–9, Jan. 2012.

[64] G. Matthys and J. Beirlant, "Estimating the extreme value index and high quantiles with exponential regression models," *Statistica Sinica*, vol. 13, pp. 853–880, 2003.

[65] S. E. Eikenberry, T. Sankar, M. C. Preul, E. J. Kostelich, C. J. Thalhauser, and Y. Kuang, "Virtual glioblastoma: growth, migration and treatment in a three-dimensional mathematical model.," *Cell proliferation*, vol. 42, pp. 511–28, Aug. 2009.